

Low Cost Hydrogen Transport Membranes

Anthony F. Sammells, Shane E. Roark,
Michael V. Mundschau, and Thomas F. Barton

Eltron Research Inc.
4600 Nautilus Court South
Boulder, CO 80301
www.eltronresearch.com

Introduction

Eltron Research Inc. is developing low cost, multi-phase membranes for separating hydrogen from hydrogen containing feedstreams (Figure 1). This is being addressed using metal/ceramic composites which facilitate high proton and electron conduction. Membranes are being developed for high (>750°C) and low (<425°C) temperature applications and have been successfully operated under a high pressure differential (250 psi) for extended times. Under ambient pressure, hydrogen transport rates >25 mL/cm²/min have been achieved at 400°C.

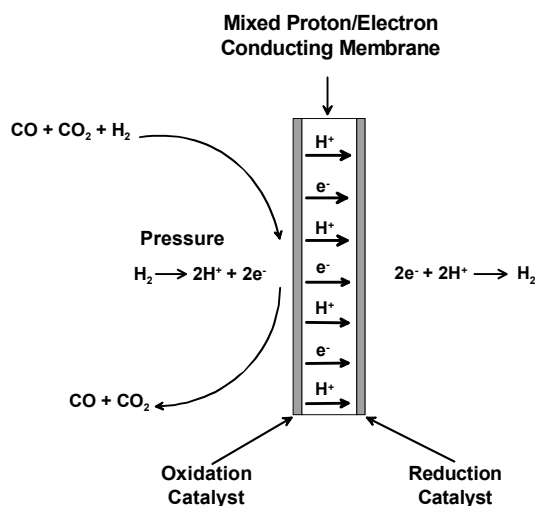


Figure 1. Schematic diagram of metal/ceramic composite membrane process for separating hydrogen from a mixture of gases.

Experimental

Doped perovskites A_{1-x}A_xB_{1-y}B_yO_{3-δ}, where x and y are the fractions of dopants in the A and B sites, respectively, and δ is the number of oxygen vacancies,¹⁻³ were prepared using conventional high temperature solid state synthesis techniques. Corresponding cermets A_{1-x}A_xB_{1-y}B_yO_{3-δ}/M were prepared by sequential pressing and sintering at elevated temperatures under controlled atmosphere conditions.

The inlet hydrogen source was initially diluted with helium. This facilitated determination of the membrane seal quality. H₂ and He fractions within inlet and sweep streams were determined by TCD-GC using a Shimadzu GC 14-A with a 12-ft. by 1/8-in. stainless steel Carbosphere column. Ultra-high purity Ar was used as the carrier gas to optimize detection limits for hydrogen and helium.

Results and Discussion

Hydrogen transport metal/ceramic composite membranes under development at Eltron consist of an adherent ceramic phase and a

low cost hydrogen permeable metallic phase. The ceramic phase can either be a dense mixed proton and electron conductor or a porous non-conducting material. This latter approach is largely for providing mechanical support when thin-film metal alloys are used.

Hydrogen permeation P(mole·m⁻¹·s⁻¹·Pa^{1/2}) through these membranes, in the absence of surface kinetic limitations, is dependent on the membrane thickness, t, according to,

$$P = \frac{J \cdot t}{\sqrt{p_{H_2, in}} - \sqrt{p_{H_2, out}}}$$

where J is the hydrogen flux through the membrane in mole·m⁻²·s⁻¹. For this class of membrane, the dependency of hydrogen flux upon thickness is shown in Figure 2 at 320°C. These membranes have been successfully operated for thousands of hours at both ambient pressure and with a 250 psi pressure differential between the hydrogen feed and permeate side.

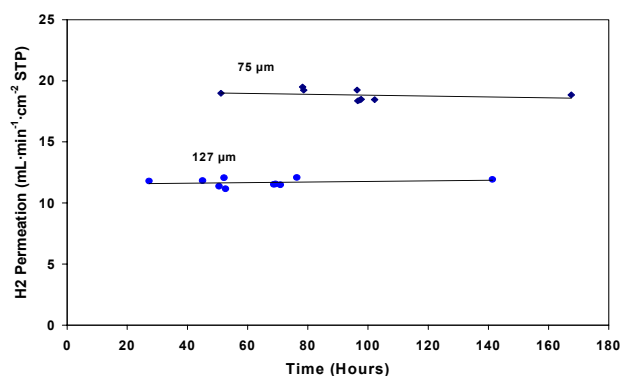


Figure 2. Hydrogen permeation as a function of time at 320°C for different membrane thicknesses. The feed gas was 80 mL/min 80/20 H₂/He and the sweep gas was approximately 250 mL/min Ar.

The performance of our low cost membranes operating under ambient pressure conditions as a function of temperature (Figure 3) and Ar sweep rate (Figure 4) on the hydrogen permeate side are shown below. As can be seen, hydrogen diffusion fluxes >25 mL/cm²/min have been achieved at 400°C.

A simplified block diagram of a hydrogen separation unit installed in an integrated gasification combined cycle (IGCC) plant is shown in Figure 5. The diagram shows three options for installation, indicated as baseline, alternative 1, and alternative 2. The alternative 1 option assumes the membrane materials will be tolerant to sulfur and particulate material, and that the raw syngas from coal gasification can be sent directly to the unit. The baseline option also assumes sulfur tolerance, but the gas stream must be filtered prior to entering the unit. If the membrane materials are not sulfur tolerant, then alternative 2 will be necessary, and the unit will be inserted after desulfurization. This condition will require reheating the gas stream through a heat exchange prior to entering the hydrogen separation unit.

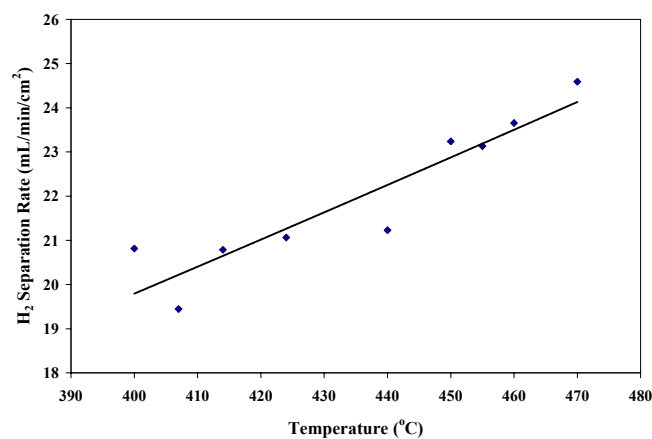


Figure 3. Hydrogen diffusion as a function of operating temperature under ambient pressure conditions. Ar sweep rate on permeate side 300 mL/min.

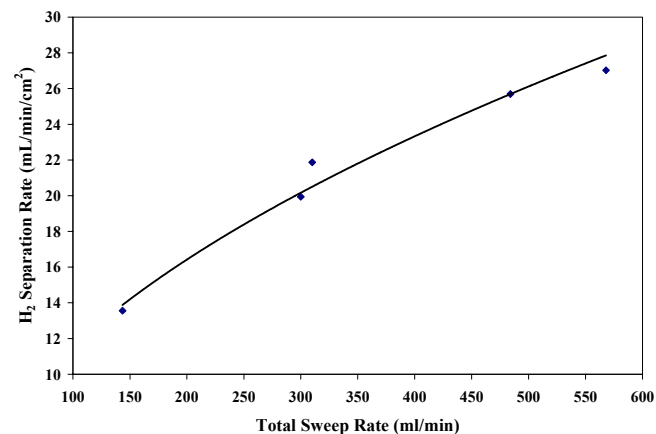


Figure 4. Hydrogen diffusion as a function of Ar sweep rate on the permeate side at 400°C. Ambient pressure conditions.

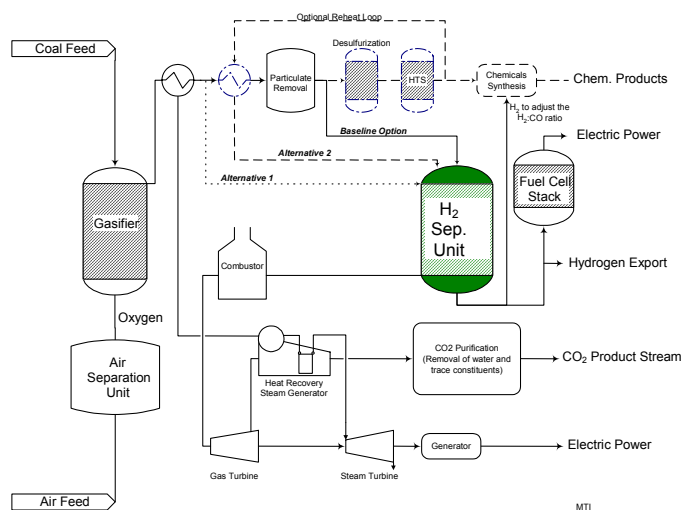


Figure 5. Diagram of an IGCC plant with three installation options for a hydrogen separation unit.

Acknowledgment

This work is supported by DOE/NETL under Contract Number DE-FC26-00NT40762.

References

- (1) White, J. H.; Schwartz, M.; and Sammells, A. F. U.S. Patent 5,821,185, October 13, 1998.
- (2) White, J. H.; Schwartz, M.; and Sammells, A. F. U.S. Patent 6,037,514, March 14, 2000.
- (3) White, J. H.; Schwartz, M.; and Sammells, A. F. U.S. Patent 6,281,403, August 28, 2001.

PRODUCTION OF SYNTHESIS GAS FROM METHANOL WITH NONTHERMAL PLASMA

Shigeru Futamura and Hajime Kabashima

National Institute of Advanced Industrial
Science and Technology
AIST Tsukuba West, 16-1 Onogawa, Tsukuba, Ibaraki,
305-8569 Japan

Introduction

Recently, application of nonthermal plasma to the processes for the production of hydrogen¹⁻⁵ and synthesis gas⁶⁻¹⁰ has attracted much attention due to its technical merits such as quick response, low and flexible reaction temperature, and facile operations. Only batch systems are available for relatively new approaches such as photocatalysis^{11,12} and mechano-catalysis.^{13, 14} On the other hand, reactions can be carried out in flow systems with nonthermal plasma, and furthermore, higher energy efficiency and higher rate for hydrogen production are obtained in water splitting. Based on these findings, the system of nonthermal plasma can be extended to processes of fuel reforming at lower temperatures. It has been already reported that process load can be reduced in the steam reforming of aliphatic hydrocarbons with nonthermal plasma.⁵

It is essentially important to optimize the plasma-generating method and reaction conditions from the practical viewpoint. However, this kind of information has been sparsely documented in the literature. This paper presents the effects of reactor type and voltage waveform and frequency on the efficiencies in the production of synthesis gas from methanol.

Experimental

A ferroelectric packed-bed reactor (**FPR**) and a silent discharge reactor (**SDR**) used in this research were described in detail elsewhere.^{15,16} Methanol was introduced to the reactor by passing N₂ through methanol in a small volume of water-bubbling device set in a thermostatic bath. Methanol concentrations were adjusted with the temperature at the thermostatic bath. The gas residence time varied from 8.9 to 44.3 s for **FPR** and 0.36 to 1.80 s for **SDR** at 0.50 to 0.10 L/min of gas flow rate. The both reactors employed 5-5000 Hz ac and high voltage up to 11 kV was applied to both of them. No breakdowns occurred during operations within their maximum voltages.

The values of plug-in power and applied voltage for **FPR** and **SDR** were measured with a digital powermeter and a digital wavemeter, respectively. Combination of a model of high voltage amplifier 20/20/B (Trek Japan, Co., Ltd.), a function generator (FG-2, Wavetek), and an oscilloscope (SONY TEKTRONIX TDS 3052) was used instead of a Neon transformer to estimate the power consumptions in both the reactors. In the applied voltage range of 3 kV to 11 kV, data sets were collected for power consumptions in the reactors and methanol conversions only with this amplifier. Then, the actual power consumptions without using 20/20B were calculated by comparing the methanol conversions at the same applied voltages with and without 20/20B. With this procedure, it was shown that about 10±2% and 20 %±3% of plug-in power were consumed in **FPR** and **SDR**, respectively.

The volatile byproducts were identified by GC-MS. Methanol conversion and byproduct yields were determined by FID-GC. The concentrations of CO, CO₂, N₂O, ethane, ethylene, and acetylene were determined by GC with both of TCD and FID and the combined columns of Porapak Q+N and Molecular Sieve 13X. H₂ and methane

were quantified by TCD-GC with a packed column of Molecular Sieve 13X.

Results and Discussion

Definitions of RED and the yields of H₂, CO, and CO₂. As a measure of energy density for **FPR** and **SDR**, reactor energy density (RED) will be used later (1), where Power denotes the plug-in power. The yields of H₂ and CO_x (x = 1 and 2) are defined in (2) and (3), respectively.

$$\text{RED (kJ / L)} = A \times \text{Power (kW)} / [\text{Gas flow rate (L/min)} / 60] \quad (1)$$

$$(A = 0.1 \text{ and } 0.2 \text{ for } \mathbf{FPR} \text{ and } \mathbf{SDR}, \text{ respectively.})$$

$$\text{H}_2 \text{ yield (mol\%)} = 50 \times [\text{H}_2 \text{ concentration (ppm)} / \text{initial CH}_3\text{OH concentration (ppm)}] \quad (2)$$

$$\text{CO}_x \text{ yield (mol\%)} = 100 \times [\text{CO}_x \text{ concentration (ppm)} / \text{initial CH}_3\text{OH concentration (ppm)}] \quad (3)$$

Waveform Effect on the Reaction Behavior of CH₃OH.

Tables 1 and 2 show the waveform effect on the reaction behavior of methanol in N₂. Applied voltages were set to obtain comparable methanol conversions for **FPR** and **SDR**.

Table 1. Effect of Voltage Waveform on Methanol Conversion

Reactor	Waveform	Applied voltage (kV)	Reactor power consumption (W)	MeOH conv. (mol%)
FPR	Triangle	6.86	0.48	26
FPR	Sine	6.84	0.22	12
FPR	Square	6.88	0.21	8
SDR	Triangle	9.20	1.99	21
SDR	Sine	9.36	1.32	18
SDR	Square	9.34	1.31	10

Voltage frequency: 50 Hz. Power consumptions in 20/20B varied in the range of 520 to 524 W. Methanol concentration 1.0 %; Q = 100 mL/min.

Table 2. Effect of Voltage Waveform on Product Distribution

Reactor	Waveform	MeOH conv. (mol%)	Product yield (mol%)		
			H ₂	CO	CO ₂
FPR	Triangle	26	5.3	4.9	0.9
FPR	Sine	12	2.6	2.4	0.5
FPR	Square	8	1.1	1.0	0.2
SDR	Triangle	21	4.2	3.2	0.7
SDR	Sine	18	3.1	2.1	0.4
SDR	Square	10	1.4	0.8	0.2

Voltage frequency: 50 Hz. Power consumptions in 20/20B varied in the range of 520 to 524 W. Methanol concentration 1.0 %; Q = 100 mL/min.

Table 1 clearly shows that higher applied voltages and larger reactor power consumptions are required for **SDR** than for **FPR** to attain comparable methanol conversions. Since the power consumptions for the primary power source (20/20B) do not change, irrespective of waveform and applied voltage, the energies of energetic electrons in nonthermal plasma are consumed in methanol conversion more effectively in **FPR** than in **SDR**. The catalytic effect of BaTiO₃ can be neglected at ambient temperature, the different performances of **FPR** and **SDR** are ascribed to the reactor-dependent populations of electron energies in nonthermal plasma.

With **FPR**, the molar ratios of H₂ to CO {[H₂] / [CO]} are ca. 2.20, irrespective of waveform and methanol conversion (Table 2).

On the other hand, $[H_2] / [CO]$ increases from 2.63 (triangle) to 3.50 (square) with **SDR**. Irrespective of the reactors, CO was obtained in ca. 5-times higher yields than CO_2 . Under our reaction conditions, the step of CO oxidation to CO_2 is slow due to the absence of O_2 and H_2O . The lower ratios of H_2 to CO could be partly ascribed to higher mole fractions of CO_2 .

Frequency Effect on Methanol Conversion. In use of a Neon transformer (Neon) at 50 Hz of plug-in voltage, **FPR** worked much better than **SDR** in methanol conversion. At higher frequencies, however, **SDR** was much more sensitive to frequency change than **FPR** (Figs. 1 and 2). At 500 Hz, methanol conversion was far lower than that with the Neon transformer at 50 Hz for **FPR** (Fig. 1). On the other hand, comparable conversions were obtained for **SDR** (Fig. 2). With this reactor, methanol was almost quantitatively converted at 5000 Hz. The power consumptions in 20/20B at 5000 Hz did not change with **FPR** and **SDR**.

The product distribution was not affected by frequency. The lifetime of the energetic electron is shorter than 10^{-6} s, and it does not seem that reactor type and voltage properties drastically affect the product-forming processes.

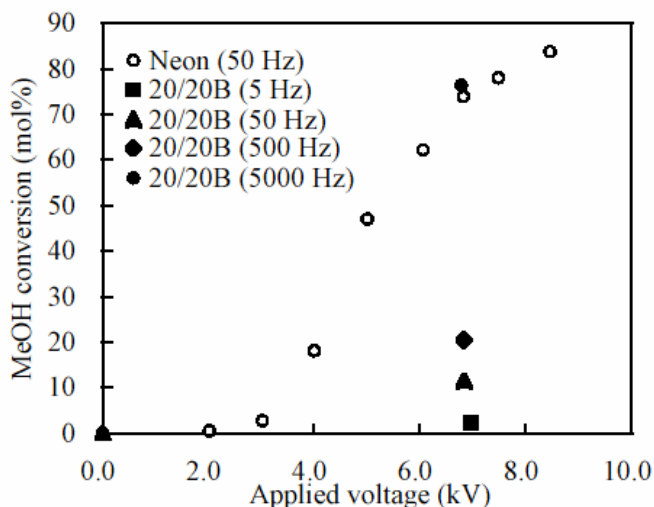


Figure 1. Effect of power source and frequency in the methanol conversion with **FPR**. Methanol concentration 1.0 %; $Q = 100$ mL/min.

Additive Effect of H_2O and O_2 . With **FPR** at 50 Hz of plug-in voltage, additive effect of H_2O and O_2 was investigated with $[H_2O] / [CH_3OH]$ up to 1.0 and $[O_2] / [CH_3OH]$ up to 0.15. The general trend was that these additives improved the carbon balance in the reaction rather than promote the methanol conversion. At higher concentrations of O_2 and H_2O , abatement of the endothermicity in methanol conversion and H_2 consumption are in a trade-off relationship with each other.

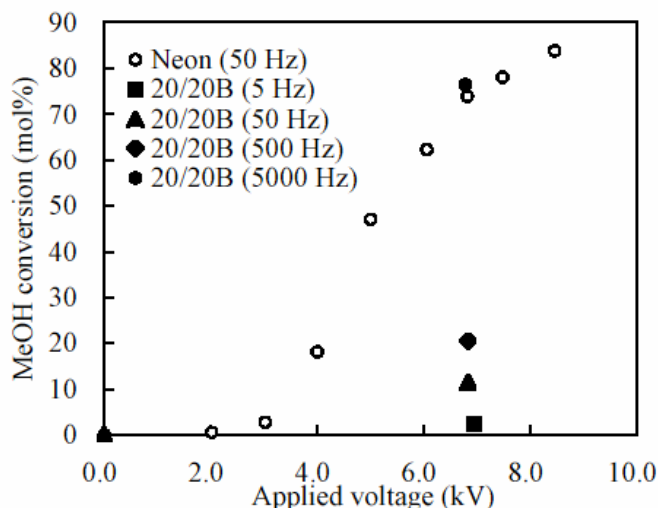


Figure 2. Effect of power source and frequency in the methanol conversion with **SDR**. Methanol concentration 1.0 %; $Q = 100$ mL/min.

Conclusions

It has been shown that effects of waveform and frequency are reflected in the process of methane reforming with nonthermal plasma, and that this effect depends on reactor type.

Acknowledgment. This work was partly supported by the Grants-in-Aid from New Energy and Industrial Technology Development Organization of Japan (NEDO).

References

- (1) Chen, X.; Marquez, M.; Rozak, J.; Marun, C.; Luo, J.; Suib, S. L.; Hayashi, Y.; Matsumoto, H. *J. Catal.*, **1998**, 178, 372.
- (2) Tanabe, S.; Matsuguma, H.; Okitsu, K.; Matsumoto, H. *Chem. Lett.*, **2000**, 1116.
- (3) Kabashima, H.; Einaga, H.; Futamura, S. *Chem. Lett.*, **2001**, 1314.
- (4) Yao, S. L.; Okumoto, M.; Nakayama, A.; Suzuki, E. *Energy Fuels*, **2001**, 15, 1295.
- (5) Kabashima, H.; Einaga, H.; Futamura, S. *IEEE Trans. Ind. Appl.*, **2003**, 39, 340.
- (6) Zhou, L. M.; Xue, B.; Kogelschatz, U.; Eliasson, B. *Energy Fuels*, **1998**, 12, 1191.
- (7) Kado, S.; Urasaki, K.; Sekine, Y.; Fujimoto, K. *Chem. Commun.*, **2001**, 415.
- (8) Bromberg, L.; Cohn, D. R.; Rabinovich, A.; Alexeev, N. Prepr. Pap. – Am. Chem. Soc., *Div. Fuel Chem.*, **2001**, 46(1), 1.
- (9) Kabashima, H.; Futamura, S. Prepr. Pap. – Am. Chem. Soc., *Div. Fuel Chem.*, **2002**, 47(2), 661.
- (10) Kabashima, H.; Futamura, S. *Chem. Lett.*, **2002**, 1108.
- (11) Takata, T.; Tanaka, A.; Hara, M.; Kondo, J. N.; Domen, K. *Catal. Today*, **1998**, 44, 17.
- (12) Kudo, A. *J. Ceramic Soc. Jpn.*, **2001**, 109, S-81.
- (13) Ohta, T. *Appl. Energy*, **2000**, 67, 181.
- (14) Hara, M.; Komaba, M.; Hasei, H.; Yashima, M.; Ikeda, S.; Takata, T.; Kondo, J. N.; Domen, K. *J. Phys. Chem. B*, **2000**, 104, 780.
- (15) Futamura, S.; Zhang, A.; Yamamoto, T. *IEEE Trans. Ind. Applicat.*, **2000**, 36, 1507.
- (16) Einaga, E.; Ibusuki, T.; Futamura, S. *IEEE Trans. Ind. Applicat.*, **2001**, 37, 1476.

EFFECTS OF REDOX PROPERTIES ON ISOSYNTHESIS OVER ZrO₂ BASED CATALYSTS

Yingwei Li, Dehua He*, Qiming Zhu, Boqing Xu

State Key Lab of C₁ Chemistry and Technology
Department of Chemistry, Tsinghua University
Beijing 100084, China

Introduction

Isosynthesis refers to the reaction that selectively converts coal or natural gas derived syn-gas (CO + H₂) to i-C₄ hydrocarbons (isobutene and isobutane). Zirconium dioxide catalyst has been shown to be active for this reaction with a high selectivity to isobutene.¹ It is well known that zirconia possesses explicitly particular chemical properties; acidic and basic properties and oxidizing and reducing properties.² The effects of acidic and basic properties on the catalytic performance of isosynthesis have been extensively investigated over zirconia based catalysts.³⁻⁸ However, little work has been reported on the effects of redox properties of zirconia based catalysts on the isosynthesis. The primary objective of present work is to identify the function of redox properties on isosynthesis selectivities through a systematic investigation on the effects of acid-base and redox properties upon the catalytic performances of zirconia based catalysts in the isosynthesis. The redox property was modified by doped ZrO₂ with various quantities of CeO₂ and Y₂O₃. The reduction and acid-base properties were systematically investigated using temperature programmed reduction (TPR) and desorption (TPD) study. In parallel, steady-state isosynthesis activities and selectivities were measured to relate the observed catalytic performances to the acid-base and redox properties characterized on these CeO₂ and Y₂O₃ doped ZrO₂ catalysts.

Experimental

Preparation of catalysts. Preparation of zirconia catalyst has been described in our previous work.⁷ CeO₂-ZrO₂ and Y₂O₃-ZrO₂ mixed oxides were synthesized by co-precipitation of a mixed solution of ZrOCl₂ and various additives, cerium or yttrium nitrate salts, with ammonium solution.

Characterization of catalysts. The acid-base properties of the catalysts were measured by temperature programmed desorption (TPD) of ammonia and carbon dioxide,⁷ respectively. Temperature programmed reduction (TPR) studies were carried out in a conventional system equipped with a thermal conductivity detector (TCD). The amount of catalyst used was 100 mg in all cases. TPR was carried out in a flow of 5% H₂/Ar (20 ml/min) at a heating rate of 10 K/min.

Reaction Procedure. The hydrogenation of CO was carried out in one quartz lined stainless steel tubular reactor⁹ at 5.0 MPa, 673 K and 650 h⁻¹. The detailed process of pretreatment and evaluation of catalysts please refer to our previous paper.⁸

Results and Discussion

Three CeO₂ doped ZrO₂ (12, 50, 88 mol% CeO₂) and five Y₂O₃ doped ZrO₂ (2.5, 4.5, 6.2, 8.6, 12.0 mol% Y₂O₃) were prepared and tested for their isosynthesis activities. Pure ZrO₂ prepared in this study has a specific area ca. 55 m² g⁻¹. All the CeO₂-ZrO₂ and Y₂O₃-ZrO₂ mixed oxides have moderate specific areas in the range of ca. 80 to 130 m² g⁻¹. Monoclinic phase was the dominating crystal phase for pure ZrO₂ prepared in this study. However, tetragonal and cubic ZrO₂ phases were the main crystal phases for all the CeO₂ and Y₂O₃ doped ZrO₂ mixed oxides.

The reduction behaviors of CeO₂-ZrO₂ and Y₂O₃-ZrO₂ mixed oxides were investigated by means of the H₂-TPR technique. Only a small quantity of H₂ was consumed on pure ZrO₂.¹⁰ The incorporation of CeO₂ and Y₂O₃ to ZrO₂ greatly enhanced the reduction behavior of ZrO₂. The maximum quantity of H₂ consumption for CeO₂ and Y₂O₃ doped ZrO₂ mixed oxides was obtained at 50% CeO₂ and 8.6% Y₂O₃ doped, respectively. This enhancement of H₂ consumption can be attributed to the mobility of lattice oxygen that was enhanced and then be more active to react with H₂ by the incorporation of CeO₂ or Y₂O₃ with ZrO₂.¹⁰

The acid and base properties of the CeO₂ and Y₂O₃ doped ZrO₂ catalysts also varied with the quantities of dopants added. The amount of acidic and basic sites for CeO₂-ZrO₂ mixed oxides both remarkably decreased with an increase in the content of CeO₂. For Y₂O₃-ZrO₂ mixed oxides, the amount of acidic sites increased slightly with more and more Y₂O₃ doped. However, the amount of basic sites decreased with an increase in the content of Y₂O₃ from 4.5% to 12%. It is not clear what caused 2.5% Y₂O₃ doped ZrO₂ catalyst to have so small quantity of basic sites (ca. 44.2 μmol g⁻¹).

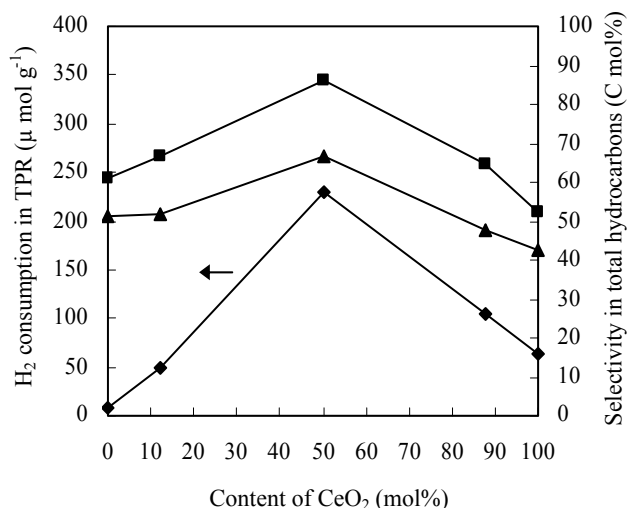


Figure 1. Quantities of H₂ consumption and selectivities to C₄ and i-C₄ in total hydrocarbons as a function of content of CeO₂ for CeO₂-ZrO₂ mixed oxide catalysts. ■ C₄ selectivity in total hydrocarbons, ▲ i-C₄ selectivity in total hydrocarbons.

The catalytic test results of the CeO₂-ZrO₂ and Y₂O₃-ZrO₂ mixed oxide catalysts in the isosynthesis are related to the redox properties of the zirconia based catalysts. Figure 1 shows the quantities of H₂ consumption in TPR measurement and selectivities to C₄ and i-C₄ in total hydrocarbons as a function of the content of CeO₂ doped in the catalysts. It can be seen that the highest selectivity to C₄ in total hydrocarbons was obtained over the catalyst which has a maximum quantity of H₂ consumption. Similar results were obtained over the Y₂O₃-ZrO₂ mixed oxide catalysts. The maximum was at 50%CeO₂ and 8.6%Y₂O₃, respectively. The selectivity to i-C₄ in total hydrocarbons also increased with increasing the quantity of H₂ consumption, as shown in Figure 1. However, the selectivity to i-C₄ in total hydrocarbons was unnecessarily achieved the maximum over the catalyst which has a maximum H₂ consumption in the TPR. For the Y₂O₃-ZrO₂ mixed oxide catalysts, the maximum H₂ consumption was at 8.6%Y₂O₃ doped. The highest selectivity to i-C₄ in total hydrocarbons was, however, obtained over the 6.2%Y₂O₃ doped ZrO₂ catalyst. No direct relationship between the amount of acidic or

basic sites and the selectivity to C₄ and i-C₄ in total hydrocarbons was observed for both CeO₂ and Y₂O₃ doped ZrO₂ catalysts, as shown in Figure 2 for CeO₂ doped ZrO₂ catalysts. Therefore, the improvement of catalytic performances over some CeO₂ and Y₂O₃ doped ZrO₂ catalysts can be attributed to the enhancement of reduction properties that are suggested to be related to the increased mobility of lattice oxygen.¹⁰

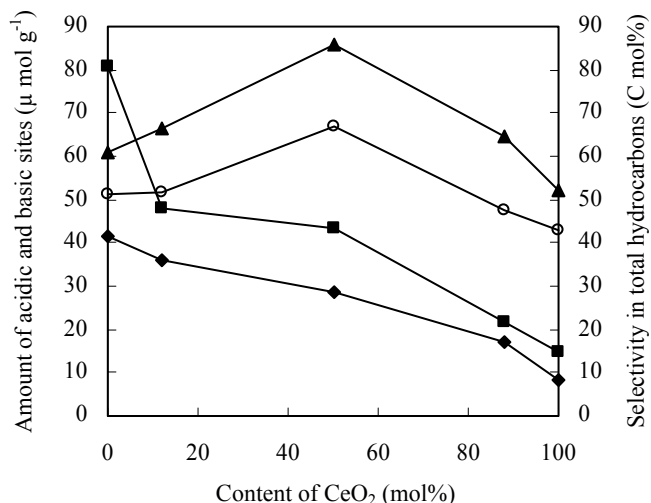


Figure 2. Amount of acidic and basic sites and selectivities of C₄ and i-C₄ in total hydrocarbons as a function of content of CeO₂ for CeO₂-ZrO₂ mixed oxide catalysts. ♦ Amount of acidic sites, ■ Amount of basic sites, ▲ C₄ selectivity in total hydrocarbons, ○ i-C₄ selectivity in total hydrocarbons.

However, the redox property can't be assigned to be the only factor in determining the catalytic performances of the catalysts. For Y₂O₃-ZrO₂ mixed oxide catalysts, the highest i-C₄ selectivity in total hydrocarbons was achieved over 6.2%Y₂O₃ doped ZrO₂ based catalyst neither 8.6%Y₂O₃ nor 12%Y₂O₃ doped catalysts which both have larger quantities of H₂ consumption. It is also found that the selectivity to C₄ and i-C₄ in total hydrocarbons showed a sharp decline with more C₁ and C₂ hydrocarbons when the content of Y₂O₃ was increased from 8.6% to 12%, although similar redox properties were obtained over these two catalysts. This would be ascribed to the large decrease of basic sites on the 12%Y₂O₃ doped ZrO₂ catalyst (ca. 45 μmol g⁻¹) since basic sites has been suggested to be significant for the formation of i-C₄ hydrocarbons.^{4,6-8} The marked decrease of basic sites can also explain the lower i-C₄ selectivities in total hydrocarbons for the 88%CeO₂ and 2.5%Y₂O₃ doped ZrO₂ catalysts compared to that for pure ZrO₂ catalyst. The amount of basic sites for these two catalysts was ca. 21.5 and 44.2 μmol g⁻¹, respectively. However, it was ca. 81 μmol g⁻¹ for pure ZrO₂ catalyst. Therefore, the improvement of C₄ and i-C₄ selectivities in total hydrocarbons over some CeO₂ and Y₂O₃ doped catalysts would be attributed to the enhancement of redox properties meanwhile maintaining an appropriate amount of base sites over these catalysts.

Acknowledgment

Financial support of this study is provided by the Foundation for Fundamental Research of Tsinghua University and the Analytical Foundation of Tsinghua University.

References

1. Maehashi, T.; Maruya, K.; Domen, K.; Aika, K.; Onishi, T. *Chem. Lett.*, **1984**, 747.
2. Tanabe, K. *Materials Chemistry and Physics*, **1985**, 13, 347.
3. Maruya, K.; Maehashi, T.; Haraoka, T.; Narui, S.; Asakawa, Y.; Domen, K.; Onishi, T. *Bull. Chem. Soc. Jpn.*, **1988**, 61, 667.
4. Feng, Z. T.; Postula, W. S.; Akgerman, A.; and Anthony, R. G. *Ind. Eng. Chem. Res.*, **1995**, 34, 78.
5. Jackson, N. B.; and Ederkt, J. G. *J. Catal.*, **1990**, 126, 31.
6. Su, C. L.; Li, J. R.; He, D. H.; Cheng, Z. X.; and Zhu, Q. M. *Appl. Catal.*, **2000**, 202, 81.
7. Li, Y. W.; He, D. H.; Cheng, Z. X.; Su, C. L.; Li, J. R.; and Zhu, Q. M. *Journal of Molecular Catalysis A: Chemical*, **2001**, 175, 267.
8. Li, Y. W.; He, D. H.; Yuan, Y. B.; Cheng, Z. X.; and Zhu, Q. M. *Energy & Fuels*, **2001**, 15 (6), 1434.
9. Li, Y. W.; He, D. H.; Zhu, Q. M. Prepr. Pap. – *Am. Chem. Soc., Div. Fuel Chem.*, **2002**, 47 (1), 168.
10. Otsuka, K.; Wang, Y.; and Nakamura, M. *Appl. Catal.*, **1999**, 183, 317.

TOWARDS THE DEVELOPMENTS OF ROBUST WATER-GAS SHIFT REACTORS

Robert M. Enick¹, Anthony V. Cugini, Richard P. Killmeyer, Bret H. Howard, Bryan M. Morreale², Michael V. Ciocco² and Felipe Bustamante¹

U.S. Department of Energy
National Energy Technology Laboratory
P.O. Box 10940, Pittsburgh PA 15236

(1) NETL Research Associate, University of Pittsburgh
enick@engr.pitt.edu, (2) NETL Site Support Contractor, Parsons
Project Services Inc.

Introduction

Hydrogen permeable Water-Gas Shift membrane reactors are being considered for the simultaneous production of separate hydrogen and carbon dioxide-streams from a coal gasification plant. As hydrogen permeates the membrane, the conversion of carbon monoxide and water to carbon dioxide and hydrogen in this equilibrium-limited reaction increases, resulting in the production of a high purity, low pressure hydrogen permeate and a high pressure, carbon dioxide-rich stream for sequestration¹.

The design of these membrane reactors requires models of the reaction kinetics and membrane performance at the post-gasifier conditions expected for various coal gasification plant configurations, with temperatures up to 1173 K, pressures up to 6.89 MPa, and hydrogen sulfide concentrations as high as 1000 ppm.

The first objective of this study is to describe the intrinsic kinetics of the forward Water-Gas Shift reaction at post-gasifier conditions in a high-pressure quartz reactor. In a commercial reactor, the reacting gas mixture flow would contact the reactor surfaces, the membrane, and heterogeneous catalyst particles. Because each of these solid surfaces may dramatically influence the reaction kinetics², the forward WGS kinetics will also be determined in a high-pressure quartz reactor packed with a material that corresponds to each of these surfaces. If a significant rate enhancement is found to be associated with the reactor material and membrane surface, the need for the introduction of the heterogeneous catalyst particles may be eliminated.

The second objective of this study is to determine the effect of temperature, pressure, alloy composition and hydrogen sulfide feed stocks on the hydrogen permeance of several Pd/Cu alloy membranes.

Experimental

Kinetic studies. Details of the reactor configuration are given elsewhere². Basically, CO and water were fed premixed to the reactor through a narrow annulus with a volume less than one tenth that of the reaction zone. The gases were rapidly heated to the reaction temperature as they passed through the annulus. CO flowrate was controlled with Brooks mass flow controllers. Water was added to the CO stream by means of a syringe pump. Tubing upstream and downstream the reactor was heat-taped and insulated to avoid condensation of water. Reactor temperature was controlled with a thermocouple placed directly on the top of the reactor; pressure was controlled with a pressure controller downstream the reactor. Conversions were kept lower than 2% in the quartz reactor studies to forfeit any effect of the reverse reaction. The effluent from the reactor was analyzed with a GC equipped with a TCD detector.

Permeation studies. The hydrogen membrane test (HMT) unit, fabricated at the NETL, was designed to evaluate membrane performance at high-temperatures and pressures via steady-state hydrogen flux testing and has been described previously³. The

apparatus was designed to operate at temperatures and pressures up to 1173 K and 3 MPa, respectively.

The various compositions Pd/Cu alloy membranes of interest in this study (40, 53, 60, and 80 wt% Pd), were prepared by ACI Alloys as 100 micron thick foils, 99.9% purity, while pure palladium and copper foils were obtained by Alfa Aesar. Membranes were fabricated for testing by brazing foil disks to thick nickel alloy washers having negligible hydrogen permeability; high-purity gold powder was used as brazing material. Brazing was done in a muffle furnace at 1400 K. A porous metal support was utilized on the permeate side of the membrane foil to prevent foil distortion and possible mechanical failure at high temperatures in the presence of a pressure drop. The membrane surface contacted the porous support surface but was not bonded to it. The resulting mounted membranes had an active hydrogen permeation diameter of approximately 8.5 mm. The membrane brazing and mounting techniques were developed at the NETL.

Sulfur-tolerance studies. The hydrogen permeance in the presence of 1000 ppm hydrogen sulfide of several of the Pd/Cu membranes described previously was determined within the NETL's Hydrogen Membrane Batch (HMB) unit. The HMB unit was designed to evaluate the hydrogen permeance of possible sulfur tolerant membrane materials over a wide range of temperatures (up to 1073 K) and relatively low-pressures (up to 0.5 MPa). The hydrogen permeance of the alloys of interest in this study was determined through a transient analysis monitoring the change in hydrogen concentration of the retentate while a constant concentration was maintained on the permeate side.

Results and Discussion

Kinetic studies. An early work by Graven and Long⁴ addressed the high-Temperature (>850°C), ambient-pressure gas-phase forward Water-Gas Shift Reaction (FWGSR). The authors found that the chain reaction mechanism previously proposed by Bradford⁵ was consistent with their experimental rate expression. For very-low conversions (i.e. <1%), the rate can be expressed as $r = k[H_2O][CO]^{1/2}$. However, the effect of high-pressure was not assessed in that study. Our results for the high-pressure (16 bar) reaction in the quartz reactor confirmed the validity of such form of the rate of reaction (not shown here). Figure 1 compares the Energy of Activation of the high-temperature, high-pressure FWGS with the high-temperature, low-pressure experimental results by Graven and Long; the figure also shows the rate constant obtained from the Bradford mechanism by using the pseudo-steady state approximation (i.e., analytical solution) or from a numerical solution of the concentration profile of each one of the species at low pressure (in both cases the rate constant for each elementary reaction were taken from the GRI kinetic database). There is good agreement between the values of the energies of activation, although the values of the rate constant differ. We are currently studying this behavior. One possible explanation of the higher results by Graven and Long is the occurrence of the Boudouard reaction ($2CO \leftrightarrow C + CO_2$), which would give an artificially higher CO conversion; in our experiment carbon was removed by overnight treatment with oxygen (we found that an induction period of more than 24hr was required for the carbon formation to affect the results). The energy of activation and pre-exponential constants for the high-pressure reaction are 69 Kcal/mol and $1.03 \cdot 10^{11} \text{ l}^{0.5} \text{ mol}^{-0.5} \text{ s}^{-1}$, respectively.

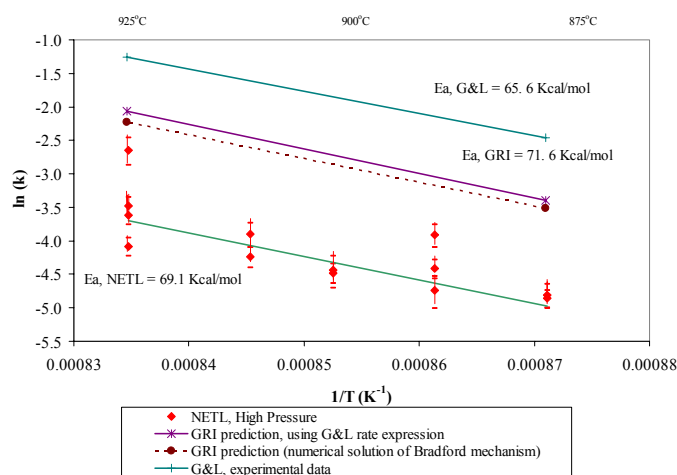


Figure 1. Energy of Activation of the high-temperature, gas-phase Forward Water-Gas Shift Reaction. NETL results: quartz reactor, 16-bar, $(y_{\text{CO}})_0 = 0.8$, $(y_{\text{H}_2\text{O}})_0 = 0.2$, residence time < 4s.

A large increase in H_2O conversion was observed when the reaction was run in the Inconel reactor. Such enhancement in the reaction rate can be related to the Inconel walls; similar behavior was observed for the reverse Water-Gas Shift Reaction². Equilibrium conversions are attained at relatively low temperatures, indicating that the membrane-reactor would be diffusion-limited rather than kinetic-limited. However, parallel reactions (e.g., methanation) become more noticeable under these conditions. Finally, metal dusting is a concern in using Inconel.

Permeation Studies. The hydrogen permeance results of this study are illustrated in Figure 2 as a function of temperature. With the exception of pure palladium, the hydrogen permeance of the 60 wt% Pd/Cu membrane exhibited the highest permeance of the alloy membranes studied at temperatures below 748 K while the 80 wt% Pd/Cu alloy exhibited the highest permeance at temperatures above 748 K. Both the 60 wt% Pd/Cu and 53 wt% Pd/Cu alloy membranes exhibited significant decreases in permeance with respect to temperature through their respective crystalline phase transition from bcc to fcc.

The 60 wt% Pd/Cu and 53 wt% Pd/Cu alloy membranes exhibited unique permeance responses with respect to the temperature induced phase transitions (bcc-fcc). The alloys displayed their highest permeance values at the low temperature, bcc phase. In addition, the permeance of both alloys decreased with temperature through their respective crystalline phase transition (bcc to fcc) while the fcc phases showed similar trends as the bcc phase with respect to temperature.

Decreases in hydrogen permeance greater than an order of magnitude in the presence of hydrogen sulfide were observed for the low-temperature, bcc crystalline phase of the 60 wt% Pd/Cu and 53 wt% Pd/Cu alloys. However, minimal changes were evidenced by the 80, 60, 53 and 40 wt% alloys at temperatures corresponding to the fcc crystalline phase.

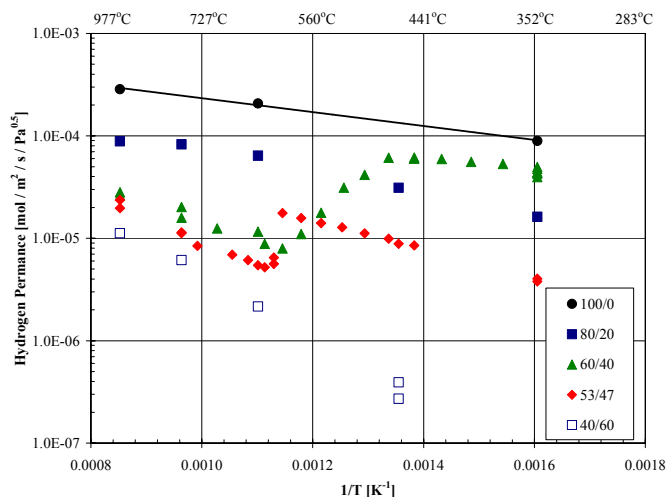


Figure 2. Hydrogen permeance results of several Pd/Cu alloys examined in this study.

Conclusions

The first experimental study of the high-pressure, high-temperature forward Water-Gas Shift reaction was conducted. Additionally the hydrogen permeance of a broad range of Pd/Cu alloy membranes was studied. The performance of the Pd/Cu membranes in the presence of sulfur was determined. Both the kinetics and permeance are required to evaluate the feasibility of a Water-Gas Shift membrane reactor at gasifier conditions. The finding of this study may be summarized as follows:

- The high-temperature, high-pressure forward Water-Gas Shift reaction appears to follow the same chain reaction mechanism than the low-pressure reaction. However, a negative influence of the high-pressure on the rate of reaction was observed. Current research efforts are underway to explain this phenomenon.
- The crystalline phase of the Pd/Cu alloys was found to have a great impact on the permeance of hydrogen both in the presence and in the absence of H_2S . Alloys with the fcc crystalline phase exhibit a higher sulfur-tolerance.

Acknowledgement. This work is supported through the "Gasification Technologies" and "Transportation Fuels and Chemicals" product lines at NETL.

References

- (1) Enick, R.; Morreale, B.; Hill, J.; Rothenberger, K.; Cugini, A.; Sriwardane, R.; Poston, J.; Balachandran, U.; Lee, T.; Dorris, S.; Graham, W.; Howard, B. In: *Advances in Hydrogen*; Kluwer Academic/Plenum Publishers, New York, 2000; pp 93-100.
- (2) Bustamante, F.; Enick, R.; Cugini, A.; Killmeyer, B.; Howard, B.; Rodgers, W.; Rothenberger, K.; Ciocco, M.; Morreale, B.; Shi, S. *AIChE J.*, in review.
- (3) Morreale, B.; Ciocco, M.; Enick, R.; Morsi, B.; Howard, B.; Cugini, A.; Rothenberger, K. *J. Membr. Sci.* **2003**, 212, 87.
- (4) Graven, W.; Long, J. *J. Am. Chem. Soc.* **1954**, 76, 26602, 6421
- (5) Bradford, B. *J. Chem. Soc.* **1933**, 1557.

AN OLD/NEW APPROACH TO THE PARTIAL OXIDATION OF ALKANES

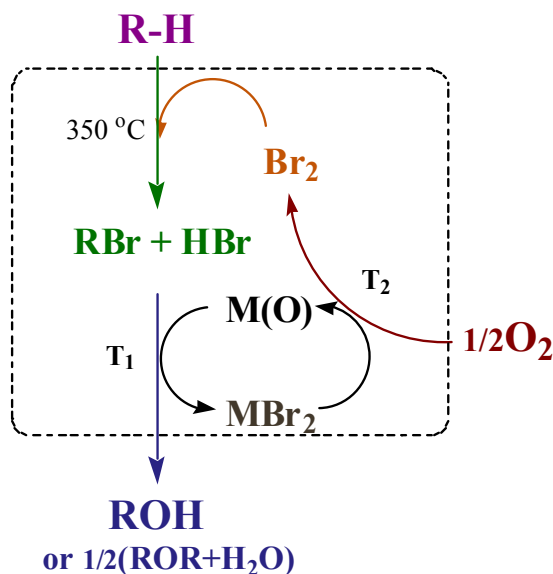
P. C. Ford, P. Grosso, L. Laverman, I. M. Lorkovic, E. W. McFarland, D. Schaefer, J. H. Sherman, G. D. Stucky, S. Sun, M. Weiss, A. Yilmaz, G. Yilmaz, X. P. Zhou)

Departments of Chemistry and Biochemistry and of Chemical Engineering, University of California, Santa Barbara, CA 93106
GRT, Inc., 5662 Calle Real #373, Santa Barbara, CA 93117

Introduction

The transformation of natural gas feedstocks to higher value compounds continues to present an important intellectual challenge with strong economic rationales. Here we describe a new integrated, multi-step process for the selective partial oxidation of alkanes to alcohols, ethers or alkenes that provides unprecedented product control.

These transformations are carried out in a sequential zone flow reactor (SZFR) and involve bromination of alkane to alkyl bromide(s) and HBr followed by reaction of this mixture with a solid metal oxide (MO) to neutralize the HBr and generate oxygenated products (alcohols or ethers) or alkenes plus solid metal bromide and, lastly, oxygenation of the spent solid to regenerate the MO and Br₂ for reuse (Scheme 1)



Thus, the overall transformation of alkane to alcohol, ether, or alkene utilizes dioxygen as the ultimate oxidant, for example:



Results and Discussion

The key to the successful partial alkane oxidation reported here is the use of a solid transition metal oxide (or MO mixture) on a stable support to react with the alkyl bromide and effect bromide/oxide metathesis under mild conditions. While others have considered related approaches, the integration of these steps into a single scheme is unique. Furthermore, the specific MO mixture composition determines product distribution and thus provides

unprecedented product control, especially with feedstocks other than methane. For example, with ethane certain MO compositions and reaction conditions give mostly alcohols or ethers (see below), while others give predominantly ethylene or acetaldehyde.

The SZFR consists of two serial fixed bed reactors. In the first, a stream of Br₂ and excess alkane (1-3 bar) reacts over glass beads (60-120 mesh) at 350 °C, and the Br₂ is fully consumed. Then the resulting alkyl bromide(s), HBr and excess alkane are directed into the second reactor containing supported metal oxide at T₁ (200-250 °C). The exiting products are identified and analyzed by ¹H-NMR and GC (with MS, TCD or FID detection) techniques. Longer runs demonstrate that most of the oxide equivalents can be utilized. After the metathesis capacity is largely consumed, O₂ is passed into the second reactor at T₂ (300-500 °C) to regenerate the MO and Br₂. The bromide retained on spent solids was quantitatively recovered as Br₂ (This procedure also releases CO₂ from carbon deposited during the metathesis.) Repetitive runs (> 10) cycles with regenerated MO showed no loss of activity. Material balances were established for bromine and carbon.

Examples of effective solid reactants for oxide/bromide metathesis are 50/50 CuO/ZrO₂ (MO-1) and 43/7/50 Co₃O₄/Sm₂O₃/ZrO₂ (MO-2). Products from these two differ considerably. MO-1 gives predominantly alcohols and more deep-oxidation to CO₂, while MO-2 gives largely ethers. For example, a 10:1 methane:Br₂ feed to a reactor containing MO-1 (3.6 g) led to 8.1% conversion with comparable amounts of CH₃OH (37%), CO₂ (35%) and unconverted CH₃Br (29%) in the product stream. A similar run with MO-2 gave CH₃OH (20%), (CH₃)₂O (20%), CO₂ (5%), and unconverted CH₃Br (40%) and CH₂Br₂ (15%). Reaction of pure CH₃Br with MO-1 or MO-2 generates some CO₂ due to reduction of metal center oxidants (Cu(II) or Co(III), respectively). Larger CO₂ yields in the integrated system are attributed to reactions of polybrominated methanes, and can be addressed by improving bromination selectivity by introducing electrophilic catalysis or otherwise optimizing reaction conditions.

Experiments with ethane:Br₂ streams give less CO₂ and a richer product array. EtOH and Et₂O are the principal products, others include ethylene, acetaldehyde, vinyl bromide, ethyl acetate and butadiene, as well as unreacted EtBr. The relative yields are sensitive to MO composition and specific reaction conditions; e.g., MO-1 favors EtOH, MO-2 favors Et₂O, while other oxides and higher T₁ give very high selectivities for ethylene

Ongoing studies are focused on improving overall conversion and controlling product selectivity and include investigations of bromination catalysis and the design and optimization of metathesis solids and conditions.

Acknowledgement. This research was supported by a sponsored research agreement between GRT Inc. and UC Santa Barbara.

SYNGAS QUALITY IN GASIFICATION OF HIGH MOISTURE MUNICIPAL SOLID WASTES

Yongseung Yun, Seok Woo Chung, and Young Done Yoo

Plant Engineering Center
Institute for Advanced Engineering
633-2, Goan-ri, Baegam-myeon
Yongin, Gyeonggi-do, 449-863 Korea

Introduction

With widespread environmental concerns among non-technical people around the conventional incinerators in city areas, it becomes more and more difficult to get permission for new municipal solid wastes (MSW) treatment facilities in Korea like many other countries. Although dioxins are not a problem anymore technically because of the added SCR facility in reducing dioxins below the environmental regulations of 0.1 ng/Nm^3 , residents in Korea still remain skeptical and start to insist that advanced technologies should be employed in order to build a new MSW treatment facility in their backyard. Germany and Japan are in the front of building MSW plants applying advanced technologies like pyrolysis, gasification, and melting. In applying the advanced technologies into Korean MSW that has unique features in composition like high moisture content due to waste vegetables, which in turn result in low heating value of MSW, there are great demand in proving the technology with actual Korean MSW before introducing major scale plants of 150-600 ton/day size.

During the last few years, newly enforced waste separation policy in major cities in Korea yielded an increased heating value of MSW as high as 3,000 kcal/kg. Since small cities are still in lag behind of following wastes separation policy, gasification plants in Korea should have a room to treat the low heating value waste quality at least for the introductory plants. Following the ever-increasing heating value in MSW that can be recovered as an alternative energy source, it appears that installing advanced MSW technology plants are inevitable in Korea in the next few years. In this paper, current research status of gasification using MSW of high moisture content is discussed.

Gasification Facility

Figure 1 shows the 3-D view of 2.5 ton/day-class gasification facility that was being developed for the municipal solid wastes. Maximum pressure and temperature for the operation are 1 bar and 1550°C , respectively.

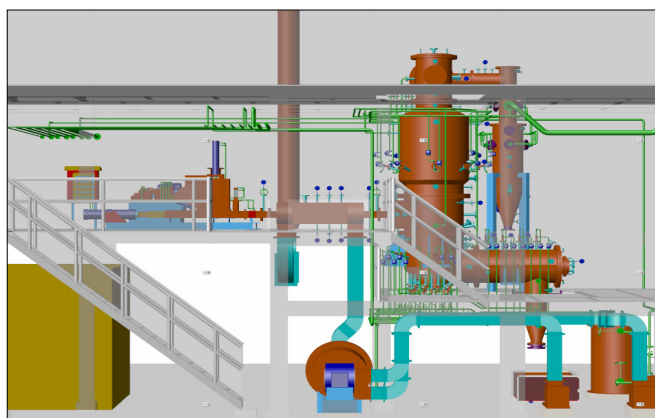


Figure 1. 3-D design view of the 2.5 ton/day MSW gasification system.

Plant consists of feed accepting apparatus, MSW compacting section, partial pyrolysis section, gasification/melting reactor part, slag homogenizing section, and quick syngas quenching section. Feed is introduced into the plant as 20 liters vinyl bags that are one way to discard MSW in Korean cities, after which MSW vinyl bags are compressed and pushed into the partial pyrolysis section in that few centimeters of surface parts are carbonized. During the compressing operation, about 10-30% of the moisture in MSW are extracted. Extracts are scavenged and pumped into the end section of the partial pyrolyzing section. Main gasification section works with LPG burners located at the bottom part of the reactor. Molten slag flows into the slag homogenizer that works to ensure the melting of all inorganic components and finally drops into the water-quenching chamber to produce slag. Gasifier temperature is maintained typically in $1,200\text{--}1,450^\circ\text{C}$ range while the slag homogenizer in $1,400\text{--}1,550^\circ\text{C}$.

Figure 2 exhibits key components of the plant (Left: gasifier section, Right: slag homogenizer). Gasifier contains two layers of refractories with water cooling pipes and jackets around the main gasification area. Pure oxygen is provided after vaporizing and compressing from liquefied oxygen storage tanks.

High moisture-containing MSW from Y-City in Korea has an average high heating value of 2,176 kcal/kg (as-received basis) with 55.8% moisture and 6.9% ash. Components of MSW in weight were 46.8% kitchen food wastes, 27.1% paper, 5.9% textiles, 11.1% vinyls, 2.3% plastics, 6.9% glass and porcelain. Another tested MSW of medium moisture from K-City in Korea contains 50.4% moisture, and 5.5% ash with HHV of 2,686 kcal/kg. Components of K-City MSW consist of 29.6% kitchen food wastes, 33.7% paper, 9.7% textiles, 19.5% vinyls, 5.6% plastics, 1.9% foam materials.

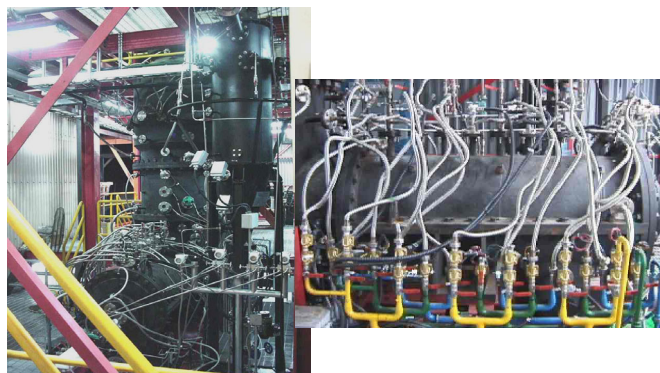


Figure 2. Gasification section (left) and the slag homogenizing section (right) of the pilot gasification facility.

Results and Discussion

Gasification results for the 55.8% moisture-containing MSW are illustrated in **Figure 3**. Syngas composition shows CO 25-30%, 20-35% hydrogen, and 22-40% CO_2 .

Figure 4 demonstrates typical waste compositions and produced syngas quality from similar types of gasification plants of Italy, Japan, and Germany. Korean MSW contains highest moisture content followed by Japanese MSW near 50%. MSW from European countries exhibits less than 30% moisture, but much higher inorganic composition of reaching 25% compared to less than 8% in Korea and Japan. As expected, high moisture containing MSW yielded lower CO/H_2 and higher CO_2 contents, which result in lower heating value in syngas. Gasification of Korean MSW produces a syngas of typical 26-28% CO and hydrogen composition with a HHV $1,640 \text{ kcal/Nm}^3$. In this case, cold gas efficiency based upon HHV was 53%.

Figure 5 shows gasification results for the 50.4% moisture-

containing Korean MWS from the K-City where most of food wastes are separated and reusable materials are recycled. Most of moisture originated from soaked rain during storage in K-City.

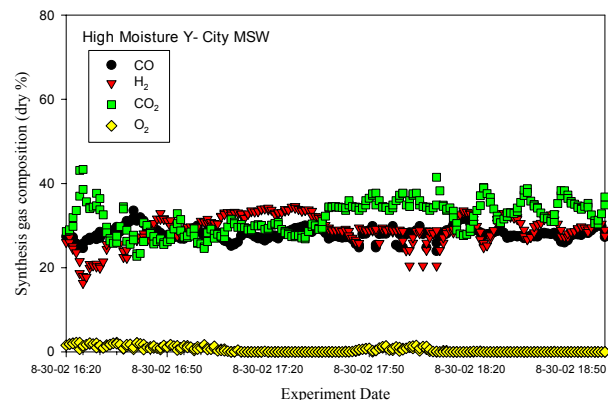


Figure 3. Syngas compositions from gasification of 55.8% moisture MSW from Y-City in Korea.

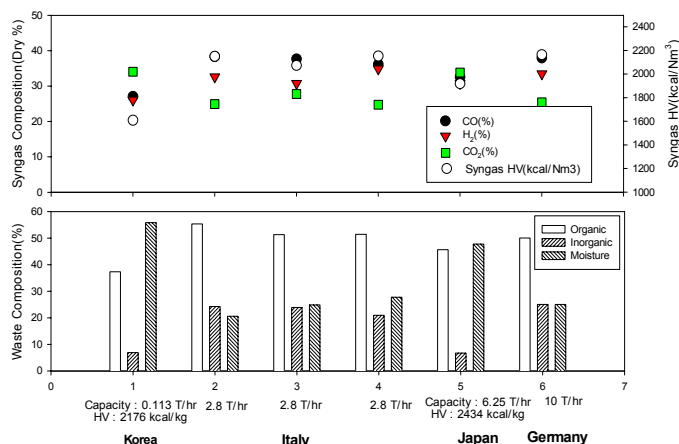


Figure 4. Comparison of syngas composition and heating value by similar types of gasification for MSW from several countries.

Moreover, the MSW in K-City contains more papers and less kitchen wastes than Y-City MSW and thus providing more organics feed for gasification at the same weight basis. Resulting syngas composition demonstrates a higher heating value in syngas as 2,125 kcal/Nm³ with 38% CO and 32% hydrogen contents. Energy content in syngas from K-City MSW is almost as high as heating value from coal gasification. Therefore, with appropriate cleanup steps, the produced syngas can be utilized as a good alternative energy source.

Slags produced from high moisture Y-City MSW are shown in **Figure 6** in that few mm of round and sharp-edged shapes are illustrated.

To utilize slags for construction materials, they should fulfill the requirements in environmental leaching regulation. **Table 1** demonstrates that produced slags are environmentally safe in leaching tests. Please note that Korean leaching regulations are about ten times less stringent than in Japan and other developed countries. The results in Table 1 exhibit that even more stringent regulations can be met through the gasification/melting process.

Conclusions

Experience in coal gasification during the last ten years has been successfully applied for the MSW gasification/melting pilot plant.

Gasification for Korean MSW of high moisture content yielded a syngas comprising of 22-40% CO and 25-38% hydrogen with a heating value equivalent of syngas from coal gasification. Since energy grade in MSW would increase above 3,000 kcal/kg in major cities, advanced gasification/melting process for MSW appears to be an inevitable choice in Korea based upon the option of producing clean energy without polluting environment as well as the people's wish for advanced technology that ensures less pollutants in their backyard.

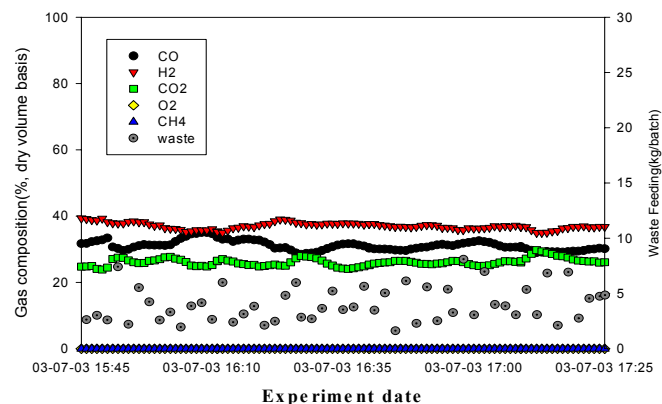


Figure 5. Syngas compositions from gasification of 50.4% moisture MSW from K-City in Korea.



Figure 6. Produced slags by gasification/melting from high moisture Y-City MSW (unit: cm).

Table 1. Leaching Test Results for Slags from Y-City MSW

Item	Unit	Result	Korean Environmental Standards
Total Hg	mg/l	n.d.	0.005
Cd	mg/l	n.d.	0.3
Pb	mg/l	0.03	3.0
Cr ⁺⁶	mg/l	n.d.	1.5
As	mg/l	n.d.	1.5
Se	mg/l	n.d.	-
Tota CN	mg/l	n.d.	1.0
Organo-phosphrous	mg/l	n.d.	1.0
Alkyl-mercury	mg/l	n.d.	-
PCB	mg/l	n.d.	-
Trichloroethylene	mg/l	n.d.	0.3
Tetrachloroethylene	mg/l	n.d.	0.1

Acknowledgement

This work was supported in part by KISTEP as one of National Research Lab. Projects in Korea under the contract 2000-N-NL-01-C-224.

SIMULATION TOOLS FOR THE DESIGN OF VISION 21 ENERGY PLANTS

Thomas J. O'Brien[†], Stephen E. Zitney[‡], William Rogers[†], and
Anthony Cugini[†]

[†]National Energy Technology Laboratory
3610 Collins Ferry Road
Morgantown, WV 26507-0880

†Fluent, Inc.
3647 Collins Ferry Road
Morgantown, WV 26505

Introduction

The development of energy systems that use fossil fuels efficiently is needed to achieve the energy goals of the U.S. through the twenty-first century. The demands of environmental stewardship require placing a greater emphasis on clean energy options while, at the same time, global competitiveness creates a market atmosphere that rewards cost-effectiveness. In addition, the time and expense of developing and demonstrating new technological systems must be reduced. With tightening research budgets, the use of numerical simulation offers an effective supplementary approach to aid in the design, development, and evaluation of new clean energy technologies.

Currently, many modeling and simulation tools are being used for energy technology development. These are being integrated into platforms for performing complete virtual demonstrations of advanced fossil energy systems. Integration of existing modeling tools is the largest development need. At present, most process engineering applications for systems architectural and engineering designs, heat and mass constitutive simulations, cost estimations, and synthetic environment visualizations are self-contained, and each provides its own user interface. Integration of these tools within a virtual reality structure will provide a powerful cost-reducing tool to examine Vision 21 energyplex options.

At the heart of this development is the challenge of bridging the time and length scales that relate microscopic scientific understanding to macroscopic engineering design, an issue frequently addressed by quantum chemists^{1,2}. For example, continuum solvation models based on quantum chemical calculations of the individual compounds in a mixture are being used to calculate thermodynamic properties of fluid mixtures³. Such fundamental models should become a valuable supplement for the well-established methods used in engineering design, namely group contribution methods, other activity coefficient models, and equation-of-state models. In addition, it should now be feasible to use the results of quantum chemical calculations to predict rate constants and thermodynamic data required for chemically reactive computational fluid dynamics, which can now be coupled with process simulation. This process requires the systematic reduction of higher-order models to consistent lower-order models, which can then be utilized in analysis at the larger scale.

For example, Vision 21 simulations of fuel cell processes consider a hierarchy of models ranging from molecular-level models to component-level models to overall system models. Molecular-level models are focused on phenomena occurring at the surface of the fuel cell membrane. Component models (e.g., fuel cell, reformer, gasifier) range from models based on engineering correlations to complex computational fluid dynamics (CFD) models that consider the hydrodynamics, heat transfer, multicomponent transport, electrochemical kinetics, and current distribution in a fuel cell^{4,5}. Such models are required to optimize the design of individual

components in a fuel cell process (e.g., reactor geometry, fuel distributor design, temperature distribution). System-level models or process simulations describe the combined performance of all the components in the fuel cell process^{6,7,8,9}. Process simulators are primarily used to perform material and energy balances on the tightly integrated fuel cell flowsheets. Such models are useful for addressing system-level design questions (e.g., recycle stream options, heat integration, overall system efficiency).

Integration of CFD and Process Simulation

Two potential strategies for bridging the gap between component-level models (i.e., CFD) and system-level models (i.e., process simulation) include:

- 1) The CFD package and process simulator model *different components* and exchange consistent physical properties (e.g., density, viscosity, heat capacity, thermal conductivity) and reaction kinetics (e.g., Arrhenius rate parameters), as well as stream information (e.g., flow rate, composition, temperature, pressure) at flow boundaries¹⁰.
- 2) The CFD package and process simulator model the *same component*, but different physical phenomena¹¹. In this case, the process simulation model typically sends physical and transport property data (e.g., density, viscosity) to the CFD model, which in turn sends back flow-dependent information (e.g., turbulent kinetic energy). This strategy also includes the case where a CFD model of a single unit operation is represented by an interconnected network of models in the process simulator¹².

In this paper we present a framework for coupling two widely used simulation tools: FLUENT™ for CFD modeling and Aspen Plus® for process simulation. The software integration is accomplished using the standard CAPE-OPEN interfaces¹³ (see www.colan.org). Osawe et al.¹⁴ presented the details of the integration. Zitney and Syamlal¹⁰ presented an example of a reaction-separation-recycle flowsheet coupled with a CFD stirred tank reactor model. They determined an optimum shaft speed (a CFD model parameter) for maximizing the overall rate of production of one of the products – a task that could not have been done by using either of the tools alone. On going work on simulating a power plant using the integrated software system is described by Sloan et al.¹⁵

Example Applications

Several applications are presented below which illustrate the present capability of this framework for integrating simulations tools for the design of potential Vision 21 components.

PEM Fuel Cell. As shown in Figure 1, this Aspen Plus application is a natural gas based PEM (proton exchange membrane) fuel cell power system, consisting of a reformer, shift converter, fuel cell, anode exhaust combustor and heat exchangers.

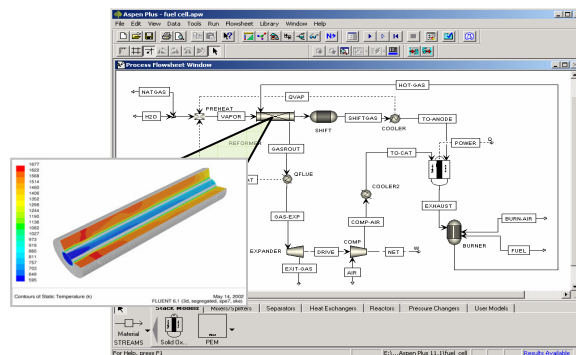


Figure 1. PEM Fuel Cell Power System

The reformer is heated with hot gases from the anode exhaust burner. The reformer is modeled with a single-step Arrhenius reaction: $\text{CH}_4 + \text{H}_2\text{O} \rightarrow \text{CO} + 3 \text{H}_2$ and simulated using a 3D CFD model that predicts conversions that account for the limitations imposed by the heat transfer to the catalyst bed. The use of the integrated CFD and process simulation enables the design engineer to study the effect of the recycled hot gases on the PEM CFD model performance¹⁶.

SOFC Fuel Cell. Prinkey et al.^{17,18} and Rogers et al.¹⁹ describe the development and validation of the NETL solid-oxide fuel cell (SOFC) model based on the FLUENT CFD code. The models for electrochemistry, electron transport (current) and porous media diffusion were implemented using the user-defined functions capability of FLUENT. Figure 2 shows the SOFC power system flowsheet in Aspen Plus, along with the distribution of H_2 mole fractions in the fuel stream passing along the fuel cell anode¹⁶. The hydrogen-rich flow enters from the bottom left and is gradually depleted as it proceeds towards the exhaust ports.

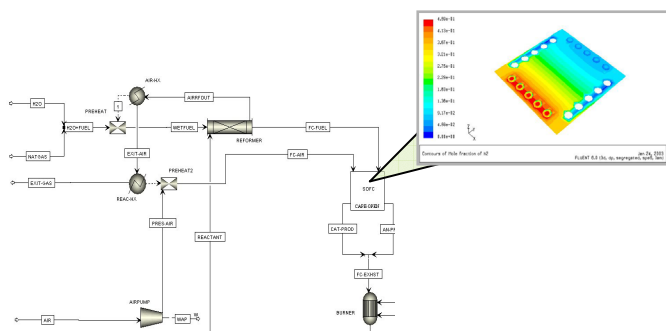


Figure 2. SOFC Fuel Cell Power System

Since the SOFC CFD model applied in this example represents a single cell, the other flowsheet components have been downscaled accordingly. Future work will include fuel cell stacks that produce electrical output on a more useful scale.

Coal Gasification. Gasification technology is essential for many schemes for the efficient and environmentally benign generation of power from a range of fuels, including coal and biomass. Specifically, they are the central component of several large-scale Integrated Gasification and Combined Cycle (IGCC) demonstration plants. Currently, detailed CFD gasification simulations are being performed which are being used for the analysis of large-scale facilities²⁰.

The CFD simulations account for the gas and particle dynamics, chemical reactions and heat transfer. They are used to study the flow of hot gas and unburned solids as it moves from the mixing zone into the riser of a circulating fluidized bed. The hydrodynamics of both the gas and solid phases are tracked, along with heat transfer between the two phases and production of gas species, such as methane, carbon monoxide and carbon dioxide. Design engineers use the CFD simulations to see how design changes affect the hydrodynamics and the chemistry in the gasifier. Future work will include integrating CFD models for gasification and fuel cell stacks into overall Vision 21 plant simulations.

Conclusions

This paper described the integration of CFD and process simulation tools for use in the design of energy plants. Such integrated simulations offer the ability to optimize individual components in the context of the entire power system rather than in isolation. Early results have demonstrated the potential for improved process design. Continued focus on seamless integration between process simulation,

CFD, and other simulation tools will present many new opportunities to design Vision 21 plants based on the fundamental principles of fluid flow, heat and mass transfer, chemical reactions, and other related phenomena, further enhancing the performance and efficiency of future energy plants.

Acknowledgement

This work was supported by U.S. Department of Energy, Office of Fossil Energy, National Energy Technology Laboratory.

References

- (1) Wang, Q.; Johnson, J.K.; Broughton J.Q., *Computers in Physics*, **1998**, 12 (6), 538.
- (2) Clementi, E., *Philos. Trans. R. Soc. London, Ser. A*, **1988**, 326, 445.
- (3) Klamt, A., Presented at *Thermodynamics 2003*, Cambridge, UK, April 9-11, 2003.
- (4) Um, S.; Wang, C.-Y.; Chen, K. S., *Journal of The Electrochemical Society*, **2000**, 147(12), 4485-4493.
- (5) Prinkey, M.T.; Gemmen, R.S.; Rogers, W.A., *American Flame Research Committee (AFRC) International Symposium*, Newport Beach, CA, USA, September 2000.
- (6) Fontes, E.; Nilsson, E., *The Industrial Physicist*, August/September, **2001**, 14-17.
- (7) Fuller, T.A.; Chaney, L.J.; Wolf, T.L.; Kesseli, J.; Nash, J.; Hartvigsen, J., Presented at the *2000 Fuel Cell Seminar*, Portland, OR, October 30 – November 2, 2000.
- (8) Keegan, K.; Khaleel, M.; Chick, L.; Recknagle, K.; Simmer, S.; Deibler, J., Presented at the *SAE 2002 World Congress*, Detroit, MI, March 4-7, 2002.
- (9) Virji, M.B.V.; Adcock, P.L.; Mitchell, P.J.; Cooley, G., *Journal of Power Sources*, **1998**, 71, 337-347.
- (10) Zitney, S.E.; Syamlal, M., *Proc. of the European Symposium on Computer Aided Process Engineering –12, ESCAPE-12*, Grievink, J.; van Schijndel, J., Eds., **2002**, 397-402.
- (11) Bezzo, F.; Macchietto, S.; Pantelides, C.C., *Computers and Chemical Engineering*, **2000**, 24, 653.
- (12) Urban, Z.; Liberis, L., Presented at *Chemputers Europe 5 Conference*, October 21-23, Dusseldorf, Germany, 1999.
- (13) Braunschweig, B.L.; Pantelides, C.C.; Britt, H.I.; Sama, S., *Chem. Eng. Progress*, **2000**, 96(9), 65.
- (14) Osawe, M.O.; Felix, P.; Syamlal, M.; Lapshin, I.; Cleetus, K.J.; Zitney, S.E., Paper No. 250c, Presented at the *AIChE 2002 Annual Meeting*, Indianapolis, IN, November 3-8, 2002.
- (15) Sloan, D.G.; Fiveland, W.A.; Zitney, S.E.; Syamlal, M., Presented at *The 27th International Technical Conference on Coal Utilization & Fuel Systems*, Clearwater, Florida, March 4-7, 2002.
- (16) Syamlal, M.; Madsen, J.I.; Zitney S.E.; Rogers, W., Presented at the *AIChE Spring National Meeting*, Session [102], New Orleans, LA March 30 - April 3, 2003.
- (17) Prinkey, M.; Gemmen, R.; Rogers, W., In *Proceedings of IMECE: ASME 2001 International Mechanical Engineering Congress and Exposition*, New York, NY, November 11-16, **2001**, No. 2-6-4-3.
- (18) Prinkey, M.T.; Gemmen, R.S.; Rogers, W.A., *American Flame Research Committee (AFRC) International Symposium*, Newport Beach, CA, USA, September 2000.
- (19) Rogers, W.A.; Gemmen, R.; Johnson, C.; Prinkey, M.; Shahnam, M., Presented at U.S. DOE NETL, RIT Meeting, 2003.
- (20) Guenther, C.; Shahnam, M.; Syamlal, M.; Longanbach, J.; Cicero, D.; Smith, P., *Proceedings of the 19th Annual Pittsburgh Coal Conference*, Pittsburgh, PA, Sept. 23-27, 2002.

Effect of Hydrogen Donor on the Morphology of Carbon Formed During Pyrolytic Stressing of JP-8 Jet Fuel

James J. Strohm, Abraham J. Brandt, Semih Eser
and Chunshan Song*

The Energy Institute and The Dept. of Energy and Geo-
Environmental Engineering, The Pennsylvania State University
209 Academic Projects Building, University Park, PA 16802
*E-mail: csong@psu.edu

Introduction

In the future, jet fuel used by high-Mach aircraft will be expected to perform a dual role as a coolant for mechanical and electrical systems, raising temperatures experienced by the fuel to greater than 480°C.¹ Current jet fuels are derived from petroleum sources resulting in a predominately paraffinic fuel. At these temperatures, linear paraffins are highly susceptible to pyrolytic degradation leading to the formation of carbon deposits² on metal surfaces within the aircraft through bulk and/or catalytic reactions.

Bulk deposits that are formed are generally due to the condensation of alkyl benzenes either present in the fuel or formed from pyrolytic dehydrogenation reactions, which results in deposits that have a general structure of 6 to 7 aromatic rings.³ Previous work has shown hydrogen donors such as tetralin and α -tetralol can reduce such pyrolytic reactions under non-oxidative conditions, thus effectively reducing the formation of bulk deposits.^{4,5} The presence of dissolved oxygen in the fuel dramatically lowers the effectiveness of such hydrogen donors in the pyrolytic regime, rendering them useless.⁵ Recently, a binary hydrogen donor consisting of α -tetralone and tetralin has shown excellent oxidative resistance while significantly preventing the formation of polyaromatics.^{6,7}

Catalytic deposition is associated with adsorption and subsequent reactions on metal surfaces resulting in filament or amorphous carbon growth. Composition of the metal surface has a profound effect on the formation rate and structure of deposits.^{8,9} Superalloys based on the group VIIIA elements were developed for high-temperature applications in corrosive environments, and have been used successfully in aircraft parts and nuclear reactors.¹⁰ However, these alloys still contain Ni and Fe, which are known to catalyze the growth of carbon filaments.¹¹

The current study seeks to investigate the effect of the previously developed binary hydrogen donor on the morphology of carbon deposits formed on the superalloy, Inconel 718, during stressing of JP-8 under pyrolytic conditions while dissolved oxygen is present in the fuel.

Experimental

Thermal stressing of JP-8 fuels was performed in the presence of Inconel 718 foils, whose elemental composition is listed in Table 1. For each experiment a foil having dimensions of 10 x 3 x 0.1 mm was placed at the bottom of a 1/4" o.d. isothermal flow reactor, lined with a Silcosteel[®] coating developed by Restek Corporation. Prior to introducing fuel into the system, the reactor was heated to 500°C wall temperature under argon flow at 500 psig.

Table 1. Elemental Composition of Inconel 718^{a,b}

Al	Cr	Cu	Fe	Mn	Mo
5000	19%	1500	18.5%	1800	3.05%
Nb+Ta	Ni	Si	Ti	C	S
5.13%	52.5%	1800	9000	400	80

^aFrom Goodfellow Co. and expressed in weight percent. ^bAl, Cu, Mn, Si, Ti, C and S in ppm.

The fuels used in this study were 1 L of JP-8 with and without a 2 wt% addition of the binary hydrogen donor consisting of equal

amounts of α -tetralone (THNone) and tetralin (THN). Each fuel was circulated through the reactor at a rate of 4 mL/min for a period of 24 hrs. The fuel was heated to 200°C before entering the reactor, and the bulk outlet temperature of the fuel was maintained at 500°C. Pressure was held constant at 500 psig, and liquid fuel samples were taken at six-hour intervals.

Carbon deposits on the metal foils were analyzed using a LECO R412 Carbon Analyzer to determine total amounts of carbon on the surface in $\mu\text{g}/\text{cm}^2$. Morphology of deposits was characterized by a Hitachi S-3500N scanning electron microscope. A Shimadzu GC-174 gas chromatograph with a Restek Xti-5 column coupled to a Shimadzu QP-5000 mass spectrometer was used to examine liquid samples. Solution state ¹³C-NMR analysis was conducted on a Bruker AMX360 with a field of 8.4 T equivalent to a 90 MHz resonance frequency for ¹³C. Approximately 0.2 mL of sample was diluted in 1 mL CDCl₃ and charged into a 5 mm tube. A pulse delay of 90 seconds was required to obtain a quantitative spectrum.

Results and Discussion

Impact on Fuel Reactions. Previous investigations of binary hydrogen donors have shown large improvements in preventing pyrolytic reactions leading to polyaromatic formation and bulk deposits. In a separate flow reactor system JP-8 was stressed with and without the binary hydrogen donor added to the fuel. Silcosteel was used to passivate the surface, in order to minimize catalytic decomposition of the fuel. The reactor utilized higher space velocities, leading to higher temperature conversions, which allowed direct examination of fuel and hydrogen donor interactions. Figure 1 shows the impact of the binary hydrogen donor on the final fuel composition when the fuel was stressed up to a bulk outlet temperature of 772°C (with a LHSV = 450 hr⁻¹).

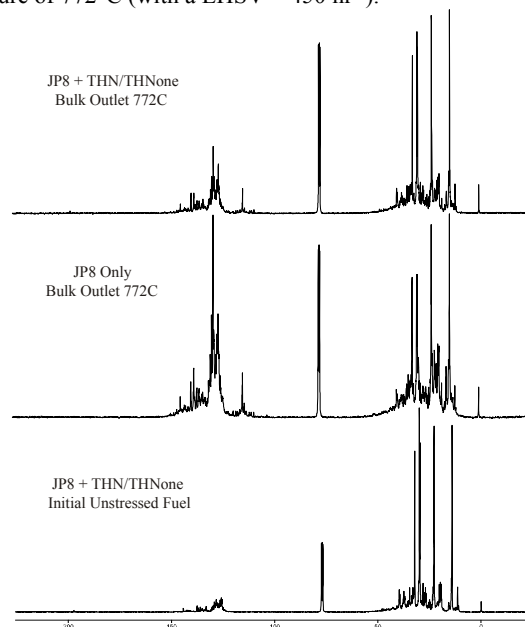


Figure 1. Impact of a binary hydrogen donor on the stabilization of pyrolytic reactions leading to the formation of PAHs as illustrated by ¹³C-NMR analysis of the stressed fuels.¹²

As Figure 1 illustrates, there is a clear increase in the prevention of the total aromatic carbon that is formed when the binary hydrogen donor is added (32% reduction). More significantly, there is a 62% reduction in the formation of bridgehead carbon associated with PAH formation. In the base of the aliphatic region of the spectra, there is

an increased broadening indicating increased cyclization of the initial fuel. Overall, the signature of the JP-8 remains more intact upon stressing when the hydrogen donors are added to the fuel; clearly this indicates a decrease in the decomposition of the fuel, and subsequent formation of precursors to bulk deposits.

Impact on Carbon Formation. TPO investigation of carbon produced on the surface of the Inconel 718 foils showed no difference in the total amount of carbon produced when the binary hydrogen donor was added to the JP-8. The TPO profiles, however, indicated that carbon produced when the hydrogen donor was added were indeed different from the carbon produced in its absence. To further examine the morphology of the carbon produced, SEM analysis was conducted and is presented in Figure 2.

With the addition of the binary hydrogen donor to JP-8, there is enhanced formation of filamentous carbon when compared to the stressing of JP-8 only. Previous work has shown

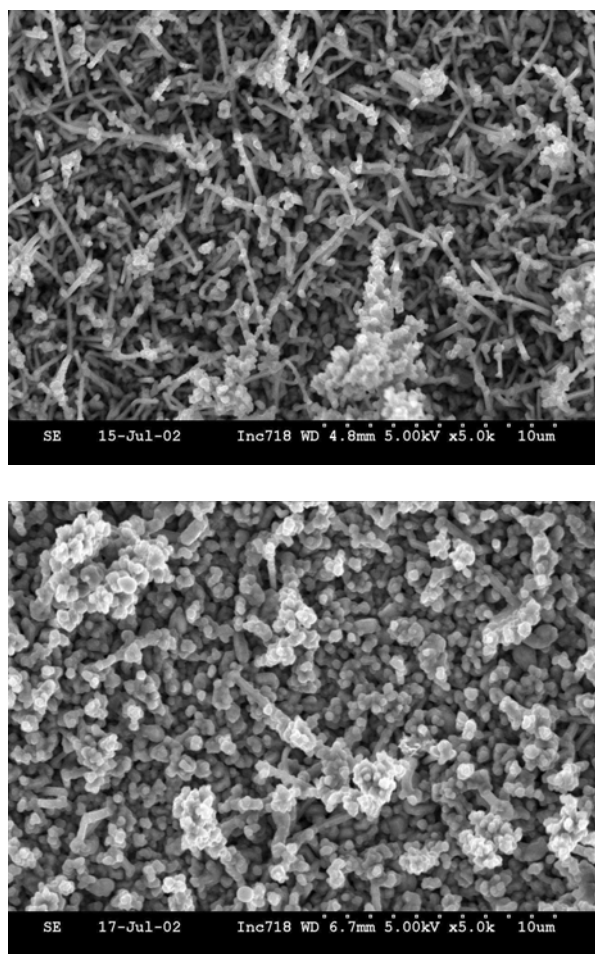


Figure 2. Scanning Electron Micrographs of deposits on the surface of Inconel 718 after thermal stressing for 24 hrs in the presence of JP-8 with (top) and without (bottom) hydrogen donors.

that filamentous carbon is due to catalytic reactions of metals such as nickel and iron with reactive species from thermal decomposition of the fuel.⁹ Research in the field of steam reforming of hydrocarbons over nickel catalyst have shown that filament growth is due to the adsorption and diffusion of carbon through nickel particles.¹³ When the particles of nickel are encapsulated by polymeric carbon, the activity (and growth of the filaments) is reduced. A similar explanation is given here for the observed differences in the carbon

produced from the thermal stressing of JP-8 with and without hydrogen donor addition.

Stressing of JP-8 without the hydrogen donor shows very short and fat carbon filaments with regions of highly amorphous carbon. It is proposed that the reason for the short filaments and amorphous carbon is due to the lay-down of polyaromatics on the surface. This lay-down of polyaromatics will terminate the catalytic activity of active metals such as nickel, resulting in the termination of filament growth. In addition, the initial lay-down of polyaromatics will facilitate an increase in amorphous deposits, due to increasing condensation and dehydrogenation reactions propagating on the surface that is already coated with amorphous deposits. This also accounts for the “regions” rather than irregular coverage of amorphous carbon that was observed on the surface when hydrogen donor is added to the fuel.

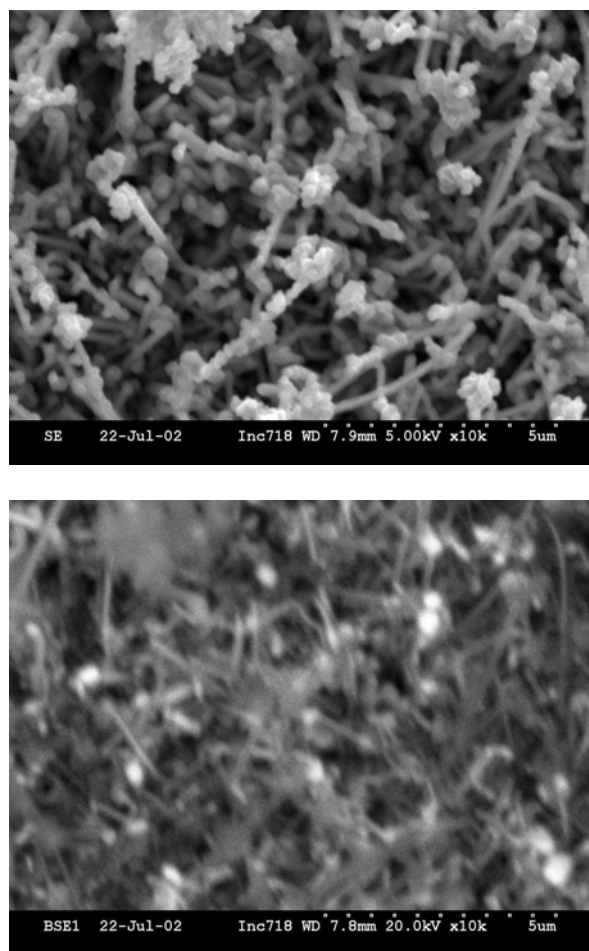


Figure 3. Scanning Electron Micrographs using secondary electrons (top) and back-scattered electrons (bottom) of deposits on the surface of Inconel 718 after thermal stressing for 24 hrs in the presence of JP-8 plus a 1% mixture of α -tetralone and tetralin.

Without the encapsulation of the active metal particles by polyaromatic lay-down, or by active hydrocarbon species from the degradation of the fuel polymerizing, the filaments can continue to grow. This is the case that is observed when hydrogen donors are added to the fuel. The decrease in the formation of polyaromatics, and the suppression of radical reactions that serve to enhance carbon

deposition prevent the encapsulation of active metals, thus allowing enhanced filament growth.

To confirm that metal species were present at the tips of the filaments that were growing, back-scattered electron (BSE) images from SEM analysis were investigated. Figure 3 shows a typical SEM image (top) of the surface after stressing of JP-8 with hydrogen donor addition and the corresponding BSE image of the same area. The light areas of the BSE image correspond to heavy elements that are present on the surface. It is seen that the ends of some of the filaments observed from the SEM image have light areas associated with them in the BSE image. Since the only heavy elements that would be present in the system would be metals, it is shown that these filaments do have metals located near their tips. Not all of the filaments show light areas near their tips, and this is due to some of the filaments being encapsulated by carbon, thus terminating the filament growth as seen in the SEM image of Figure 3.

Conclusions

The effect on the morphology of carbon produced from thermal stressing of JP-8 over Inconel 718 after adding a binary hydrogen donor, comprised of tetralin and α -tetralone, has been examined. Hydrogen donor addition can significantly improve the detrimental pyrolytic reactions leading to the formation of polyaromatics and other reactive species, which results in the formation of bulk and amorphous deposits on the surface. However, the reductions of such compounds being formed will allow the enhanced formation of filamentous carbon. The enhanced production of filamentous carbon is caused by the metal particles on the tips of the filaments remaining active, since they are not being encapsulated by pyrolytic carbon. To effectively reduce the formation of carbon during the pyrolytic decomposition of paraffinic-based fuels, a dual approach to the problem is needed. The first step is to passivate the surface so that the metals, such as nickel that can lead to filamentous carbon, do not interact with the fuel. Secondly, to eliminate the formation of amorphous carbon from bulk reactions, hydrogen donors can be added to the fuel to reduce the formation of polyaromatics, which are the precursors to the formation of amorphous carbon.

Acknowledgement. We are grateful for the U.S. Air Force Office of Scientific Research for financial support. Thanks go to Prof. Harold H. Schobert and Dr. Orhan Altin of Penn State University, and to Mr. William Harrison III, Dr. Cindy Obringer and Dr. Tim Edwards of the U.S. Air Force Wright Laboratory for helpful discussions.

References

- (1) Edwards, T. and Zabarnick, S. *Ind. Eng. Chem. Res.* **1993**, 32, 3117.
- (2) Song, C.; Eser, S.; Schobert, H.H.; Hatcher, P.G. *Energy & Fuels* **1993**, 7, 234.
- (3) Andresen, J.M.; Strohm, J.J.; Sun, L.; Song, C. *Energy & Fuels* **2001**, 15(3), 714.
- (4) Song, C.; Lai, W.-C.; Schobert, H.H. *Ind. Eng. Chem. Res.* **1994**, 33, 548.
- (5) Strohm, J.J.; Andresen, J.M.; Song, C. Prepr. Pap. – *Am. Chem. Soc., Div. Petro. Chem.* **2000**, 45(3), 449.
- (6) Strohm, J.J.; Andresen, J.M.; Song, C. Prepr. Pap. – *Am. Chem. Soc., Div. Fuel Chem.*, **2001**, 46(2), 487.
- (7) Strohm, J.J.; Andresen, J.M.; and Song C. Prepr. Pap. – *Am. Chem. Soc., Div. Fuel Chem.*, **2002**, 47 (3), 189.
- (8) Atria, J.; Li, J.; Eser, S.; Schobert, H.H.; and Cermignani, W. *Carbon '97, 23rd Biennial Conf. Carbon* **1997**, 2, 312.
- (9) Altin, O.; Eser, S. *Ind. Eng. Chem. Res.* **2001**, 40, 589.
- (10) Sims, C.T.; Stoloff, N.S.; and Hagel, W.C. *Superalloys*, John Wiley and Sons: New York, 1987.
- (11) Baker, R.T.K. *Carbon* **1989**, 27 (3), 315.

- (12) Strohm, J.J. *Novel Hydrogen Donors for the Improved Thermal Stability of Advanced Aviation Jet Fuels*, M.S. Thesis, The Pennsylvania State University, **2002**.
- (13) Rostrup-Nielsen, J.R. In *Catalysis Science and Technology*; Andersen, J.R.; Boudart, M., Ed.; Springer-Verlag, New York, **1984**, 4, 34.

CHARACTERIZATION AND COMPARISON OF CARBON DEPOSITION FROM THERMAL STRESSING OF JP-8 MILITARY JET FUEL AND JET-A COMMERCIAL AVIATION JET FUEL OVER PURE METAL, BINARY ALLOY AND SUPER ALLOY SURFACES

Ramya Venkataraman, Orhan Altin, and Semih Eser

The Energy Institute
&
Department of Energy and Geo-Environmental Engineering
230 Hosler Building
The Pennsylvania State University, University Park, PA
16802, USA

Introduction

Jet fuel produces significant amounts of carbon deposits over the metal surfaces of aircraft engines due to the high temperatures encountered from thermal loads during its application as coolant^{1,2}. This phenomena is a very important issue in the design of advanced aircrafts and is further complicated by the metal surface effects and composition of various types of jet fuel particularly the sulfur content³. Pure metals such as Ni and Fe have been observed to catalyze the deposit formation to a greater extent than super alloys⁴ however the nature of the sulfur compounds present in the fuel in some cases promotes and in other cases inhibits the deposit formation³. Metal catalyzed carbon deposits are more structurally ordered than thermally formed carbon. The former can also promote formation of the latter due to increased surface area⁵.

The objective of this study is to compare the nature and amount of carbon deposits from the thermal stressing of two different types of petroleum derived jet fuels, JP-8 and Jet A over a range of contemporary metal and alloy surfaces in order to understand the change in the nature of the deposition with change in fuel and catalytic surface effects.

Experimental

Thermal stressing experiments were carried out at 480 °C and 500 psig in an isothermal, glass lined flow reactor of OD 1/4". The above reaction conditions are supercritical⁶. The substrates used were two pure metals Ni and Fe, one binary alloy Fe-Ni (55/45) and a super alloy Inconel 600. The composition of Inconel 600 alloy wt% is Ni:72%, Fe:8%, Cr:15.5%, Mn: 1.0%, Cu:5000 ppm, C:1500 ppm, Si:5000 ppm, S:150 ppm. The fuels used were JP-8 which is an advanced military application fuel and Jet A which is commercial aviation jet fuel. According to the U.S turbine fuel specifications Jet A typically has a lower sulfur content than JP-8 however the in the batch received at Penn State both fuels had a comparable high sulfur content. The fuels were analyzed using GC/MS before and after the stressing experiments to study their composition. The sulfur content was obtained using GC/PFPD. The substrate foils were all cut into 13 cm X 3 mm coupons and rinsed in ethanol before being placed in the reactor. The duration of each of the experiments was 5 hours. The morphology of the carbon deposited samples was then studied under an SEM and the characterization and quantification of the deposits was done using Temperature Programmed Oxidation (TPO) in the LECO Multiphase Carbon Analyzer⁷.

Results and Discussion

The total amounts of carbon deposition over each of the samples is shown in Table 1. Characterization of these deposits using TPO reveals that all four substrates, Ni, Fe, Ni-Fe, and Inconel 600 facilitate the formation of more than one type of carbon deposit through various complex mechanisms.

Table 1. Carbon deposits in ($\mu\text{g}/\text{cm}^2$) collected over Ni, Fe, Fe-Ni and Inconel 600 surfaces from JP-8 & Jet A.

Fuel	Carbon Deposits ($\mu\text{g}/\text{cm}^2$)			
	Ni	Fe	Fe-Ni (55/45)	Inconel 600
JP-8	66	124	29	176
Jet A	12.5	15	11	111

As can be seen in Table 1 overall JP-8 forms more carbon deposition than Jet A over pure metals, binary alloy and super alloy surfaces however both low temperature and high temperature carbon peaks seem to be occurring at nearly the same temperature for a particular substrate in both fuels. The pure metals Ni and Fe individually form more carbon deposits than their combined binary (Fe-Ni 55/45) alloy. Inconel 600 showed a significantly different behavior compared to the pure metals and binary alloy. It had the highest peak for highly ordered carbon in both cases and formed the maximum amount of carbon deposition in both fuels, followed by Fe and then Ni.

The crystalline structures seen in the SEM micrograph of Fe for both JP-8 and Jet A are most likely Fe sulfide crystals with highly ordered carbon growing over its surface which in turn gives rise to small amorphous carbon structures over it. The Fe-Ni binary alloy produced a lot of filamentous carbon as well as amorphous carbon on its surface for both JP-8 and Jet A, as did the Ni surface with JP-8. The morphology of the carbon structures over Ni surface for Jet A seem mainly amorphous growing over the Ni sulfide crystals³. The Inconel 600 substrate mainly produced small spherical amorphous carbon when stressed with JP-8 and formed highly ordered filamentous carbon as well as amorphous carbon deposits with Jet A.

The carbon peak observed before 200 °C over Ni, Fe and Fe-Ni with JP-8 and over Inconel 600 with Jet A are mostly due to the adsorbed hydrocarbons on the surface of the amorphous carbon deposits. These usually have a lot of hydrogen associated with them and hence get oxidized much easier than the deposits themselves. Ni and Fe are very good substrates for the formation of catalytic carbon⁵. These may further develop secondary amorphous carbon in association with them by providing a greater surface area. Therefore we find a varied nature of carbon deposits over these substrates with both JP-8 and Jet A. The burn off temperatures for low temperature carbon increases in the order Fe-Ni, Fe, Inconel 600, Ni for JP-8 and Fe-Ni, Ni, Fe, Inconel 600 for Jet A. The high temperature carbon oxidation temperatures in increasing order are Ni, Ni-Fe, Inconel 600, Fe for JP-8 and Fe, Ni, Fe-Ni and Inconel 600 for Jet A. Although Ni is a better dehydrogenation catalyst⁸ Fe is a very good oxidation catalyst⁹, aiding in the better removal of carbon deposits, hence the CO₂ signal recorded by the carbon analyzer may be greater than that recorded over the Ni substrate. However the combination of these pure metals in the binary alloy (Fe-Ni) in a ratio of 55/45 seems to decrease the carbon deposits over the surface. According to the study by Zhang F⁴ the presence of a homogenous one phase alloy (γFe , Ni) particularly at a 55/45 ratio of Fe/Ni in the binary alloy produces substantially lower amounts of deposits. The behavior of Inconel 600 is very interesting in the case of both fuels particularly Jet A. The

presence of trace elements on the Inconel 600 surface are expected to make it less susceptible to roughening by sulfur compounds¹⁰ and carbon deposition. However, the sulfur compounds present in this batch of JP-8 and Jet A probably inhibit the formation of carbon deposits³. Ni, Fe and their binary alloy can easily form metal sulfides from the sulfur compounds in jet fuel whereas the resistance of Inconel 600 to this particular type of sulfur attack probably makes it more conducive to carbon deposit formation on its surface. The SEM micrograph of Ni surface after thermal stressing of Jet A suggests that the smooth crystalline structures in them may be Ni sulfides specific to benzylphenylsulfide which seem to inhibit carbon deposits on pure metals but increase deposition over super alloy surfaces⁷. The additives in JP-8 added for enhanced performance in military applications probably cause extensive degradation of the fuel during thermal stressing producing more solid deposits overall on different surfaces compared to Jet A.

Conclusions

The nature of carbon deposits on metal/alloy surfaces depends extensively on the nature of the substrate and can vary greatly with substrate composition but is relatively similar for similar fuels. Although pure metals are most susceptible to destruction by carbon deposition this may not be the case always. The combination of Ni and Fe in a particular ratio can decrease the carbon deposition compared to the individual metals themselves. Although the trace elements in superalloys are added to make them more resistant to attack by carbon deposits the composition of the fuel particularly the sulfur compounds can aid the formation of the same.

Acknowledgment. This work is part of a project funded by the Air Force Office of Scientific Research under contract F49620-99-1-0290.

References

1. Orhan Altin, Geoffrey Bock and Semih Eser, "Thermal Stressing of Petroleum and Coal-Derived Jet Fuels On Inconel 718" *Division of Petroleum Chemistry, Inc., ACS 221st National Meeting*, Boston, August, 2001.
2. Strohm J. J.; Butnark S.; Keyser T.L.; Andersen J. M.; Badger M. W.; Schobert, H. H.; Song C. *Fuel Chemistry Division preprints* 2002, 47, 177-178.
3. Encarnacion Raymundo-Pinero, Orhan Altin, and Semih Eser, "Effects of Sulfur Compounds on Solid Deposition on Metals and Inconel 718 from Thermal Decomposition of N-Dodecane" *Division of Petroleum Chemistry, ACS 221st National Meeting*, Boston, August, 2001.
4. Zhang, F., *Carbon Deposition on Heated Alloy Surfaces From Thermal Decomposition of Jet Fuel*, M.S. Thesis, 2000, Pennsylvania State University, University Park.
5. Li, J., *Metal Surface Effects on Deposit Formation from Thermally Stressed Jet Fuel and Model Compounds*, Ph.D. Thesis, 1998, Pennsylvania State University, University Park.
6. Edwards T.; Zabarnick S.; *Ind. Eng. Chem. Res.* 1993, 32, 3117-3122.
7. Altin, O.; Eser, S.; *Ind. Eng. Chem. Res.*, 1999, 39(3), 642.
8. Yu J.; Eser S.; *Ind. Eng. Chem. Res.* 1997, 36, 534-584.
9. Thrower, P.A. *Chemistry and Physics of Carbon*. Marcel Dekker, INC, 1981, Vol 16.
10. Zhang F.; Altin O.; Eser S.; *Prepr. Pap- ACS Fuel Division Preprints* 2000, 220.

Carbon deposits from the thermal stressing of JP-8 over Ni, Fe, Fe-Ni (55/45) and Inconel 600 surfaces at supercritical conditions.

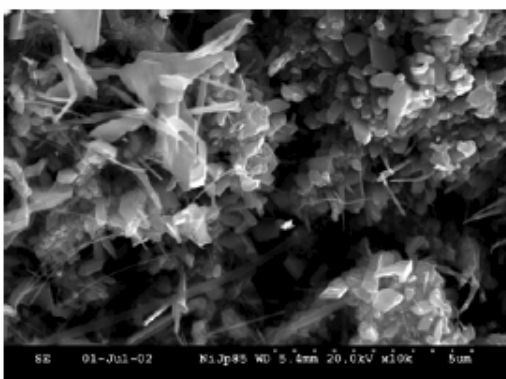


(Fig.1) SEM micrograph of JP-8 stressed over Ni for 5 hrs.

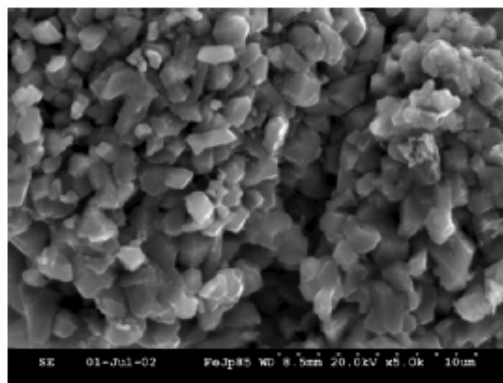


(Fig.2) SEM micrograph of JP-8 stressed over Fe for 5 hrs.

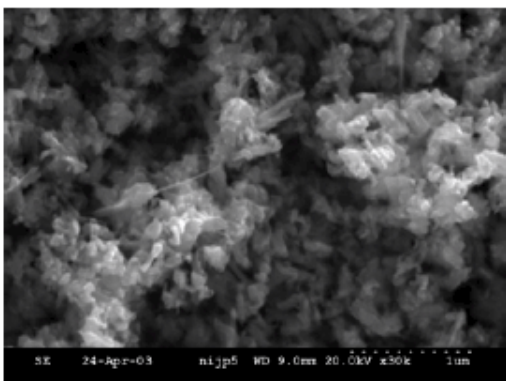


(Fig.3) SEM micrograph of JP-8 stressed over Fe-Ni (55/45) for 5 hrs.

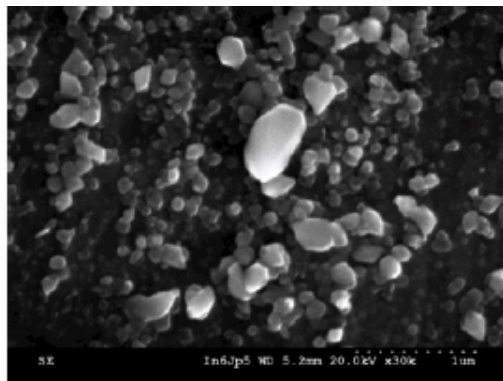


(Fig.4) SEM micrograph of JP-8 stressed over Inconel 600 for 5 hrs.

Carbon deposits from the thermal stressing of Jet A over Ni, Fe, Fe-Ni (55/45) and Inconel 600 surfaces at supercritical conditions.

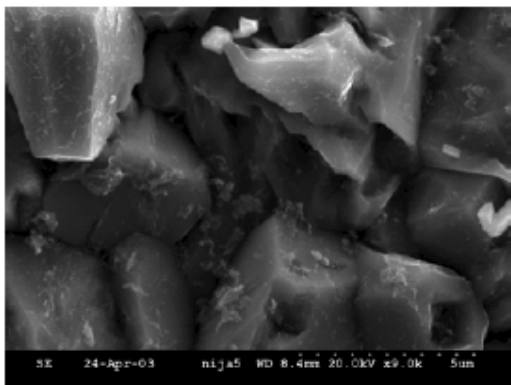


(Fig.5) SEM micrograph of Jet A stressed over Ni for 5 hrs.

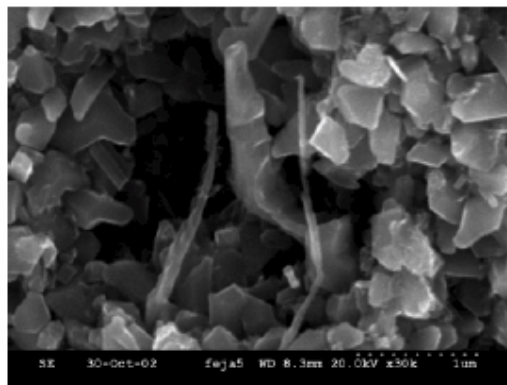


(Fig.6) SEM micrograph of Jet A stressed over Fe for 5 hrs.

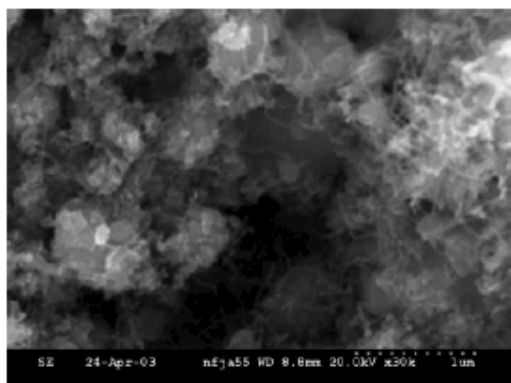


(Fig.7) SEM micrograph of Jet A stressed over Fe-Ni (55/45) for 5 hrs

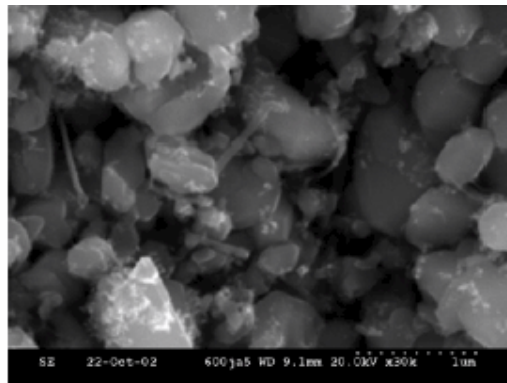


(Fig.8) SEM micrograph of Jet A stressed over Inconel 600 for 5 hrs.

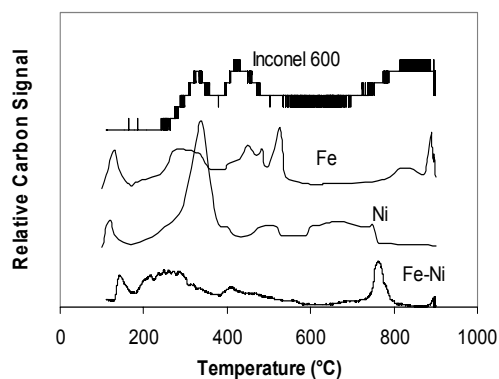


Figure 9. TPO profile of the deposits collected on JP-8 over Ni, Fe, Fe-Ni and Inconel 600 at 480°C, 500 psig and 4 ml/min flow rate for 5 hours.

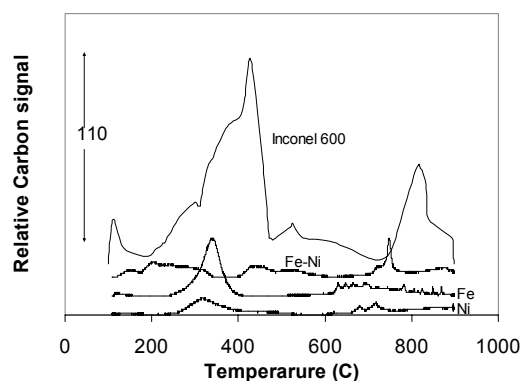


Figure 10. TPO profile of the deposits collected on Jet A over Ni, Fe, Fe-Ni and Inconel 600 at 480°C, 500 psig and 4 ml/min flow rate for 5 hours.

ENERGETIC CATALYST-HYDROGEN PLASMA REACTION AS A POTENTIAL NEW ENERGY SOURCE

R. L. Mills, P. Ray, M. Nansteel, J. He, X. Chen, A. Voigt,
and B. Dhandapani

BlackLight Power, Inc.
493 Old Trenton Road
Cranbury, NJ 08512

Introduction

A new chemically generated or assisted plasma source based on a resonant energy transfer mechanism (rt-plasma) has been developed that may be a new power source. One such source operates by incandescently heating a hydrogen dissociator and a catalyst to provide atomic hydrogen and gaseous catalyst, respectively, such that the catalyst reacts with the atomic hydrogen to produce a plasma. It was extraordinary that intense extreme ultraviolet (EUV) emission was observed by Mills et al.^{1,2} at low temperatures (e.g. $\approx 10^3$ K) and an extraordinary low field strength of about 1–2 V/cm from atomic hydrogen and certain atomized elements or certain gaseous ions which singly or multiply ionize at integer multiples of the potential energy of atomic hydrogen, 27.2 eV. A number of independent experimental observations confirm that the rt-plasma is due to a novel reaction of atomic hydrogen which produces as chemical intermediates, hydrogen in fractional quantum states that are at lower energies than the traditional “ground” ($n = 1$) state. Power is released, and the final reaction products are novel hydride compounds or lower-energy molecular hydrogen as reported herein. The supporting data include EUV spectroscopy,^{1–6,8–10} characteristic emission from catalysts and the hydride ion products,^{2,6,9} lower-energy hydrogen emission,^{3–5} chemically formed plasmas,^{1,2,6,8,9} extraordinary (>100 eV) Balmer α line broadening,^{1–3,6,7,9} population inversion of H lines,^{9,10} elevated electron temperature,⁷ anomalous plasma afterglow duration,⁸ power generation,^{3,4} and analysis of novel chemical compounds.¹¹

The theory given previously^{1,3–6,12} is based on applying Maxwell’s equations to the Schrödinger equation. The familiar Rydberg equation (Eq. (1)) arises for the hydrogen excited states for $n > 1$ of Eq. (2).

$$E_n = -\frac{e^2}{n^2 8\pi\epsilon_0 a_H} = -\frac{13.598 \text{ eV}}{n^2} \quad (1)$$

$$n = 1, 2, 3, \dots \quad (2)$$

An additional result is that atomic hydrogen may undergo a catalytic reaction with certain atoms, excimers, and ions which provide a reaction with a net enthalpy of an integer multiple of the potential energy of atomic hydrogen, $m \cdot 27.2$ eV wherein m is an integer. The reaction involves a nonradiative energy transfer to form a hydrogen atom that is lower in energy than unreacted atomic hydrogen that corresponds to a fractional principal quantum number. That is

$$n = \frac{1}{2}, \frac{1}{3}, \frac{1}{4}, \dots, \frac{1}{p}; \quad p \text{ is an integer} \quad (3)$$

replaces the well known parameter $n = \text{integer}$ in the Rydberg equation for hydrogen excited states. The $n = 1$ state of hydrogen and the $n = \frac{1}{\text{integer}}$ states of hydrogen are nonradiative, but a

transition between two nonradiative states, say $n = 1$ to $n = 1/2$, is possible via a nonradiative energy transfer. Thus, a catalyst provides a net positive enthalpy of reaction of $m \cdot 27.2$ eV (i.e. it resonantly

accepts the nonradiative energy transfer from hydrogen atoms and releases the energy to the surroundings to affect electronic transitions to fractional quantum energy levels). As a consequence of the nonradiative energy transfer, the hydrogen atom becomes unstable and emits further energy until it achieves a lower-energy nonradiative state having a principal energy level given by Eqs. (1) and (3). Processes such as hydrogen molecular bond formation that occur without photons and that require collisions are common. Also, some commercial phosphors are based on resonant nonradiative energy transfer involving multipole coupling.

Two $H(1/p)$ atoms may react to form the corresponding molecule $H_2(1/p)$ that has a bond energy and vibrational levels that are p^2 times those of H_2 comprising uncatalyzed atomic hydrogen where p is an integer. The theory was given previously.^{4,5,12} Since the $v = 0$ to $v = 1$ vibrational transition of H_2 is a resonant state of the corresponding transition of $H_2(1/2)$, emission due to the reaction $2H(1/2) \rightarrow H_2(1/2)$ is possible with vibronic coupling within the transition state at

$$E_{D+vib} = p^2 E_{D H_2} \pm \left(\frac{v^*}{3}\right) E_{vib H_2(v=0 \rightarrow v=1)}, \quad v^* = 1, 2, 3, \dots \quad (4)$$

where $E_{D H_2}$ and $E_{vib H_2(v=0 \rightarrow v=1)}$ are the experimental bond and vibrational energies of H_2 , respectively.

Atomic and molecular hydrogen are predicted to form stable states of lower energy than traditionally thought possible. Substantial spectroscopic and physical differences are anticipated. For example, novel EUV atomic and molecular spectral emission lines from transitions corresponding to energy levels given by Eqs. (1) and (3) and Eq. (4), respectively, are predicted. He^+ fulfills the catalyst criterion—a chemical or physical process with an enthalpy change equal to an integer multiple of 27.2 eV since it ionizes at 54.417 eV which is $2 \cdot 27.2$ eV. Thus, microwave discharges of helium–hydrogen mixtures were studied by EUV spectroscopy to search for line emission from transitions to fractional Rydberg states of atomic hydrogen and due to the formation of molecular hydrogen corresponding to fractional Rydberg states of atomic hydrogen. In addition, helium–hydrogen (90/10%) and helium–deuterium (90/10%) plasma gases were flowed through a high-vacuum (10^{-6} Torr) capable, liquid nitrogen cryotrap, and the condensed gas was characterized by gas chromatography (GC), mass spectroscopy (MS), visible and EUV optical emission spectroscopy (OES), and 1H nuclear magnetic resonance (NMR) of the liquid-nitrogen-condensable gas dissolved in $CDCl_3$. Since the electronic transitions are very energetic, power balances were measured to determine whether this reaction has sufficient kinetics to merit its consideration as a practical power source.

Experimental

EUV spectroscopy was recorded on microwave discharge plasmas of hydrogen, nitrogen, oxygen, carbon dioxide, ammonia, helium, neon, argon, krypton, xenon, or 2% hydrogen mixed plasmas as well as nitrogen-methane (96/4%) according to the methods given previously.^{3,4} Each ultrapure gas alone or mixture was flowed through a half inch diameter quartz tube at an inlet pressure of 1 Torr. The gas pressure to the cell was maintained during differential pumping by flowing the mixture while monitoring the pressure with a 10 Torr and 1000 Torr MKS Baratron absolute pressure gauge. The tube was fitted with an Opthos coaxial microwave cavity (Evenson cavity). The microwave generator was an Opthos model MPG-4M generator (Frequency: 2450 MHz). The input power to the plasma was set at 85 watts with forced air cooling of the cell. Extreme ultraviolet emission spectra were also obtained on these plasmas maintained in a glow discharge cell that comprised a five-

way stainless steel cross that served as the anode with a hollow stainless steel cathode according to the methods given previously.^{5,7} For spectral measurement, the light emission was introduced to a normal incidence McPherson 0.2 meter monochromator (Model 302) equipped with a 1200 lines/mm holographic grating with a platinum coating. The wavelength region covered by the monochromator was 2–560 nm. The EUV spectrum was recorded with a channel electron multiplier (CEM) at 2500–3000 V or a photomultiplier tube (PMT) at -1000 V and a sodium salicylate scintillator. The wavelength resolution was about 0.2 nm (FWHM) with an entrance and exit slit width of 50 μm . The increment was 0.2 nm and the dwell time was 500 ms. The PMT (Model R1527P, Hamamatsu) used has a spectral response in the range of 185–680 nm with a peak efficiency at about 400 nm. The increment was 0.4 nm and the dwell time was 1 s. Peak assignments were based on a calibration against the known He I, He II, and Lyman series lines.

To achieve higher sensitivity at the shorter EUV wavelengths, the light emission was recorded with a McPherson 4° grazing incidence EUV spectrometer (Model 248/310G) equipped with a grating having 600 lines/mm with a radius of curvature of $\approx 1\text{m}$. The angle of incidence was 87°. The wavelength region covered by the monochromator was 5–65 nm. The wavelength resolution was about 0.1 nm (FWHM) with an entrance and exit slit width of 300 μm . The increment was 0.1 nm and the dwell time was 500 ms. The light was detected by a CEM at 2400 V.

Condensable gas from helium–hydrogen (90/10%) microwave plasmas maintained in the Evenson cavity was collected in a high-vacuum (10^{-6} Torr) capable, liquid nitrogen cryotrap as described previously.¹³ After each plasma run the cryotrap was pumped down to 10^{-5} Torr to remove any non-condensable gases in the system. The pressure was recorded as a function of time as the cryotrap was warmed to room temperature. Typically, about 3 Torr of condensed gas was collected in a 3 hr plasma run. Controls were hydrogen and helium alone.

The mass spectra ($m/e=1$ to $m/e=200$) of ultrahigh purity hydrogen (Praxair) control samples and samples of the condensable gas from the helium–hydrogen microwave plasmas were recorded with a residual gas analyzer. In addition, the ion current as a function of time of the mass to charge ratio of two ($m/e=2$) was recorded while changing the electron gun energy from 30 to 70 to 100 eV for ultrapure hydrogen and the condensable gas from the helium–hydrogen plasma reaction.

Cryogenic gas chromatography was performed on a Hewlett Packard 5890 Series II gas chromatograph equipped with a thermal conductivity detector and a 60 meter, 0.32 mm ID fused silica Rt-Alumina PLOT column (Restek, Bellefonte, PA). The chromatographic column was submerged in liquid nitrogen, and samples were run at -196° C using Ne as the carrier gas.

OES was performed on the condensable gas from helium–hydrogen (90/10%) microwave plasmas to search for atomic hydrogen lines from plasma-decomposed $\text{H}_2(1/p)$. A sample tube was fitted with the Evenson cavity, and the visible spectrum was recorded during a discharge maintained at 80 W input power at about 2 Torr as described previously.¹³

EUV OES was performed on the condensable gas from helium–hydrogen (90/10%) and helium–deuterium (90/10%) microwave plasmas by flowing the gas through a needle valve from a gas collection tube to the half inch diameter quartz tube fitted with the Evenson cavity. The microwave system and EUV spectrometer was as given *supra.*, except that the differential pumping was enhanced using a 2 mm diameter pin-hole optic between the plasma tube and chamber, and only the turbo pump was used. With the typical

pressure in the 20 cm^3 gas collection tube of 5–20 Torr, the plasma could be maintained for up to 30 minutes before the flowing gas was depleted. Peak assignments were based on a calibration against standard lines obtained before and after each run as given previously.¹³

Sealed ^1H NMR samples were prepared by collecting the condensed gas from the cryotrap in an NMR tube (5 mm OD, 23 cm length, Wilmad) which was then sealed as described previously.¹³ Control NMR samples comprised ultrahigh purity hydrogen (Praxair) and the helium–hydrogen (90/10%) mixture with CDCl_3 solvent. The NMR spectra were recorded with a 300 MHz Bruker NMR spectrometer that was deuterium locked. The chemical shifts were referenced to the frequency of tetramethylsilane (TMS) at 0.00 ppm.

The excess power was measured by water bath calorimetry on helium–hydrogen (90/10%) plasmas maintained in a microwave discharge cell compared to control plasmas with the same input power. The water bath was calibrated by a high precision heater and power supply. A high precision linear response thermistor probe (Omega OL-703) recorded the temperature of the 45 L water bath as a function of time for the stirrer alone to establish the baseline. The heat capacity was determined for several input powers, 30, 40, and 50 $\text{W} \pm 0.01\text{ W}$, and was found to be independent of input power over this power range within $\pm 0.05\%$. The temperature rise of the reservoir as a function of time gave a slope in $^\circ\text{C/s}$. This slope was baseline corrected for the negligible stirrer power and loss to ambient. The constant known input power (J/s), was divided by this slope to give the heat capacity in $\text{J}/^\circ\text{C}$. Then, in general, the total power output from the cell to the reservoir was determined by multiplying the heat capacity by the rate of temperature rise ($^\circ\text{C/s}$) to give J/s.

Since the cell and water bath system were adiabatic, the general form of the power balance equation with the possibility of excess power is:

$$P_{in} + P_{ex} - P_{out} = 0 \quad (5)$$

where P_{in} is the microwave input power, P_{ex} is the excess power generated from the hydrogen catalysis reaction, and P_{out} is the thermal power loss from the cell to the water bath. Since the cell was surrounded by water that was contained in an insulated reservoir with negligible thermal losses, the temperature response of the thermistor T as a function of time t was determined to be

$$\dot{T}(t) = (1.907 \times 10^5 \text{ J}/^\circ\text{C})^{-1} \times P_{out} \quad (6)$$

where $1.907 \times 10^5 \text{ J}/^\circ\text{C}$ is the heat capacity for the least square curve fit of the response to power input for the control experiments ($P_{ex} = 0$). The slope was recorded for about 2 hours after the cell had reached a thermal steady state, to achieve an accuracy of $\pm 1\%$.

Results and Discussion

The EUV emission was recorded from microwave and glow discharge plasmas of (1) hydrogen, helium, krypton, and xenon alone, and (2) krypton and xenon with 2% hydrogen over the wavelength range 5–125 nm. No peaks were observed in these controls except hydrogen peaks at wavelengths greater than about 80 nm for hydrogen alone or hydrogen mixed with krypton or xenon. Neither krypton or xenon satisfy the catalyst condition; thus, no novel lines were predicted. Similarly, only He I and He II peaks were observed for helium alone.

The EUV spectrum (5–100 nm) of the microwave cell emission of the helium–hydrogen (98/2%) mixture is shown in Figure 1.

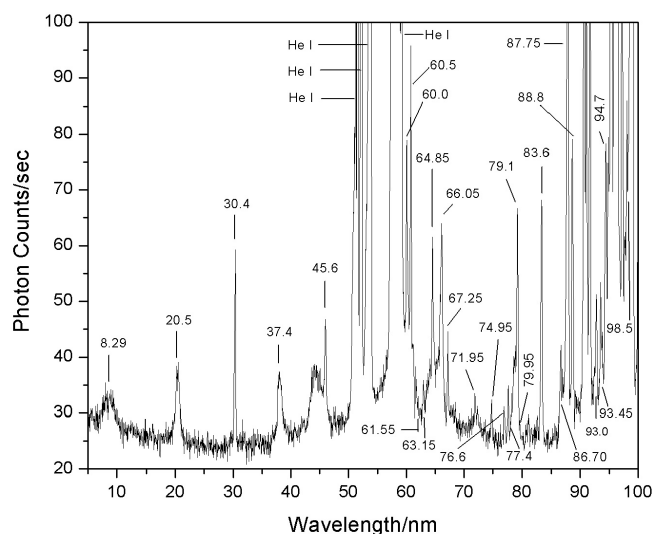


Figure 1. The EUV spectrum (5–100 nm) of the microwave cell emission of the helium–hydrogen (98/2%) mixture recorded with a normal incidence EUV spectrometer and a CEM. Reproducible novel emission lines were observed at 45.6 nm, 30.4 nm, and 8.29 nm with energies of $q \cdot 13.6$ eV where $q = 2, 3$, or 11 and at 37.4 nm and 20.5 nm with energies of $q \cdot 13.6$ eV where $q = 4$ or 6 that were inelastically scattered by helium atoms wherein 21.2 eV was absorbed in the excitation of He ($1s^2$) to He ($1s^1 2p^1$). In addition, a novel series of sharp wavelength-labeled peaks were observed in the 60–100 nm region that were assigned to members of peaks predicted at $E_{D+vib} = 17.913 \pm (v^*/3) 0.515902$ eV due to the reaction $2H(1/2) \rightarrow H_2(1/2)$ with vibronic coupling.

Reproducible novel emission lines were observed at 45.6 nm, 30.4 nm, and 8.29 nm with energies of $q \cdot 13.6$ eV where $q = 2, 3$, or 11 and at 37.4 nm, and 20.5 nm with energies of $q \cdot 13.6$ eV where $q = 4$ or 6 that were inelastically scattered by helium atoms wherein 21.2 eV was absorbed in the excitation of He ($1s^2$) to He ($1s^1 2p^1$) as discussed previously.^{3,4,13} Additional spectra extended the series to $q = 1, 2, 3, 4, 6, 7, 8, 9$, or 11 as discussed before.^{3,4,13} In addition, a series of peaks were observed in the 60–100 nm region of Figure 1. The wavelength-labeled peaks in Figure 1 match members of peaks predicted at $E_{D+vib} = 17.913 \pm \left(\frac{v^*}{3}\right) 0.515902$ eV, $v^* = 1, 2, 3, \dots$ due

to the reaction $2H(1/2) \rightarrow H_2(1/2)$ with vibronic coupling. Hydrogen has no peaks below 80 nm. The peaks of the series also do not match helium as shown in control spectra and NIST tables¹⁴ except for a distinguishable peak at 97.2 nm.⁴ Figure 2 shows the plot of the theoretical emission vacuum wavelengths E_{DH_2} due to the reaction $2H(1/2) \rightarrow H_2(1/2)$ with vibronic coupling at energies of $E_{D+vib} = p^2 E_{DH_2} \pm \left(\frac{v^*}{3}\right) E_{vib H_2} (v=0 \rightarrow v=1)$ ($p=2$) and the wavelengths observed over multiple spectra as partially shown in Figure 1. The data matched (Eq. (4)) to longer wavelengths for $v^* = 2$ to $v^* = 32$ and to shorter wavelengths for $v^* = 1$ to $v^* = 16$ to within the spectrometer resolution of about $\pm 0.05\%$.

Helium–hydrogen (90/10%) gas was flowed through the microwave tube and the cryosystem for 2 hours with the trap cooled to liquid nitrogen temperature. No change in pressure over time was observed when the dewar was removed, and the system was warmed to room temperature. The experiment was repeated under the same

conditions but with a plasma maintained with 60 W forward microwave power and 10 W reflected. In contrast to the control case, a liquid-nitrogen-condensable gas was generated in the helium–hydrogen plasma reaction since the pressure due to the reaction product rose from 10^{-5} Torr to 3 Torr as the cryotrap warmed to room temperature.

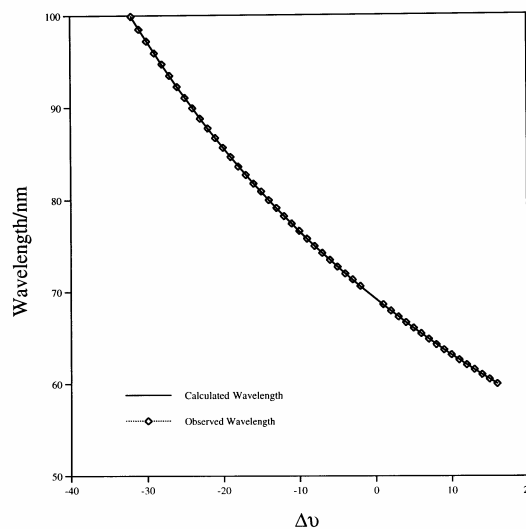


Figure 2. The plot of the theoretical (Eq. (4)) emission vacuum wavelengths E_{DH_2} due to the reaction $2H(1/2) \rightarrow H_2(1/2)$ with vibronic coupling at energies of $E_{D+vib} = p^2 E_{DH_2} \pm (v^*/3) E_{vib H_2} (v=0 \rightarrow v=1)$ ($p=2$) and the wavelengths observed such as those shown in Figure 1. The data matched to longer wavelengths for $v^* = 2$ to $v^* = 32$ and to shorter wavelengths for $v^* = 1$ to $v^* = 16$ to within the spectrometer resolution of about $\pm 0.05\%$.

The mass spectrum over the range $m/e = 1$ to $m/e = 200$ showed that the condensable gas was highly pure hydrogen. The $m/e = 2$ ion current as a function of time was recorded while changing the electron gun energy from 30 to 70 to 100 eV for ultrapure hydrogen and the condensed gas from the helium–hydrogen plasma reaction. The relative changes in the $m/e = 2$ ion current with increasing electron-beam energy indicated that the condensable gas has a higher ionization potential than ultrapure hydrogen. Upon increasing the ionization potential from 30 eV to 70 eV, the $m/e = 2$ ion current for the control hydrogen increased by a factor of about 30%; whereas, the gas collected under liquid nitrogen from the helium–hydrogen plasma increased by a factor of about 10 under the same pressure condition as that of the control.

The only known gases that show peaks on the liquid nitrogen-cooled Rt-Alumina PLOT column are helium and para-hydrogen and ortho-hydrogen, and these gases can be identified by their retention times of 13.7 min., 17.1 min., and 18.9 min., respectively. Trace helium (0.4%) and small peaks at the position of hydrogen were observed for the condensed gas that had the same 1:3 para-ortho ratio as H_2 . However, two additional larger peaks were observed at 18.9 min. and 28.9 min. that had the same 1:3 relative ratio and were less thermally conductive than the neon carrier gas. The negative peaks could result from an on-column pressure change associated with the analyte gas.

With sufficient input power, the electrons at the tail of the Maxwellian distribution of a microwave plasma may be sufficiently energetic to ionize and decompose $H_2(1/2)$ (65 eV). The high resolution (± 0.1 nm) visible optical emission spectrum recorded on a

microwave discharge plasma of the liquid-nitrogen-condensable helium–hydrogen (90/10%) microwave discharge plasma gas showed strong Balmer α , β , γ , and δ lines of atomic hydrogen at 656.28 nm, 486.13 nm, 434.05 nm, and 410.17 nm, respectively, which indicated that the gas contained hydrogen.

The EUV optical emission spectra (45–100 nm) recorded on two separate microwave discharge plasmas of the liquid-nitrogen-condensable helium–hydrogen (90/10%) microwave discharge plasma gases collected over 48 hours are shown in Figure 3. A reproducible series of evenly spaced peaks were observed with a higher energy separation of 0.74 eV compared to the vibrational energy of H_2 ($E_{vib} H_2 (v=0 \rightarrow v=1) = 0.5159 \text{ eV}$) which is the highest known vibration transition energy. The series was similar to that shown in Figure 1, except that the energy spacing is about four times larger. Hydrogen has no emission below 80 nm. The peaks from the condensable gas did not match those of hydrogen for wavelengths >80 nm as well. The series of evenly spaced peaks did not match the He I and He II peaks observed from the helium gas discharge. The series of lines shown in Figure 3 was assigned to mixed vibration-rotational transitions of an electronically excited state of $H_2(1/p)$.

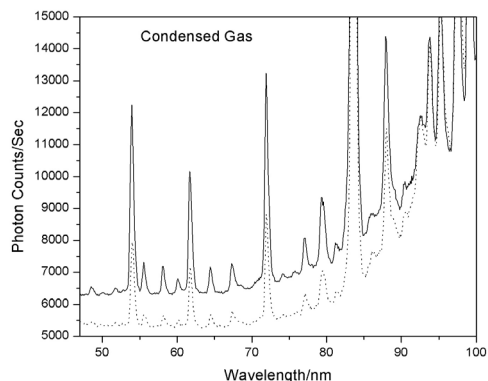


Figure 3. The EUV optical emission spectra (45–100 nm) recorded with a normal incidence EUV spectrometer and a CEM on two separate microwave discharge plasmas of the liquid-nitrogen-condensable helium–hydrogen (90/10%) microwave discharge plasma gases. A reproducible series of evenly spaced peaks were observed with a higher energy separation of 0.74 eV compared to the vibrational energy of H_2 ($E_{vib} H_2 (v=0 \rightarrow v=1) = 0.5159 \text{ eV}$) which is the highest known vibration transition energy. The series of lines was assigned to mixed vibration-rotational transitions of an electronically excited state of $H_2(1/p)$.

Deuterium substitution offers a method of definitively making the assignment of the condensed gas to a hydrogen-type molecule by the observation of a predicted shift of the spectral lines relative to the hydrogen spectrum. The EUV optical emission spectra (50–80 nm) recorded on microwave discharge plasmas of the liquid-nitrogen-condensable helium–hydrogen (90/10%) and helium–deuterium (90/10%) microwave discharge plasma gases are shown in Figure 4 (top) and (bottom), respectively. The isotope shift of the lines identified the series as belonging to $H_2(1/p)$ and supported the assignment of mixed vibration-rotational transitions of an electronically excited state of $H_2(1/p)$. The energy difference of 0.44 eV between the hydrogen and deuterium-based gases at 71.9 nm and 73.8 nm gives a good match to $p=2$ if anharmonicity and the increased electronic energy ΔE_{ele} of deuterium compared to hydrogen is considered as discussed previously.¹³

An exhaustive list of even remotely possible alternative assignments was considered for the EUV results for the reaction

plasma EUV emission shown in Figure 1 and the liquid-nitrogen condensable H_2 shown in Figures 3 and 4. The only known species in a helium–hydrogen plasma, H^+ , H_2^+ , H_3^+ , H^- , H , H_2 , He_2^+ ,

HeH^+ , and remotely possibly HeH were eliminated since the spectra did not match or the species could not exist under the reaction conditions. Other exotic possibilities such as He_2^+ , HHe_2^+ , HHe_n^+ and He_n were eliminated due to the extremely specialized conditions required for their formation such as extremely low temperatures that were unlike those in the helium–hydrogen microwave plasmas.^{15,16} Air contaminants were also eliminated. Emission from plasmas of nitrogen, oxygen, carbon dioxide, and ammonia or these gases with 2% hydrogen showed no emission in the region < 80 nm. In addition, water vapor present in the oxygen–hydrogen plasma showed no emission in this region. The spectrum of the nitrogen–methane (96/4%) plasma to form CN , C_x , and C_xH_y species (confirmed by visible spectra) showed no emission in this region. Emission of argon, krypton, and xenon as helium contaminants was eliminated. No emission was observed in the region <80 nm for krypton, krypton–hydrogen, xenon, xenon–hydrogen, and argon. Neon was eliminated based on spectral line mismatches and absences since only the Ne I lines were observed. Cl I, Br I, I I, and S I lines given by the NIST tables¹⁴ were not detected in the visible or shorter wavelength regions. Silicon from the quartz tube wall was eliminated based on the NIST tables.¹⁴ No pump contaminants were possible.

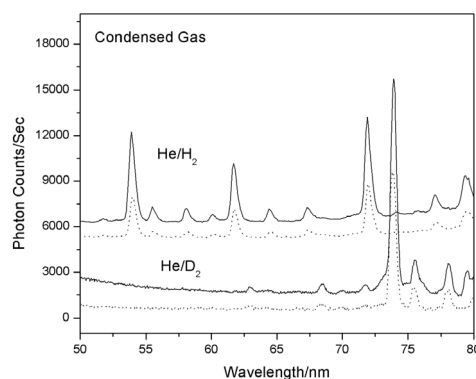


Figure 4. The EUV optical emission spectra (50–80 nm) recorded with a normal incidence EUV spectrometer and a CEM on two microwave discharge plasmas of the liquid-nitrogen-condensable helium–hydrogen (90/10%) (top) and helium–deuterium (90/10%) (bottom) microwave discharge plasma gases. The observation that the novel EUV emission spectrum shifted with deuterium substitution in a region where no hydrogen emission has ever been observed strongly supported the existence of lower-energy molecular hydrogen. The isotope shift of the lines also identified the series as belonging to mixed vibration-rotational transitions of an electronically excited state of $H_2(1/p)$.

1H NMR spectra on sealed samples of condensable helium–hydrogen plasma gases dissolved in $CDCl_3$ relative to tetramethylsilane (TMS) are shown in Figure 5. Peaks observed in the 0 to 10 ppm region were a singlet peak at 7.26 ppm with side bands which matched $CDCl_3$ and two novel singlet peaks at 3.22 and 3.47 ppm. In addition, an H_2 peak was observed at 4.63 ppm. NMR chemical shifts of common laboratory solvents as trace impurities are given by Gottlieb et al.¹⁷ All of the possible assignments were eliminated based on a mismatch between the observed and literature values for the chemical shifts, or in cases where the shifts matched to within ± 0.05 ppm, the known compound was eliminated based on a

mismatch between the multiplicity of the peak and/or the absence of other peaks of the known compound.

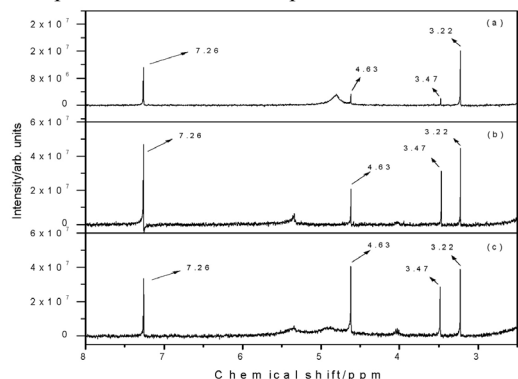


Figure 5. The ^1H NMR spectrum (2–7.5 ppm) on sealed samples of liquid-nitrogen-condensable helium–hydrogen plasma gases dissolved in CDCl_3 relative to tetramethylsilane (TMS). In each case, an H_2 peak was observed at 4.63 ppm. A singlet peak was observed at 7.26 ppm which matched CHCl_3 . Two novel singlet peaks were observed at 3.22 ppm and 3.47 ppm which could not be assigned to a known compound. These upfield peaks relative to H_2 were assigned to $\text{H}_2(1/p)$ in two p quantum states.

The upfield peaks relative to H_2 only formed during the helium–hydrogen plasma reaction. The 3.22 ppm and 3.47 ppm peaks that could not be assigned to any known compound was assigned to $\text{H}_2(1/p)$ in two different quantum states. Even though the radii of corresponding states are related by inverse integers, the anticipated shifts are relatively small and matched those anticipated as discussed previously.¹³ The assignments were further consistent with the EUV OES, GC, and MS results.

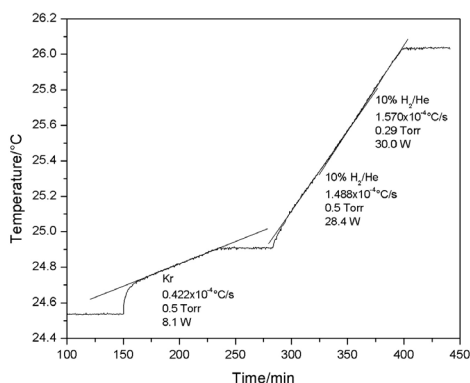


Figure 6. The $T(t)$ water bath response to stirring and then with selected panel meter readings of the constant forward and reflected microwave input power to krypton was recorded. The microwave input power was determined to be 8.1 ± 1 W. A helium–hydrogen (90/10%) mixture was run at identical microwave input power readings as the control, and the excess power was determined to be 21.9 ± 1 W from the $T(t)$ response.

The water bath calorimetry is an absolute standard and indicated $P_{in} = 8.1 \pm 1$ W input power at the selected diode settings for all control plasmas. From these results, power input to the helium–hydrogen plasma was confidently known as the diode readings identically matched those of the controls. For example, the $T(t)$ water bath response to stirring and then with selected panel meter readings of the constant forward and reflected microwave input

power to krypton was recorded as shown in Figure 6. Using the corresponding $\dot{T}(t)$ in Eq. (6), the microwave input power was determined to be 8.1 ± 1 W. A helium–hydrogen (90/10%) mixture was run at the same microwave input power readings as the control which corresponded to $P_{in} = 8.1 \pm 1$ W in Eq. (5). The $T(t)$ response was significantly increased for helium–hydrogen (90/10%) as shown in Figure 6. At 350 minutes, the pressure was changed from 0.5 Torr to 0.29 Torr. A slight increase in $\dot{T}(t)$ was observed at the lower pressure, possibly due to an increase in atomic hydrogen and He^+ . The excess power was determined to be 21.9 ± 1 W from the corresponding $\dot{T}(t)$ using Eq. (6) and Eq. (5). The sources of error were the error in the calibration curve (± 0.05 W) and the measured microwave input power (± 1 W). The propagated error of the calibration and power measurements was ± 1 W. Given an excess power of 21.9 W in 3 cm^3 and a helium–hydrogen (90/10%) flow rate of 10.0 sccm, the excess power density and energy balance were high, 7.3 W/cm^3 and $-2.9 \times 10^4 \text{ kJ/mole H}_2$ (150 eV/H atom), respectively. The reaction of hydrogen to form water which releases $-241.8 \text{ kJ/mole H}_2$ (1.48 eV/H atom) is about 100 times less than that observed. The results indicate that a new power source based on the catalysis of atomic hydrogen is not only possible, but is competitive with gas turbine combustion.

References

- (1) Mills, R.L., Nansteel, M., Ray, P., *IEEE Trans. Plasma Sci.*, **2002**, 30 (2), 639.
- (2) Mills, R.L., Nansteel, M., Ray, P., *New J. Phys.*, **2002**, 4, 70.1.
- (3) Mills, R.L., Ray, P., Dhandapani, B., Nansteel, M., Chen, X., He, J., *J. Mol. Struct.*, **2002**, 643 (1–3), 43.
- (4) Mills, R.L., Ray, P., Dong, J., Nansteel, M., Dhandapani, B., He, J., *Vib. Spectrosc.*, **2003**, 31 (2), 195.
- (5) Mills, R.L., Ray, P., *Int. J. Hydrogen Energy*, **2002**, 27 (5), 533.
- (6) Mills, R.L., Ray, P., *Int. J. Hydrogen Energy*, **2003**, 28 (8), 825.
- (7) Mills, R.L., Ray, P., Dhandapani, B., Mayo, R.M., He, J., *J. Appl. Phys.*, **2002**, 92 (12), 7008.
- (8) Conrads, H., Mills, R.L., Wrubel, Th., *Plasma Sources Sci. Technol.*, in press.
- (9) Mills, R.L., Ray, P., Mayo, R.M., *IEEE Trans. Plasma Sci.*, **2003**, 31 (2), 236.
- (10) Mills, R.L., Ray, P., Mayo, R.M., *Appl. Phys. Lett.*, **2003**, 82 (11), 1679.
- (11) Mills, R.L., Dhandapani, B., Nansteel, M., He, J., Shannon, T., Echezuria, A., *Int. J. Hydrogen Energy*, **2001**, 26 (4), 339.
- (12) Mills, *The Grand Unified Theory of Classical Quantum Mechanics*, September 2001 Edition, BlackLight Power, Inc., Cranbury, New Jersey, Distributed by Amazon.com; January (2003) Edition posted at www.blacklightpower.com.
- (13) Mills, R.L., Dhandapani, B., Nansteel, M., He, J., Ray, P., *J. Phys. Chem. B*, submitted.
- (14) NIST Atomic Spectra Database, www.physics.nist.gov/cgi-bin/AtData/display.ksh.
- (15) Baccarelli, I., Gianturco, F. A., Schneider, F., *J. Phys. Chem. A*, **1997**, 101, 6054.
- (16) Higgins, J., Callegari, C., Reho, J., Stienkemeier, F., Ernst, W.E., Gutowski, M., Scoles, G., *J. Phys. Chem. A*, **1998**, 102, 4952.
- (17) Gottlieb, H.E., Kotlyar, V., Nudelman, A., *J. Org. Chem.*, **1997**, 62, 7512.

VALORIZATION OF LIGHT ALKANES FOR THE PRODUCTION OF LPG AND QUALITY GASOLINE

N. Viswanadham^{1*}, Uday T. Turaga², and Lalji Dixit¹

¹Indian Institute of Petroleum, Dehra Dun 248005, India

²Fuel Science Program, The Pennsylvania State University, State College, PA 16802

*E-Mail: nvish@iip.res.in

Introduction

Environmental legislation is restricting the use of light petroleum fractions such as light naphtha (LN) and natural gas liquid (NGL) for gasoline blending because these feeds have high Reid Vapor Pressure (~70) and low octane numbers (65-70). Consequently, such feedstocks are not being consumed and becoming available in surplus quantities. Existing refinery processes like catalytic reforming are not effective as the feedstocks mainly contain *n*-pentane and *n*-hexane that are non-reformable by simple dehydrocyclization reactions. On the other hand, demand for propane and butane (Liquefied Petroleum Gas) is increasing at a growth rate of over 14% every year in India, where it is widely used in homes for cooking. LPG demand is expected to accelerate further in the future because of its potential use as a clean transportation fuel. Current petroleum production and refining capacities are not sufficient to meet the deficit and growing need for LPG [1,2]. This situation suggests the need for a new process that seeks to add value to light alkane feeds by converting them into LPG or low-benzene, high octane gasoline, or both simultaneously.

The conversion of hydrocarbons over acid catalyst involves carbocation intermediates and takes place at rates which are governed by the nature, number, and strength of acid sites suggesting that acid-catalyzed reactions on a given catalyst take place on sites of a narrow range of energies [3]. The zeolite, ZSM-5, is well known for its tailorable properties, in particular, acidity and shape selectivity facilitated by the medium-sized pore channels. Such features have made ZSM-5 a suitable catalyst for a number of hydrocarbon transformations such as xylene isomerization, toluene disproportionation, and methanol to gasoline and olefins [4,5]. The number and strength of acid sites are controlled by amount and distribution of aluminum in the zeolite framework which depends on the silica-alumina ratio of the gel during zeolite synthesis. The silica-alumina ratio could also be modified post-synthesis, e.g., by hydrothermal treatment.

It has been known that ZSM-5 increases LPG-range products when used as an FCC additive. Further, earlier studies in our laboratory have led to the development of zinc-aluminosilicate of MFI structure, which has good activity for the conversion of NGL to aromatics [6-8]. The knowledge of these systems led us to study the possibility of exploiting ZSM-5-based catalysts for the production of LPG and gasoline by suitable modification of catalytic properties. In this quest, we have developed a novel zeolite-based catalyst whose efficacy for conversion of light alkane/NGL feedstocks to LPG and gasoline has been thoroughly evaluated on both model compounds and commercial feedstocks. The catalyst and process—designated Naphtha to Gas and Gasoline (NTGG)—is relevant to refiners because of its ability to consume potentially surplus light alkane feedstocks and produce supply-constrained products such as LPG along with high-octane, low-benzene gasoline.

Experiments

ZSM-5 zeolite with Si/Al ratio of 35 was synthesized from the silica-alumina-sodium-water gel system in a stainless steel reactor. Its acidity properties were tailored by treating it with steam, nitric acid, and the incorporation of metal ions such as Zn and Pt. Steam treatment was conducted in a shallow bed reactor with 100% steam at controlled water flow rate and reactor temperatures ranging from 300 to 600 °C, for a duration of 3 hours. Acid leaching was conducted with 3N nitric acid at 100 °C, while metal incorporation was carried out by incipient wet impregnation of metal salts [8].

The as-synthesized and modified zeolite samples were characterized using nitrogen adsorption/desorption, XRD, XRF, IR, and microcalorimetric ammonia adsorption. The performance of these catalysts was evaluated in two phases. The first phase was used to select one catalyst out of several several formulations using *n*-heptane as a model reaction, while the second phase involved further testing on the selected catalyst using industrial feedstocks such as light naphtha (LN), natural gas liquid (NGL), and udex raffinate. The catalyst evaluation was conducted in a fixed-bed micro reactor at reaction temperatures of 400 to 500° C, 10 kg/cm² pressure using nitrogen as carrier gas with N₂/HC molar ratio of 2.

Results and Discussion

X-ray diffraction patterns of the synthesized ZSM-5 samples revealed the formation of ZSM-5 without any impurity phases. The steamed and acid-treated samples had some changes in the intensities of major peaks suggesting increased hydrophobicity because of framework dealumination [9]. X-ray fluorescence, Si²⁹, and Al²⁷ NMR studies indicated variations in the amount and nature of alumina in the ZSM-5 samples after steaming and acid treatment. Si²⁹ MAS NMR was used to determine the framework Si/Al ratios and the phenomenon of steam dealumination was identified from higher Si/Al ratios and the presence of octahedral alumina.

Microcalorimetric adsorption of ammonia on the zeolites and resulting enthalpy of adsorption, as a function of volume of ammonia adsorbed were determined. The initial heat of adsorption indicates the maximum strength of acid site. As expected, the total amount of ammonia adsorbed per gram of catalysts decreased with steam dealumination. However, at a certain degree of dealumination, the samples exhibited a high value of initial heat of adsorption related with the involvement of extra-framework alumina in the creation of very strong acid sites.

Performance of various ZSM-5 catalysts towards *n*-heptane conversion is given in Figure 1, where based on the nature of utilization the product was broadly classified into five groups, namely, (1) fuel gas (methane, ethane and ethylene), (2) LPG (propane and butane), (3) BTX (benzene, toluene and xylenes), (4) C₅+ paraffins (pentane, hexane and heptane), and (5) C₉+ (higher aromatics).

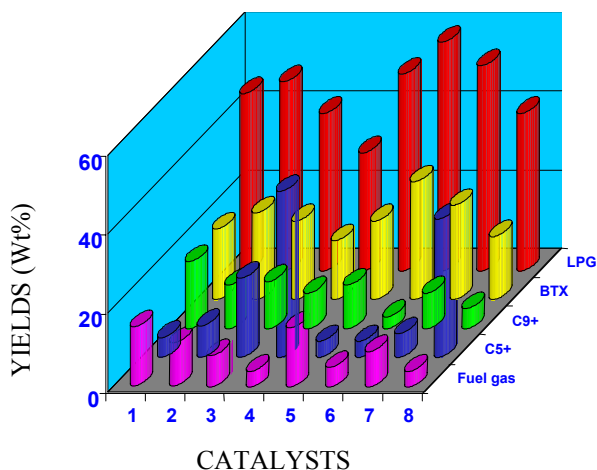


Figure 1. Effect of catalyst properties on product distribution

The results indicated a change in product selectivities after the modification of ZSM-5 properties by pre- and post-synthesis modifications. A general trend was the decrease in selectivity to fuel gas with simultaneous increase in LPG and aromatics, which is advantageous for achieving the desired product quality. However, careful analysis of the data suggests the influence of various factors on the product selectivity such as the amount and nature of extra-framework in zeolites. The criteria of catalyst selection is to maximize the production of LPG and BTX with minimal amount of fuel gas and C₅+ paraffins, where the catalyst HZ-6 exhibited the best performance with 56 wt% LPG and 36 wt% BTX in n-heptane conversion. Further testing with commercial feedstocks on this catalyst was also performed whose results are presented in Table 1. The lower IBP (initial boiling point) and FBP (Final boiling point) of the feedstocks indicate the lower average carbon number of the feed.

Table 1. Performance towards industrial feedstocks

Feed	n-C ₇	NGL	UR [*]	LN-1	LN [#] -2
Feed Characteristics					
IBP	98.0	65.1	46.1	70.0	87.0
FBP	98.0	90.0	131.9	90.0	137.0
Density	0.68	0.70	0.68	0.72	0.79
Product Yield (wt%)					
Fuel gas	2.2	4.5	9.2	5.6	3.1
LPG	56.0	55.4	52.0	55.0	51.2
BTX	36.0	28.2	29.8	32.5	39.0
C ₅ +	3.0	9.8	7.0	3.0	2.0
C ₉ +	2.8	2.1	2.0	3.9	4.7

*Udex raffinates; [#]Light naphtha

The product analysis indicates that the catalyst exhibits high conversions for all the industrial feedstocks with minor changes in selectivities for LPG and aromatics irrespective of the minor differences in feed characteristics caused by hydrocarbon composition. The higher aromatic yield observed in LN-2 conversion can be ascribed to the higher FBP of the feed. It is interesting to see that the decrease in aromatic yield was always accompanied by a simultaneous increase in LPG.

Conclusions

The authors have demonstrated the development of zeolite-based catalysts using novel modifications for the utilization of light alkane feedstocks for the production of LPG and low benzene-containing gasoline. The total yield of LPG and aromatics over this catalyst was found to be more than 80 wt% and is highly attractive for commercial applications.

References

1. Haun, R.R., Otto, K.W., and Whitley, S.C., *Oil Gas J.*, 13 June 1994, 92(24), 54.
2. *LPG News of India*, March 1996, p 17.
3. R.B. Borade, S.G. Hegde, S.B. Kulkarni, and P. Ratnasamy, *Appl. Catal.*, 13 (1984) 27.
4. S.L. Meisel, J.C. Mc Cullough, C.H. Lechthaler, P.B. Weisz, *Chem. Tech.*, 6 (1976) 86.
5. D.H. Olson, and W.O. Haag, *Am. Chem. Soc. Symp. Ser.*, (1984) 248-275.
6. A.R. Pradhan, N. Viswanadham, S. Suresh, N. Ray, Uma Shanker and T.S.R. Prasada Rao. *US Patent No. 6177374*
7. A.R. Pradhan, N. Viswanadham, Mohanlal Sharma, Uma Shanker, N. Ray, and T.S.R. Prasada Rao, *US Patent No. 5961818*
8. N. Viswanadham, A.R. Pradhan, N. Ray, S.C. Vishnoi, Uma Shanker and T.S.R. Prasada Rao, *Applied Catalysis: A*, 137, 1996, 225.
9. N. Viswanadham, Takafumi Shido, Takehiko Sasaki, and Yasuhiro Iwasawa *J.Phy.Chem. B*, 106 (2002) 10955-10963

KINETIC STUDY ON SOLVENT SWELLING OF SINGLE COAL PARTICLES IN PYRIDINE

Satoru Murata, Tomohiro Yokoyama, Toshifumi Sako, Hong Gao, Koh Kidena, and Masakatsu Nomura

Department of Applied Chemistry, Faculty of Engineering, Osaka University, 2-1 Yamada-oka, Suita, Osaka 565-0871, Japan

Introduction

Coal is a very complicated mixture of organic and inorganic materials, organic portions of which are believed to consist of numerous polycyclic aromatic compounds linked to each other by methylenes, ethers, and naphthenes. In order to obtain the structural information, many studies have been conducted including spectroscopic studies, destructive conversions and detailed analyses of the resulting products, and measurements of physical properties. Density of cross-link is one of the most important structural factors affecting physical properties and chemical reactivities of coal. In general, measurements of solvent swelling have been conducted to obtain the information of three-dimensional arrangement of organic portions of coals. Major methods for getting the data of swelling are (1) volumetric measurement based on packed bed and (2) gravimetric method using solvent sorption from vapor phase. Both methods have several advantages and shortcomings. One of the most important drawbacks in both methods, the authors think, is that these can give only the average values for each parameter such as kinetic parameters, activation energy, cross-link density, etc. Coal is considered to be a complicated heterogeneous mixture, therefore, all structural features should have a kind of distribution. A microscopic observation of swelling of coal particles is one of the methods to solve the above problem. Using this orthogonal microscope coupled with an image analysis system, the authors conducted swelling measurements of four kinds of coal particles to examine the distribution of kinetic parameters, and estimation of coal structural features such as average number of carbons between cross-link points.¹⁻² One drawback of the apparatus employed in these studies is the lack of the method to control the temperature of the solvent. This may lead to ambiguity of the data obtained. Therefore, an improvement of the apparatus for enabling the measurement of the solvent swelling at different temperature was conducted in the present study to re-examine the kinetic parameters. The authors also tried to obtain the activation energy of the solvent swelling and the effects of pretreatments of coal on the rate and activation energy of swelling.

Experimental

Samples and reagents. Witbank coal sample was provided by the Iron and Steel Institute, Japan (ISIJ), whose ultimate analysis was as follows; C 82.5, H5.0, N 2.0, O+S (by diff.) 10.5 wt%, daf. The sample was ground to coarse particles ranging from 0.20 to 0.25 mm of a diameter and dried at 40 °C *in vacuo* for a night before use. Pyridine (solvent for swelling experiments) was commercially available as a reagent grade and used without further purification.

Experimental apparatus and procedure. Details of the experimental apparatus used in this study were described elsewhere. Basically, it consists of a pair of microscopes connected with color video camera systems to monitor orthogonally the behavior of the coal particles in a sealed solvent cell (made from a transparent quartz glass). This image analysis system was used for sampling the time-resolved images and evaluating the time-resolved volumetric swelling ratio of the coal particles quantitatively. In order to carry out the kinetic study, a brand-new cell was developed (see Figure 1).

Here, the temperature of the water could be controlled with 0.5 °C from the determined one.

Under the conditions of atmospheric pressure and the controlled temperature, 3 mL of pyridine was injected into the cell and the system was kept for at least 30 min until the temperature of pyridine approached to the determined temperature. Then, the coal particles (typically 5 pieces) were randomly placed into cell, and sampling of images was started until a quasi-equilibrium state of swelling was attained (about 24 h, in the case of Witbank coal). The recorded images were directly examined and analyzed on an Apple Power Macintosh computer with an image processing software, NIH Image (ver. 1.61, from NIH, USA). The time-resolved volumetric swelling ratios of coal particles at time *t* ($Q_{v,t}$) were defined as the average value calculated with the equivalent volume converted from the two projection areas of the particles measured orthogonally by two cameras. Detailed expressions for calculation of the volumetric swelling ratio of the coal particles can be found elsewhere.

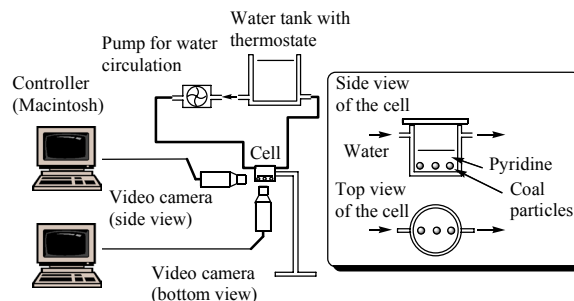


Figure 1. Schematic view of the apparatus for swelling experiments.

Results and Discussion

Kinetics of Witbank coal particles in pyridine. By using a newly prepared cell, swelling experiments of 35 particles of Witbank coal were conducted in pyridine at 20 °C. Swelling kinetics could be simulated by using the following empirical equations.

$$M_t / M_e = kt^n \quad (1)$$

$$(Q_{v,t} - 1) / (Q_{v,e} - 1) = M_t / M_e \quad (2)$$

$$(Q_{v,t} - 1) / (Q_{v,e} - 1) = kt^n \quad (3)$$

$$\ln [(Q_{v,t} - 1) / (Q_{v,e} - 1)] = \ln(k) + n \ln(t) \quad (4)$$

where, M_t and M_e mean amounts of the solvent penetrated into coal particles both at *time*=*t* and at *quasi-equilibrium* stage, respectively, $Q_{v,t}$ and $Q_{v,e}$ indicate volumetric swelling ratios at *time*=*t* and at *quasi-equilibrium* stage, respectively, *k* is rate constant for swelling, and *n* is a number that crudely indicates the nature of the solvent diffusion.

By using these equations, 35 sets of *k*, *n*, and $Q_{v,e}$ were obtained for 35 particles of Witbank coal.

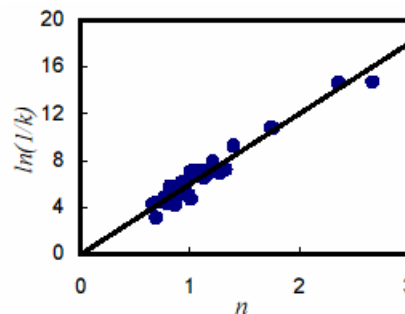


Figure 2. Correlation between *n* and $\ln(1/k)$ in swelling of Witbank coal particles in pyridine at 20 °C.

Then, the authors investigated the correlation of these swelling parameters and found that the parameter $\ln(1/k)$ is proportional to the parameter n as shown in **Figure 2**. Using a proportional constant, β , eq. 4 can be replaced with eq. 6.

$$\ln(1/k) = n\beta \quad (5)$$

$$\ln[(Q_{v,t} - 1)/(Q_{v,e} - 1)] = n\ln(t) - n\beta \quad (6)$$

The authors also found that the parameter n changed from 0.6 to 2.6 and its distribution could be simulated by double exponential function as shown in **Figure 3**, the latter findings were reported previously.

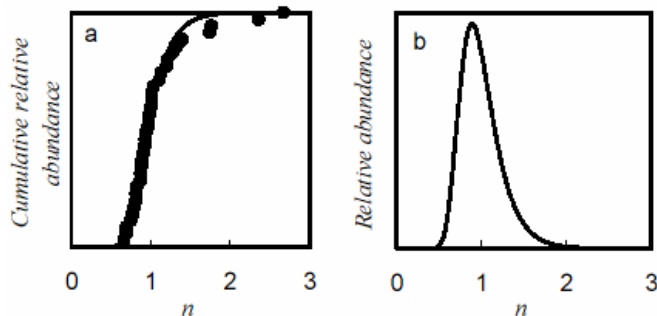


Figure 3. Distribution of n and curve fitting results (a) and differential form of fitting function (b).

Activation energy of swelling. The authors conducted the swelling experiments of Witbank coal particles in pyridine at 30 and 40 °C for evaluation of its activation energy. By using the same methods as mentioned above, kinetic parameters for swelling at 30 and 40 °C were obtained. Activation energy can be calculated by using a well-known equation:

$$\ln(k) = -E_{act} / RT + \ln(A) \quad (7)$$

Using eq. 5, eq. 7 can be transformed into eq. 8.

$$E_{act} = -Rd[\ln(k)]/d(1/T) = nRd\beta/d(1/T) \quad (8)$$

Eq. 8 indicates that activation energy can be calculated based on the value of $d\beta/d(1/T)$. The value $d\beta/d(1/T)$ can be obtained from the slope of the plots of β vs. reciprocal of temperature as shown in **Figure 4**.

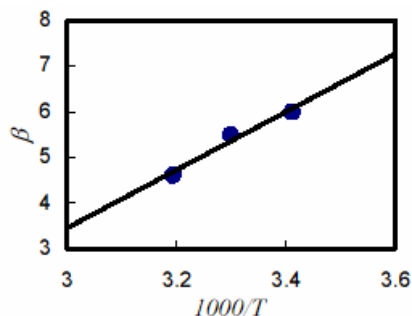


Figure 4. Temperature-dependence of the parameter, β , from the solvent swelling of Witbank coal in pyridine at 20–40 °C.

The value, $d\beta/d(1/T)$, was estimated to be 6.33×10^3 from **Figure 4**. From eq. 8 and $d\beta/d(1/T)$, E_{act} for swelling of Witbank coal particles in pyridine could be estimated to be:

$$E_{act} = 12.8 \times n \text{ (in kcal/mol)} \quad (9)$$

As shown in **Figure 3**, the parameter n had some distribution from 0.6 to 2.6, and the authors reported that the distribution of n could be simulated by double exponential distribution function. Based on these results, the authors simulated the distribution of activation energies, the results being shown in **Figure 5**.

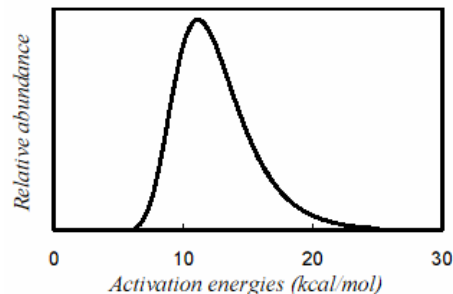


Figure 5. Distribution of the activation energies of swelling of Witbank coal particles in pyridine.

Effects of pretreatments on the kinetics of swelling.

The authors examined the effects of pretreatments of coal particles on the kinetics of solvent swelling. Pyridine pre-extraction, *O*-acetylation by acetic anhydride in pyridine, and HCl-leaching were employed as pretreatments of coal. These pretreatments were found to enhance the rate of swelling. It is interesting to note that distribution of n of the particles after *O*-acetylation and pyridine pre-extraction changed drastically.

Figure 6 shows the distribution of the activation energies of the swelling of original and treated Witbank coal particles.

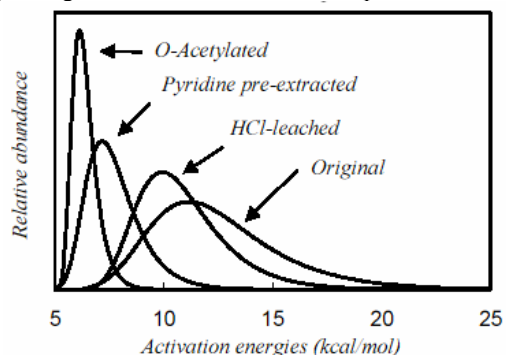


Figure 6. Distribution of Activation Energies from swelling of original and treated Witbank coal particles in pyridine.

Average and dispersion of activation energies also changed by these pretreatments. Changes of average values of E_{act} may result from the change of non-bonding interactions in the coal. *O*-Acetylation cleaves the hydrogen bondings. HCl-leaching cleaves ionic bonding by inorganic salts. Pyridine extraction may remove interaction via low-molecular weight compounds. Therefore, energy barriers for solvent penetration were reduced. Origin of the change of dispersion was not clear. One possibility is the induced rearrangement of three-dimensional structure of the coal by pyridine, because *O*-acetylation and extraction treatment used pyridine.

References

- (1) Gao, H.; Artok, L.; Kidena, K.; Murata, S.; Nomura, M. *Energy Fuels*, **1998**, *12*, 881.
- (2) Gao, H.; Nomura, M.; Murata, S.; Artok, L. *Energy Fuels*, **1999**, *13*, 518.

SHAPE SELECTIVE METHYLATION OF 4-METHYLBIPHENYL WITH METHANOL OVER MgO/HZSM5

Xinwen Guo^{a*}, Jian-Ping Shen^b, Lu Sun^b, Chunshan Song^b and Xiangsheng Wang^a

^aState Key Laboratory of Fine Chemicals, Dalian University of Technology, Dalian 116012, China

^bClean Fuels and Catalysis Program, The Energy Institute and Department of Energy & Geo-Environmental Engineering, The Pennsylvania State University, 209 Academic Projects Building, University Park, PA 16802, USA

Introduction

Shape-selective alkylation of polycyclic hydrocarbons has been the focus of many recent studies [1-9] for preparation of symmetric intermediates such as 4,4'-dialkylbiphenyl (4,4'-DABP) or 2,6'-dialkyl-naphthalene (2,6'-DAN), the important precursors for advanced polymer materials [1]. In the preparation of 4,4'-DABP, the alkylation agents can be either large group like isopropyl or the small one such as ethyl and methyl groups. The results in literature show that it is extremely difficult to obtain shape selectivity to 4,4'-dimethylbiphenyl [8,9]. Recently, some breakthrough on the methylation of 4-methylbiphenyl with methanol was achieved in which the selectivity to 4,4'-DMBP can be up to as high as 65% over HZSM-5 modified with inorganic P compound [10]. Over MgO modified HZSM-5 catalyst, the selectivity to 4,4'-DMBP is up to 80% [11]. In this paper, effects of catalyst activation and the reaction conditions on the methylation of 4-MBP with methanol over MgO/CBV8020 were investigated.

Experimental

HZSM-5 (CBV8020, 80) was obtained from PQ Corporation and calcined at 540 °C for 5 h.

The MgO/CBV8020 was prepared as follows: a solution was prepared from 1.101 g Mg(NO₃)₂·6H₂O and 20 ml distilled water, 3 g CBV8020 was added into the solution under stirring at room temperature. After 15 minutes, the mixture was placed into an oven (120 °C) and dried overnight, and then calcined at 450 °C for 5 hrs. The loading of MgO is about 5.6 wt%.

The acidic properties of MgO/CBV8020 sample were measured by TPD of ammonia on Autosorb 2910 apparatus. The samples were outgassed at 250 °C prior to BET sorption of N₂ to measure surface areas and total pore volumes (Autosorb-1). Micropore and mesopore volumes were calculated using the t-plot method.

Methylation of 4-methylbiphenyl was carried out in a fixed-bed, quartz flow reactor. About 0.30 g catalyst is placed in between quartz beads and activated at 450 °C for 1 h, then cooled down to 300 °C. The typical reaction conditions are as follows: feed 4-methylbiphenyl: methanol: mesitylene = 1:5:5 (mol ratio), reaction temperature 300 °C, N₂ flow 20 ml/min. Analysis of products was carried out by GC-MS and GC with BETA DEX[®] 120 column (60 m *0.25 mm). The typical analysis conditions are as follows: He flow 1.5 ml/min inside the capillary column, 300 °C for both detector and injector, the initial GC oven temperature 145 °C, the ramp 1 °C/min to final 190 °C, and then kept at the final temperature for 15 min.

Results and discussion

SEM of CBV8020 shows that the crystal size is about 1~3 μm. XRD spectra of CBV8020 and MgO/CBV8020 show that MgO modification leads to the decrease of the relative crystallinity, no crystalline MgO. According to the literature [12], the XRD-undetectable part of MgO can be highly dispersed onto the surface of ZSM-5. TPD curves of CBV8020 and MgO/CBV8020 show that the weak acidity in HZSM-5 decreases after MgO modification.

During the preparation of MgO/CBV8020, Mg nitrate is decomposed at 330 °C. So, the effect of calcination temperature on the methylation of 4-MBP over the catalyst was investigated.

Table 1 Effect of calcination temperature on methylation of 4-MBP with methanol (Reaction time is 75 min)

Calcination temperature (°C)		450	500	550	600	650
Conversion (%)		8.3	8.1	9.7	6.1	7.8
Yield (%)	BP	0.6	0.6	0.6	0.5	0.7
	MBPs	2.3	2.5	2.6	1.2	1.6
	DMBPs	5.3	5.1	6.4	4.3	5.5
	others	0.0	0.0	0.0	0.0	0.1
MBP composition (%)	2-	0.3	0.0	0.5	0.1	0.1
	3-	2.2	2.6	2.4	1.2	1.6
	4-	97.5	97.4	97.2	98.7	98.3
DMBP composition (%)	2,2'-	3.8	0.0	0.0	4.7	5.0
	3,3'-	1.5	0.0	1.7	1.4	1.7
	3,4'-	13.6	15.6	14.8	17.2	12.7
	4,4'-	78.1	80.7	79.7	74.5	76.3
	2,3'-	3.0	3.7	3.8	3.3	3.5
	others	0.0	0.0	0.0	0.9	0.9

It can be seen from Table 1 that with an increase in the calcination temperature of MgO/HZSM-5, the selectivity to 4,4'-DMBP increases to 80.7% when the calcination temperature is 500 °C, and the conversion of 4-MBP is 9.7% when that calcination temperature is 550 °C. The optimum scope is between 450-550 °C.

Table 2 lists the effect of reaction temperature on methylation of 4-MBP with methanol over MgO/CBV8020 zeolite catalyst. It can be seen that with an increase in the reaction temperature, the conversion of 4-MBP decreases and the selectivity to 4,4'-DMBP first increases, then decreases. The selectivity to 4,4'-DMBP is up to 79.7% when the reaction temperature is 300 °C. With an increase in the reaction temperature, the isomerization of 4-MBP into 3-MBP increases, and the isomerization of 4,4'-DMBP into 2,3'- and 3,4'-DMBP increases.

Table 2. Effect of reaction temperature on methylation of 4-MBP with methanol (Reaction time is 75 min)

with increasing reaction time (s 7.5 min)							
Reaction temp (°C)		275	300	325	350	375	400
Conversion (%)		7.1	9.7	9.4	10.7	12.7	13.3
Yield (%)	BP	0.6	0.6	0.5	0.6	0.6	0.6
	MBPs	1.2	2.6	3.5	5.7	7.2	8.4
	DMBPs	5.3	6.4	5.2	4.4	4.6	4.0
	others	0.0	0.0	0.0	0.0	0.0	0.0
MBP composition (%)	2-	0.0	0.5	0.2	0.0	0.2	0.1
	3-	1.3	2.4	3.6	6.0	7.4	8.7
	4-	98.7	97.2	96.3	94.0	92.4	91.2
DMBP composition (%)	2,2'-	5.8	0.0	4.6	2.3	3.1	4.7
	3,3'-	1.3	1.7	2.1	2.8	3.3	3.5
	3,4'-	14.5	14.8	15.5	20.0	21.6	23.3
	4,4'-	75.8	79.7	72.7	70.0	66.0	61.9
	2,3'-	2.6	3.8	4.3	5.3	6.1	6.7
	others	0.0	0.0	0.8	0.0	0.0	0.0

* Corresponding author. Email: guoxw@dlut.edu.cn; Fax: 86-411-3689065; Tel:86-411-3689065

The effect of WHSV of feed on the methylation of 4-MBP with methanol was also investigated, when the WHSV increases from 2 ml/h to 6 ml/h, the selectivity to 4,4'-DMBP decreases from 79.7% to 70.0%, and the conversion of 4-MBP decreases from 9.7% to 3.6%.

The effect of reaction time on the methylation of 4-MBP with methanol shows that both the conversion of 4-MBP and the selectivity to 4,4'-DMBP decrease with reaction time. Moreover, the addition of water in the feed does not favor methylation of 4-MBP with methanol.

The effect of the amount of mesitylene on the methylation of 4-MBP was investigated, and the results are listed in Table 3.

Table 3 Effect of the amount of mesitylene on methylation of 4-MBP with methanol (Reaction time is 75 min)

4-MBP:mesitylene (molar ratio)		1:5	1:14.26
Conversion (%)		9.7	10.0
Yield (%)	BP	0.6	0.9
	MBPs	2.6	4.6
	DMBPs	6.4	4.5
	others	0.0	0.0
MBP composition (%)	2-	0.5	0.0
	3-	2.4	4.9
	4-	97.2	95.1
DMBP composition (%)	2,2'-	0.0	0.0
	3,3'-	1.7	0.0
	3,4'-	14.8	18.6
	4,4'-	79.7	81.4
	2,3'-	3.8	0.0
	others	0.0	0.0

From Table 3, it can be seen that with an increase in the amount of mesitylene, both the selectivity to 4,4'-DMBP and 4-MBP conversion increase a little. However, the activity stability improves a lot, after 375 min reaction, the selectivity to 4,4'-DMBP is about 80%, and 4-MBP conversion is about 8% (Figure 1). 4-MBP conversion decreases to 2% after 700 min. After regeneration by calcinating at 550 °C for 4 h, 4-MBP conversion is about 8%, while the selectivity to 4,4'-DMBP is up to 86% (Figure 2). The results of N₂ physical absorption (Table 4) show that both the total surface area and microporosity decrease after reaction due to the coke, while the mesoporosity keeps constant. After regeneration, both the surface area and the porosity are the same as those of fresh catalyst.

Table 4 Properties of MgO/CBV8020 before and after reaction and after regeneration

Sample	Surface area / m ² ·g ⁻¹			Porosity / ml·g ⁻¹		
	Total	Micro	Meso	Total	Micro	Meso
Fresh	314	267	47	0.21	0.13	0.08
After reaction	200	160	40	0.14	0.08	0.06
After regeneration	312	257	55	0.21	0.13	0.08

Acknowledgements. The project was sponsored by the Scientific Research Foundation for the Returned Overseas Chinese Scholars, Ministry of Education, and the Pennsylvania State University.

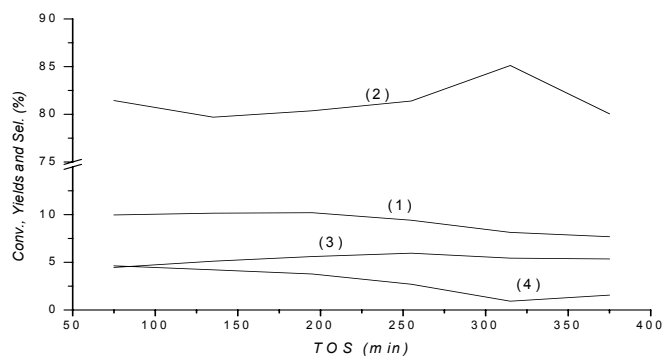


Figure 1 Methylation of 4-MBP with methanol over Mg/CBV8020 (4-MBP: methanol: mesitylene=1:5:14.26)

(1) Conversion of 4-MBP; (2) 4,4'-DMBP Selectivity; (3) DMBP Yield of; (4) MBP Yield

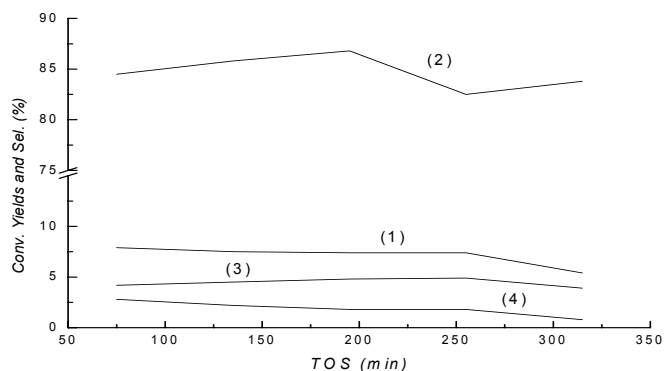


Figure 2 Methylation of 4-MBP with methanol over Mg/CBV8020 after regeneration (4-MBP: methanol: mesitylene=1:5:14.26)

(1) Conversion of 4-MBP; (2) 4,4'-DMBP Selectivity; (3) DMBP Yield of; (4) MBP Yield

References

- [1] C. Song, J.M.Graces and Y. Sugi, eds., Shape-selective Catalysis. Chemicals Synthesis and Hydrocarbon Processing, ACS Symp. Ser., **2000**, Vol. 738(Am. Chem. Soc., Washington, DC) p.410; C. Song, Cattech, **2002**, 6 (2), 64.
- [2] D. Fraenkel, M. Cherniavsky, B. Ittah and M. Levy, J. Catal. **1986**, 101, 273.
- [3] G.S. Lee, J.J.Maj, S.C. Rocke and J.M.Garces, Catal. Lett. **1989**, 2, 243.
- [4] C. Song and S. Kirby, Micropor. Mater. **1994**, 2, 467.
- [5] A.D. Schmitz and C. Song, Catal. Today, **1996**, 31, 59; A.D. Schmitz and C. Song, Catal. Lett. **1996**, 40, 59.
- [6] Y.Sugi and M. Toba, Catal Today, **1994**, 19, 187.
- [7] J.P.Shen, J. Ma, D. Jiang and E. Min, Chem. Res. Chin. Uni. **1993**, 14, 845; J.P.Shen, J. Ma, D. Jiang and E. Min, Chem. Res. Chin. Uni. **1993**, 14, 1135.
- [8] Y.Sugi, Y. Kubota, K. Nakajima, K. Kunimori, H. Hanaoka and T. matsuzaki, Am. Chem. Soc. Div. Petrol. Chem. Prepr. **1998**, 43, 264.
- [9] C. Brechtelsbaur and G.Emig, Appl. Catal. **1997**, 161, 79.
- [10] J.P. Shen, L. Sun, C. Song, Catal. Lett. **2000**, 65, 147; J.P. Shen, L. Sun, C. Song, Stud. Surf. Sci. Catal. **2001**, 135, 151.
- [11] X.W. Guo, J.P. Shen, S. Lu, C. Song, X. S. Wang, Catal. Lett. **2003**, 87, 25.
- [12] D. E. Jiang, B. Y. Zhao, Y C Xie, et al., Applied Catalysis A: General, **2001**, 219, 69-78.

PLASMA ENHANCED PREPARATION OF Pt/NaZSM-5 CATALYSTS FOR NO REDUCTION BY METHANE

Neng Zhu¹ and Yue-ping Zhang^{2,3}*

¹College of Environmental Science and Engineering, ²Department of Chemistry, ³ABB Plasma Greenhouse Gas Chemistry Laboratory, Tianjin University, Tianjin 300072, China

Introduction

An intensive investigation has been conducted to reduce nitrogen oxides that are extremely harmful pollutants. The reported investigations include catalytic reduction by hydrocarbons (esp., methane)[1-5], plasma reduction [6,7] and the combination of plasma and catalytic reduction [8-13]. The catalytic reduction has a higher selectivity but the lifetime of catalysts needs to be improved. Plasma conversion shows a high conversion rate for removing nitrogen oxides (NO_x). But the poor selectivity limits its application. The combination of plasma and heterogeneous catalyst has been found recently to be a promising technology for NO_x reduction [8-13]. In general, the investigated combination includes single stage plasma catalytic reactor system and two-step plasma catalytic reactor system. The first reactor system employs a direct interaction between catalyst and plasma species during NO_x reduction. The catalyst must show some field-dependent structural and electronic properties that can response effectively to the influence of plasmas. The two-step system normally uses plasma in the first step to convert NO to other nitrogen oxides that are easier to be converted catalytically in the second step. Evidently, for either single stage or two-step combination technology, a good catalyst is very important. In this work, we report a different technology: the plasma is used first to prepare catalyst and then the prepared catalyst is applied for NO reduction by methane. The experiment confirms that a better catalyst has been achieved. A remarkable improvement in the stability has been achieved by this plasma treatment.

Experimental

A Pt/NaZSM-5 catalyst was prepared by incipient wetness impregnation method. The support NaZSM-5 was commercially obtained (Nankai University Catalyst Plant, China) and was applied as received. This support was first impregnated in an aqueous solution of chloroplatinic acid (H₂PtCl₆) for 18 hours. After impregnation, the resulted sample was dried at 110 °C for eight hours. The obtained sample was then treated by plasma at room temperature for 30 minutes before further calcination at 500 °C for four hours. We have successfully utilized a dc glow discharge for plasma treatment of catalyst. During plasma treatment, the catalyst powder (40-60 mesh) was held in a container that is placed in the discharge tube. The glow discharge [14], one of cold plasma phenomena, is initiated by a dc high voltage generator at low pressure. The catalyst was located in the "positive column" of glow discharge [14] that was generated at ca. 120 Pa using argon as the plasma-forming gas. This region is characterized by its high-energy electrons. The applied voltage to the electrode was measured using a high voltage probe (Tektronix P6015A) with a Tektronix TDS210 digital real-time oscilloscope. The loading amount of Pt is 0.1%, 0.2%, 0.3% and 0.5%, respectively. The effect of the Pt loading amount on the NO reduction by methane has been investigated in this work.

The catalytic NO reduction by methane was carried out in a quartz tube reactor. The inner diameter of the quartz tube is 6 mm. The catalyst loaded is 0.1 g. The feed gas contained 3989.1 ppm NO,

7845.2 ppm CH₄ and helium makes the balance. The total flow rate was kept at 100 Nml/min (GHSV= 47922 h⁻¹). Before reaction, the catalyst was pretreated at 773 K under the flowing hydrogen at a flow rate of 20 Nml/min for 1 hour. Then the temperature was reduced to 573 K and the gas helium was fed into the reactor for half hour.

The feed gas and the effluent were analyzed by a GC (Agilent 4890D) with a TCD detector using a column of HP-Plot Molecular Sieve 5A. The column ID is 0.53 mm and the length is 15 m.

Results and Discussion

Figure 1 shows an effect of Pt loading amount on the NO conversion of NO reduction by methane. Evidently, almost all the catalysts exhibit an excellent low temperature activity. Except the catalyst 0.1% Pt/NaZSM-5, all the catalysts show a 100% NO conversion at the temperatures tested. For the catalyst 0.1% Pt/NaZSM-5, the NO conversion is less than 100% at the temperatures below 410 °C. This means that the loading amount has an effect on the catalytic activity.

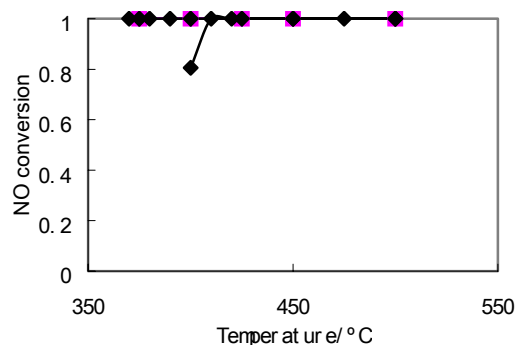


Figure 1. Comparison of activity of Pt/NaZSM-5 with different Pt loading amount (◆: 0.1%Pt; ■: 0.2%Pt; ●: 0.3%Pt; ▲: 0.5% Pt)

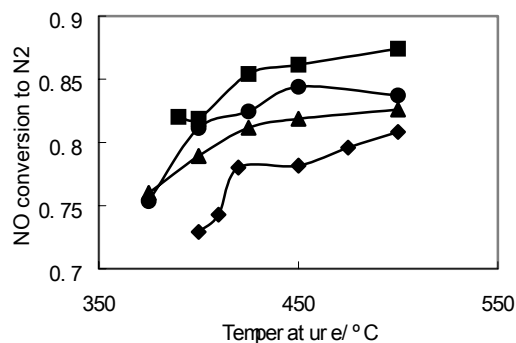


Figure 2. The NO conversion to N₂ over catalysts with different Pt loading amount (◆: 0.1%Pt; ■: 0.2%Pt; ●: 0.3%Pt; ▲: 0.5% Pt)

Figure 2 presents the effect of Pt loading amount on the selectivity of NO reduction to N₂. It is very interesting to find that the best selectivity of the catalysts tested is presented over the catalyst

0.2%Pt/NaZSM-5. The Pt loading amount less or higher than 0.2% is not favored for the NO reduction to nitrogen. Further catalyst characterization is being conducted for a better understanding of the reactions.

Conclusions

The present investigation confirms the glow discharge plasma-enhanced preparation will lead to a better catalyst for NO reduction to nitrogen. The Pt loading amount has a little effect on the catalytic conversion if the loading amount of Pt is larger than 0.1%. However, the Pt loading amount has a significant influence on the selectivity of NO reduction to nitrogen. The best loading amount of Pt over the NaZSM-5 zeolite support is 0.2% for NO reduction to nitrogen. We have previously found that the plasma enhanced preparation of catalyst has led to an increased stability of the catalyst. Further investigation will lead to a practical application of Pt/NaZSM-5 catalyst for NO reduction to nitrogen.

Acknowledgement. The support from the Tianjin City Committee of Science and Technology is greatly appreciated. Part of instrument and equipment applied in this investigation was donated by ABB Switzerland Ltd., which is deeply appreciated.

References

- (1) Loughran C.J.; Resasco D.E. *Appl. Catal. B* **1995**, 5, 351.
- (2) Ozkan U.S.; Kumthekar M.W.; Karakas G. *Catal. Today* **1998**, 40, 3.
- (3) Xie S.; Rosynek M.P.; Lunsford J.H. *J. Catal.* **1999**, 188, 32.
- (4) Adelman B.J.; Sachtler W.M.H. *Appl. Catal. B* **1997**, 14, 1.
- (5) Balint I.; Miyazaki A.; Aika K.-I. *Appl. Catal. B* **2002**, 37, 217.
- (6) Luo J.; Suib S.L.; Marquez M.; Hayashi Y.; Matsumoto H. *J. Phys. Chem. A* **1998**, 102, 7954.
- (7) Kim H.H.; Prieto G.; Takashima K.; Katsura S.; Mizuno A. *J. Electrostatics* **2002**, 55, 25.
- (8) Kim H.H.; Takashima K.; Katsura S.; Mizuno A. *J. Physics D* **2001**, 34, 604.
- (9) Rajanikanth B.S.; Ravi V. *Plasma Sci. & Tech.* **2002**, 4, 1399.
- (10) Yoon S.; Panov A.G.; Tonkyn R.G.; Ebeling A.C.; Barlow S.E.; Balmer M.L. *Catal. Today* **2002**, 72, 243.
- (11) Roh H.-S.; Park Y.-K.; Park S.-E. *Chem. Lett.* **2000**, 578.
- (12) Francke K.P.; Miessner H.; Rudolph R. *Catal. Today* **2000**, 59, 411.
- (13) Bröer S.; Hammer T. *Appl. Catal. B* **2002**, 28, 101.
- (14) Liu C.-J.; Vissokov G.P.; Jang B. *Catal. Today*, **2002**, 72, 173.

CATALYTIC SYNTHESIS OF DIETHYL CARBONATE FROM CARBON MONOXIDE AND ETHYL NITRITE ON SUPPORTED Pd CATALYSTS

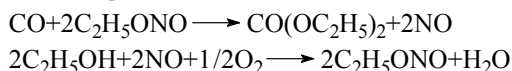
Xinbin Ma, Haifeng Shi, Zhen Zhang, Baowei Wang,
Shengping Wang, Genhui Xu

State Key Laboratory of C1 Chemistry and Technology,
School of Chemical Engineering and Technology, Tianjin University,
Tianjin 30072, China

Introduction

Diethyl carbonate (DEC) is one of the important green chemicals and widely used for organic synthesis because of having various functional groups in its molecule. DEC is a better octane blending fuel, and has more oxygen in the molecule than *tert*-butyl ether (MTBE), 40.6% versus 18.2%, which reduces emissions from gasoline and diesel engine [1]. For these reasons many studies on the production of DEC have been extensively carried out, e.g., reactions between phosgene and ethanol, oxidative carbonylation of ethanol and trans-esterification reaction. Among them, a novel type of catalytic synthesis of DEC over supported Pd catalysts using ethyl nitrite as substitutes for ethanol and oxygen was developed, which is similar to the synthesis of diethyl oxalate (DEO) in which DEC is generated as a by-product [2].

In this synthesis procedure, two separated reactions are involved. The first reaction is DEC synthesis from ethyl nitrite and CO over Pd catalysts and the second reaction is a gas-liquid reaction of ethyl nitrite synthesis from nitrogen monoxide produced in the first step, oxygen and ethanol. Ethyl nitrite produced in the second step is recycled in the process.



It was showed that the catalysts Pd on activated carbon have high activities and the better selectivity for the DMC synthesis [3]. Herein, we reported the activities of palladium catalysts for the DEC synthesis. The reason for deactivation of catalyst PdCl₂/CuCl₂/a.c. was also investigated.

Experimental

Catalyst Preparation. A catalyst component solution containing Pd, Cu was prepared by heat-dissolving 0.437g of palladium chloride (PdCl₂) and 0.839g of cupric chloride (CuCl₂·2H₂O) in 40 ml methanol at a temperature of 40°C to 50°C. Separately, particulate activated carbon in an amount 8.725g was immersed in the solution, and the resultant mixture was stirred at room temperature for an hour. Then methanol was evaporated away from the mixture at a temperature of 50°C under a reduced pressure. The resultant mixture was dried in a nitrogen gas atmosphere at a temperature of 200°C, to provide a solid catalyst. In the resultant catalyst, a mixture of PdCl₂ and CuCl₂ was carried on a carrier consisting of the activated carbon. The total content of the metal compound in terms of metallic palladium was 3wt % by weight based on the weight of the carrier, and the atomic ratio of Pd, Cu in the catalysis was Pd: Cu=1:2.

Diethyl Carbonate Synthesis. The above solid catalyst in an amount of 3.0 ml was placed in a gas phase reaction tube having an inside diameter of 20mm and equipped with an outside jacket. The tube filled with catalyst was fixed vertically and a heating system was used to maintain the inside temperature of the reaction tube between 110°C and 120°C. A mixed gas containing ethyl nitrite (EN) prepared from ethanol, sulfuric acid and sodium nitrite, carbon

monoxide and nitrogen, consisting of 15% by volume of ethyl nitrite, 20% by volume of carbon monoxide and 65% by volume of nitrogen, was fed into the reaction tube through a top end thereof at a space velocity of 2000h⁻¹ under the ambient atmosphere pressure, to cause the carbon monoxide to react with the ethyl nitrite. The reaction products passed through a cooling trap and uncondensed gas products were analyzed by gas chromatographs with TCD detector. The liquid products collected in the cooling trap were taken out every hour, and were analyzed by GC (4890D, Agilent) with FID detector. The by-product includes diethyl oxalate (DMO), CO₂, ethyl formate (EF), and diethoxyethane (DEE). The CO and EN selectivities to DEC were calculated on the basis of the CO or EN consumed, respectively.

$$\text{CO selectivity (\%)} = \text{DEC} / [\text{DEC} + 2\text{DEO} + \text{CO}_2] \times 100$$

$$\text{EN selectivity (\%)} = \text{DEC} / [\text{DEC} + \text{DEO} + \text{DEE} + 2\text{EF}] \times 100$$

Catalyst Characterization. The specific surface areas of the catalysts were determined using a constant volume adsorption apparatus (CHEMBET-3000) by the N₂ BET method at the liquid nitrogen temperature. The XPS analysis of the catalysts was carried out on a Perkin-Elmer PHI 1600 ESCA system operated at pass energy of 29.35 eV with an aluminum X-ray source (E=1486.6 eV). The samples were mounted on the specimen holder by means double-sided adhesive tape. Spectra were recorded in steps of 0.25 eV. The Cls peak (284.6 eV) was used as the internal standard for binding-energy calibration. The deviation of the binding energy was ±0.15 eV. The pressure during the measurements did not exceed 1.6×10⁻⁸ Torr and the temperature was approximately 293 K.

Results and Discussion

Effect of Solvent. Table 1 shows the catalytic activities and properties of the catalysts PdCl₂-CuCl₂/a.c., which were made by using the same activated carbon and have the same amount of Pd and Cu. Nevertheless, PdCl₂ and CuCl₂ are dissolved in different solvent (hydrochloric acid or methanol).

Table1 The Effect of the Dissolved Solvent on the Activity and Specific Surface Area of Catalyst

Solvent	Specific surface area (m ² /g)		Conv. (%)	Selectivity (%)	STY (g/lcat.h)
	B	A			
HCl	583	286	16.3	91	199
CH ₃ OH	680	322	28.5	92	392

B, before reaction; A, after reaction.

As the result showed in the **Table1**, PdCl₂ and CuCl₂ dissolved by methanol make the catalyst have a larger specific area and we conclude it is because that using methanol to dissolve PdCl₂ and CuCl₂ enable Pd metal to be adsorbed in smaller particle on the surface of the carrier than using hydrochloric acid, therefore the catalyst showed higher catalytic behavior on terms of conversion of CO and STY of DEC, PH of the solvent used to dissolve PdCl₂ and CuCl₂ may also have effect on the catalytic behavior of the catalyst. Since the synthesis of DEC is under normal pressure, the STY of DEC is not very high. However, the specific area of the catalyst decreases greatly after reaction. Palladium species supported on activated carbon or metal oxides have been reported to aggregate easily to form Pd metal particles, especially in the presence of CO or H₂ [4]. Deactivation of supported Pd catalysts is often a consequence of reduction and migration of Pd species and the resultant growth of Pd metal. The reason responsible for the decrease of the specific area

may be because atom Pd gets to conglomerate during the reaction and the cluster of atom Pd clogged the hole of the carrier.

Catalyst Lifetime Test. The deactivation behavior of 3wt.% Pd/C for DEC synthesis reaction was studied at 388K to examine the stability of the catalysis. The relation between the formation rate of DEC, ethyl formate (EF) and DEO and the selectivity of CO and ethyl nitrite(EN) to DEC and reaction time are shown in **Figure1**.

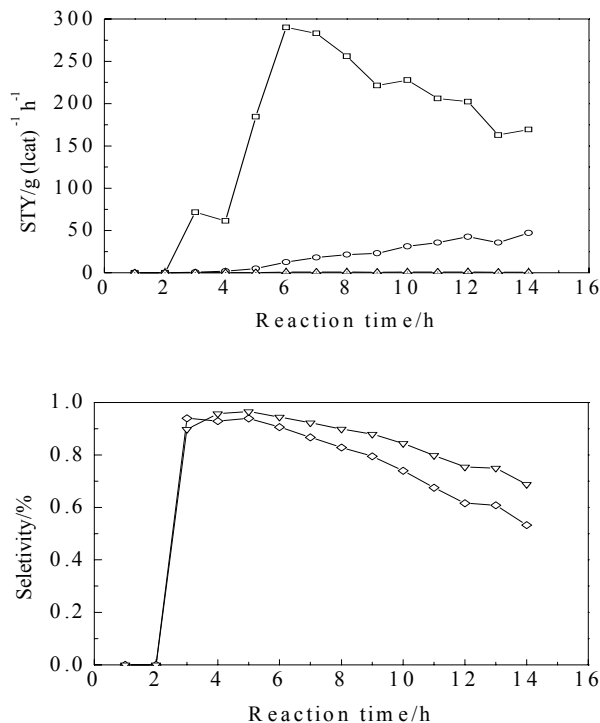


Figure 1. Catalytic behavior of 3 wt.% Pd/C for DEC synthesis as a function of reaction time. (a) Formation rates of DEC (□), EF (△) and DEO (○) and (b) Selectivity of CO (◇) and EN (▽) to DEC.

The STY of DEC reached the maximum of 290 g(lcat.h)⁻¹ after 6 h then gradually decreased and reached a steady state activity 220 g(lcat. h)⁻¹. Meantime, the DEO and EF formation increased slowly. The selectivity to DEC on the basis of CO and EN consumed decreased with the increase of the reaction time. The rate of deactivation of the catalyst in the reaction was relatively higher than in the UBE progress. It is partly because we did not add HCl gas into the system, atom Pd could not be reoxidized fully, which resulted in the deactivation of the catalyst.

Effect of Reaction Temperature. The relation between the reaction temperature and the catalytic activity of Pd/C was also investigated. The catalytic activity and the selectivity of DEC on the basis of CO consumed are shown in the **Figure 2**.

Clearly, the selectivity of DEC based on CO increased with the increase of the reaction temperatures from 100°C to 125°C. The STY of DEC gradually increased with the increase of the reaction temperature from 100°C to 120°C, beyond which the STY of DEC decreased greatly, the decomposition point of ethyl nitrite is responsible for this because the decomposition point of ethyl nitrite is 116°C under normal pressure [3].

XPS Characterization. It is demonstrated in **Table 2** that there is a peak of Cl⁻ at the binding energy 200 eV before reaction but after reaction the peak of Cl⁻ disappeared on the surface of the catalyst. As

showed in **Figure 1** the catalytic behavior of catalyst also deactivated with the loss of Cl⁻, this is the main reason for the deactivation of the catalyst. While the amount of Pd increased after reaction, it was perhaps that Pd got congregated during reaction.

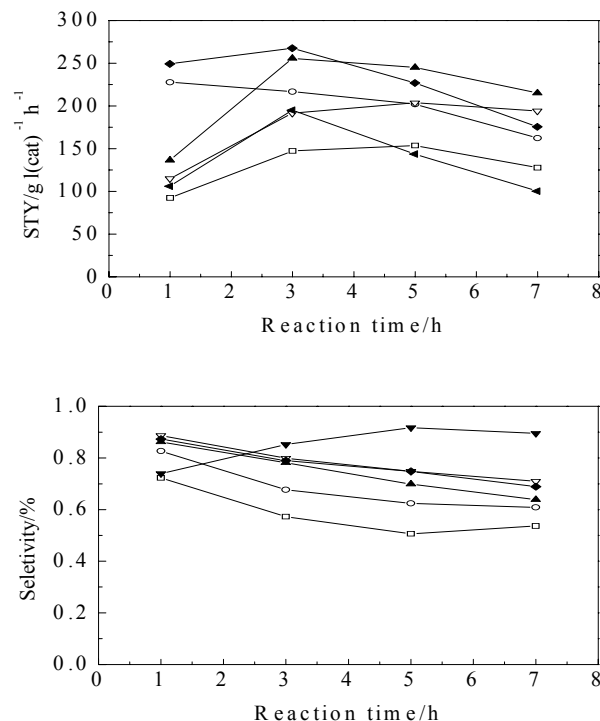


Figure 2. Effect of reaction temperature on the catalytic activity of Pd/C for DEC synthesis. 100°C (□), 105°C (○), 110°C (▲), 115°C (▽), 120°C (◆), 125°C (▼)

Table 2. The Surface Composition of Catalyst Detected by XPS

Catalyst		Surface composition (mol%)				
		C	O	Pd	Cl	Cu
3 wt.% Pd/C	B	64.0	29.2	0.6	3.4	2.8
	A	54.6	38.7	5.6	0	5.6

B before reaction; A after reaction

Conclusions

PdCl₂ and CuCl₂ dissolved in methanol can make the catalysts have a larger specific surface area and show better activity than dissolved in hydrochloric acid. The catalysts have relatively high selectivity and STY of DEC when reaction temperature is about 110 °C. The loss of chloride ion is the main reason for the deactivation of the catalysts. So how to fix chloride ion or supply chloride ion during reaction to maintain the activity of catalysts is the key problem.

References

- (1) Pacheco, M. A., Marshall, C. L., *Energy & Fuels*, **1997**, 11, 2-29.
- (2) Jiang, X. Z., Su, Y. H., Chien, S. H., *Catalysis Letter*, **2000**, 69, 153-156
- (3) Matsuzaki, T., Nakamura A., *Catalysis Surveys of Japan*, **1997**, 1, 77-88.
- (4) Yamamoto, Y., Matsuzaki, T., Tanaka, S., Nishihira, K., Ohdan, K., Nakamura, A., Okamoto, Y. *J. Chem. Soc., Faraday Trans.*, **1997**, 93, 3721-3727.

THE INFLUENCE OF POTASSIUM PROMOTER ON SYNTHESIS OF DIETHYL CARBONATE BY OXIDATIVE CARBONYLATION OF ETHANOL

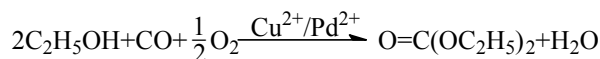
Xinbin Ma, Zhen Zhang, Shengping Wang,
Haifeng Shi, Hengjin Zhang

State Key Laboratory of C1 Chemistry and Technology,
School of Chemical Engineering and Technology, Tianjin University,
Tianjin 300072, China

Introduction

Diethyl carbonate (DEC) is one of the important green chemicals in carbonate ester and widely used for organic synthesis because it has versatile chemical properties as a nontoxic carbonylating and ethylating agent by the presence of a carbonyl group and two ethoxy groups in its molecule. Diethyl carbonate can be used as solvent, surfactant, additive of lithium cell electrolyte etc. In recent years, diethyl carbonate is found to substitute for methyl *tert*-butyl ether (MTBE), which is used as an oxygen-containing fuel additive. It has more favorable gasoline/water distribution coefficient and lower volatility than dimethyl carbonate [1], which is another promising substitute of MTBE.

Several reaction routes have been known for DEC production so far such as the traditional phosgene process, the ester exchange process, the carbon monoxide–ethyl nitrite process and the oxidative carbonylation of ethanol. The synthesis of DEC from oxidative carbonylation of ethanol can be carried out in both liquid- and gas-phases. The gas-phase process is more attractive because it avoids the drawbacks of the liquid-phase process, such as the halide corrosion and the difficulty in separating catalyst from the products. The overall reaction is:



Dunn [4] reported that the yield and selectivity of DEC were improved when the $\text{CuCl}_2/\text{PdCl}_2$ /activated carbon catalyst is treated with KOH by using a batch reactor. Roh et al. [5] used a pulse-quench-flow reactor to investigate the influence of the amounts of reactant and the reaction condition on continuous production of DEC.

Dunn concluded that the catalyst $\text{CuCl}_2/\text{PdCl}_2$ /activated carbon treated with KOH is better than other metal alkali compounds, and explained that potassium promote the reaction. In order to further enhance the conversion rate of reactants and the yield of DEC, the effects of various potassium salts promoters in catalyst $\text{CuCl}_2/\text{PdCl}_2$ /activated carbon on the reaction performance were studied in this paper. The reason for deactivation of catalyst $\text{CuCl}_2/\text{PdCl}_2$ /activated carbon was also investigated.

Experimental

Catalyst Preparation. The catalyst was prepared by impregnating activated carbon with methanol solution of CuCl_2 , PdCl_2 and a sort of potassium salts (potassium acetate, potassium citrate tribasic monohydrate, potassium sorbic, potassium chloride). Then the mixture was refluxed with vigorous stirring for 4h at 60 °C, and the methanol was removed by vacuum distillation and the catalyst was dried at 80 °C for 4h in a vacuum oven. The Cu and Pd content in the catalyst are 3wt. % Cu and 0.25wt. % Pd measured as metals. The molar ratio of the K/Cu was 1. The catalyst sample was then impregnated in a sodium hydroxide methanol solution ($\text{Cu}/\text{OH}=1$, molar ratio), and again treated in the above method. The BET specific surface area of the activated carbon employed here is 900 m^2/g .

Catalyst Evaluation. Catalytic activity was measured in a computer-controlled continuous micro reactor system (MRCS-8004B) with a stainless steel tubular reactor of 8mm inner diameter. A thermocouple was placed inside the catalyst bed for accurate temperature control. The reaction products passed through a cooling trap and uncondensed gas products were analyzed by gas chromatographs (GC-8A, Shimadzu) with TCD detector, which employed a column packed with TDX-01 and Propak-Q. The liquid products collected in the cooling trap were taken out every hour, and were analyzed by GC (4890D, Agilent) with FID detector. The reaction conditions were as follows, 2g catalyst, 0.1ml/min ethanol (as liquid), 4 sccm O_2 , 40 sccm CO , 20 sccm N_2 , reaction temperature 150°C and reaction pressure 0.64 MPa.

Catalyst Characterization. The XPS analysis of the catalysts was carried out on a Perkin-Elmer PHI 1600 ESCA system operated at a pass energy of 187.85 eV for survey spectra with a $\text{Al K}\alpha$ X-ray source ($E=1486.6$ eV). The samples were mounted on the specimen holder by means of double-sided adhesive tape. Spectra were recorded in steps of 0.80 eV. The C1s peak (284.6 eV) was used as the internal standard for binding-energy calibration. The pressure during the measurements controlled under 1.6×10^{-8} Torr and the temperature was approximately 293 K.

Results and Discussion

Dunn [4] reported that potassium promoter is better than any other promoter such as sodium, calcium, etc. In the process of synthesis dimethyl carbonate, Jiang et al. [6] concluded that potassium acetate is the most active promoter than other potassium promoter. We use different potassium salt to investigate the catalytic activity of the catalyst.

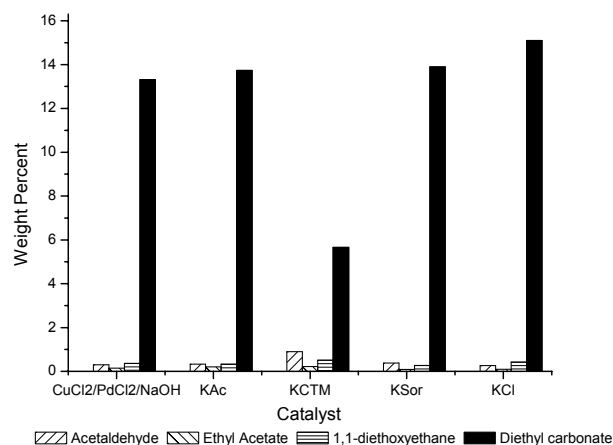
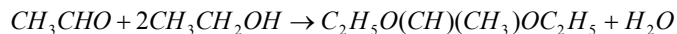
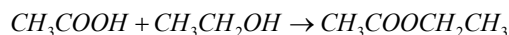
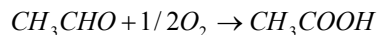
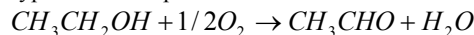


Figure 1. Influence of treating an activated carbon-supported $\text{CuCl}_2 + \text{PdCl}_2 + \text{NaOH}$ catalyst with various potassium salts on the product yields. Conditions: 2g catalyst, 0.1ml/min ethanol (as liquid), 4 sccm O_2 , 40 sccm CO , 20 sccm N_2 , reaction temperature 150°C, reaction pressure 0.64 MPa

The most of the catalysts show better activity except the catalyst in which potassium citrate tribasic monohydrate was added as a promoter as shown in **Figure 1**. The selectivity of the reaction kept steady. When KCl was added as a promoter in the catalyst $\text{CuCl}_2/\text{PdCl}_2/\text{NaOH}/\text{a.c.}$, the reaction shows the best activity. However, the selectivity of DEC dropped down slightly. This result is consistent with previously reported research conducted on the

oxidative carbonylation of methanol [6]. The formation of byproducts is independent on the main reaction of DEC synthesis. According to GC-MS analysis, the mechanism of the production of byproducts was put forward as follows:



The four steps mechanism makes it easy to carry out thermodynamic calculation and analysis.

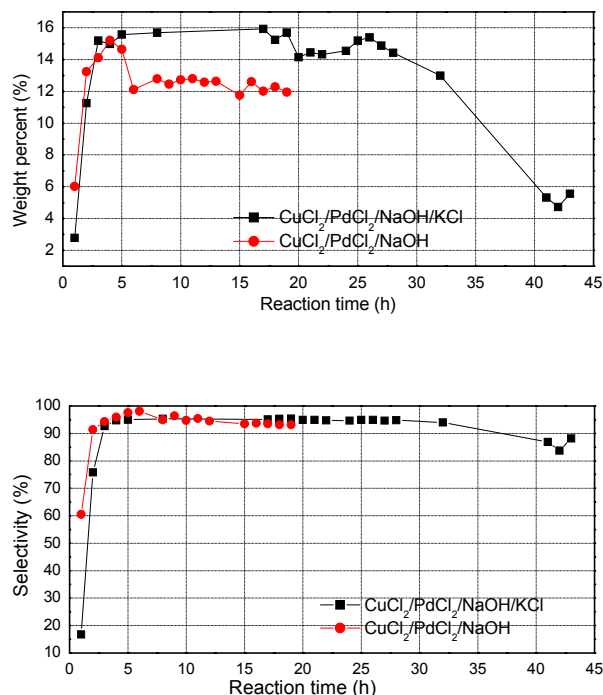


Figure 2. The difference of the product yield and the selectivity to DEC between the catalyst CuCl₂/PdCl₂/NaOH/KCl/a.c. and the catalyst CuCl₂/PdCl₂/NaOH/a.c. (40h lifetime test.)

As shown in **Figure 2**, the catalytic activity maintained steady within 30 hours after adding KCl on the catalyst, and the catalyst without adding potassium chloride deactivated after six hours run. The conversion rate dropped down about twenty percent to twelve percent. However, the selectivity of both these two kinds of catalysts kept high level. The selectivity to DEC didn't increase significantly after potassium chloride was added as a promoter. The potassium chloride can improve the catalytic activity of the catalyst without influence on the selectivity of the diethyl carbonate. Through XPS analysis shown in **Figure 3**, the percentage of chlorine dropped from 12.6 % to 6.5 % of the catalyst CuCl₂/PdCl₂/NaOH/KCl/a.c. after the reaction. The results indicate that chloride ion is an important component in the catalysts, and therefore must be playing a key role in forming DEC. The chlorine ion run away is the main reason of the deactivation of the catalyst. How to fix the chlorine ion becomes the key to prolong the lifetime of the catalysts. Because potassium can apply the chlorine ion, the activity of the catalyst can be increased and maintain more hours.

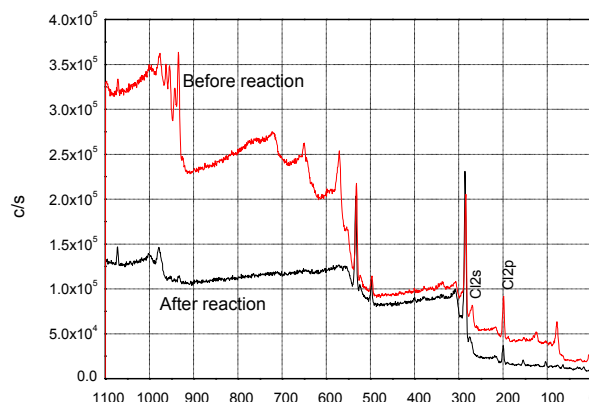


Figure 3. Comparison of the XPS spectrum of CuCl₂/PdCl₂/NaOH/KCl/a.c. catalyst before reaction and after reaction.

Conclusions

Diethyl carbonate can be prepared with high selectivity using a catalyst CuCl₂/PdCl₂/NaOH supported on activate carbon. When potassium salts was added as a promoter, the conversion of ethanol and the formation of diethyl carbonate increased. Through XPS analysis, we can conclude that potassium chloride shows the best activity because chloride ion is an important component in the catalysts, and therefore it must be playing a key role in forming DEC. The production of by-products are independent on the main reaction, it just because the oxidative of ethanol. The four steps mechanism is given to make the thermodynamic calculation and analysis easy.

Reference

- (1) Pacheco, M. A., Marshall, C. L. *Energy & Fuel*, **1997**, 11,2~29.
- (2) Mo, W. L., Li, G. X., Zhu, Y. Q. *Chinese Journal of Catalysis*, **2003**, 24, 3~4.
- (3) Wang, Y. J., Zhao, X. Q., Yuan, B. G. *Applied Catalysis A: General*, **1998**, 171, 255-260.
- (4) Dunn, B. C., Guenneau, C., Hilton, S. A., Pahnke, J., Eyring, E. M. *Energy & Fuels* 2002,16(1): 177-181.
- (5) Roh, N. S., Dunn, B. C., Eyring, E. M. Prepr. Pap. - *Am. Chem. Soc., Div. Fuel Chem.*, **2002**, 47(1), 142-143.
- (6) Jiang, R. X., Wang Y. J., Zhao, X. Q. *Journal of Molecular catalysis A: Chemical*, **2002**, 185, 159~166.

Studies on Conversion of FCC Gasoline to Light Olefins and High Octane Number Gasoline with Low Olefin Content

Xiaohong Li, Chunyi Li, Qimin Yuan, Chaohe Yang, Honghong Shan, and Jianfang Zhang

State Key Laboratory of Heavy Oil Processing, University of Petroleum, Dongying 257061, Shandong, China

Introduction

Light olefins, such as ethylene, propylene, butylene, are major basic chemical materials. With the development of global economy the demand for ethylene and propylene increases greatly, and it is estimated that the increasing rates may be 4.8% and 5.6% per year within coming years, respectively^[1]. Presently 90% ethylene^[1] and 70% propylene^[2] are produced by thermal cracking of hydrocarbons, which operates at about 800 °C, in some cases even higher than 1000 °C. Obviously, the energy consumption is very large. Furthermore, limited by the reaction mechanism, the ratio of propylene/ethylene is hardly regulated. In order to improve the production of light olefins, many studies have been carried out worldwide, where catalytic pyrolysis is a very important field^[3-6].

FCC processes provide about 80% commercial gasoline in China. FCC gasoline contains too much olefin and can not meet the gasoline specifications limiting the olefin content not more than 35% (vol). The current methods of reducing olefin content may lead to a significant loss of octane number, as the octane number of olefins is higher.

In catalytic pyrolysis, olefins are more active than other hydrocarbons, such as alkanes, naphthenes, aromatics. Thus, if the olefins in FCC gasoline can be selectively cracked to light olefins by using specially made catalysts at appropriate conditions, then on one hand light olefins can be produced, and on the other hand the octane number of gasoline may be retained or even enhanced as aromatics content increases. Here we will introduce the abecedarian results in this aspect.

Experimental

In the experiments the HZSM-5/Al₂O₃ catalyst was prepared by the semi-synthesis method. The particle size of the catalyst is 20~100mm. During the reaction H₂O and feed were pumped into the fixed-bed micro-reactor from the upside respectively. In the atmosphere of N₂ and/or stream the feed was cracked over the catalyst bed, which was placed in the middle of the reactor and the free space was filled with quartz sand to shorten the residence time of oil gas. After reaction, N₂ was used to sweep the reactor to ensure all the oil gas to be out. The effluent from the reactor was collected with a condenser immersed in ice/water bath. The uncondensed gas was collected by draining-water method and analyzed with Varian 3800 chromatograph. The hydrocarbon composition of the gasoline and the octane number were analyzed with HP5890 chromatogram.

Results and Discussion

In order to confirm the feasibility of the above idea, the experiments of thermal cracking and catalytic pyrolysis were conducted. In Table 1, the conversion in the catalytic pyrolysis is 12.91 percent points lower than that in the thermal cracking, while the yield of ethylene + propylene in the former is 2.99 percent points higher and the selectivity is 21.32 percent points higher, and the yields of the byproducts including H₂, CH₄, C₂H₆ and coke in the catalytic pyrolysis are much lower than that in the later. This may be caused by selective catalysis of the catalyst and the restraining effect

of lower temperature on the free radical mechanism of thermal cracking. Furthermore, the ratio of propylene/ethylene in the catalytic pyrolysis is 2.12, which is much higher than the value 0.90 in the thermal cracking.

Table 1. Comparison of thermal cracking and catalytic pyrolysis

Process	Thermal Cracking		Catalytic Pyrolysis	
Temperature, °C	750		600	
Conversion, %	57.33		44.42	
Catalyst	Quartz sand		HZSM-5/Al ₂ O ₃	
	Y, %	S, %	Y, %	S, %
Hydrogen	0.30		0.06	
Methane + Ethane	15.22	26.56	1.78	4.10
Ethylene	15.10	26.33	10.17	22.89
Propylene	13.67	23.84	21.59	48.60
Butylene	8.17	14.25	7.73	17.40
Coke	0.24		0.03	
Ethylene + Propylene	28.77	50.17	31.76	71.49

Reaction conditions: mass of catalyst: 7g, reaction time: 1h, H₂O/Oil ratio (wt/wt): 0.55, feed: Daqing gasoline, input rate of feed: 150g/h

Table 2. RON, MON and antiknock index of feed and product after catalytic pyrolysis

	RON	MON	Antiknock Index
Feed	91.0	78.1	84.5
Pruduct	95.7	83.1	89.4

Reaction conditions are the same as that of Table 1.

Table 3. Hydrocarbon composition of feed and product after catalytic pyrolysis (wt%)

	Alkanes	Naphthenes	Aromatics	Olefins
Feed	38.67	8.50	17.54	35.27
Product	41.70	10.67	37.76	10.39

Reaction conditions are the same as that of Table 1.

After the catalytic pyrolysis, the RON, MON and antiknock index of the remaining gasoline (Table 2) rise by 4.7, 5.0 and 4.9, respectively. The increase of octane number has close relation with the hydrocarbon composition listed in table 3. After the catalytic reaction, although the olefin content drops from 35.27% to 10.39%, the aromatics, whose syncretic octane number are about 110, rise more than 20 percent points. The conversion of olefins is more than 85%, and is much more than that of the other hydrocarbons. The reason maybe ascribes to two aspects: one is the reaction rate of olefins is much faster, and the other is that the pore size of the HZSM-5 only allows alkanes and olefins to enter.

The effects of temperature, residence time, H₂O/Oil ratio (wt/wt) and reaction time in catalytic pyrolysis were also investigated. In Fig. 1, we can see the conversion of the reaction and the yield of ethylene + propylene rise with temperature, while the selectivity to ethylene + propylene drops because the thermal cracking plays an increasing role. The yield increase of ethylene is larger than that of propylene with temperature. Thus, the ratio of propylene to ethylene can be adjusted by varying the reaction temperature.

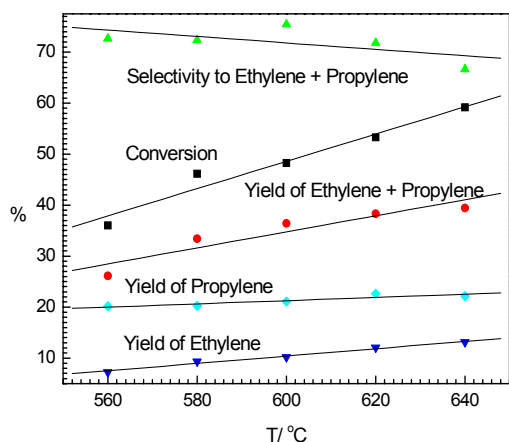


Figure 1. Trends of conversion, yield of products and selectivity to products with temperature (Mass of catalyst: 7g, Reaction time: 1h, Input rate of feed: 150g/h, H_2O/Oil ratio: 0.50).

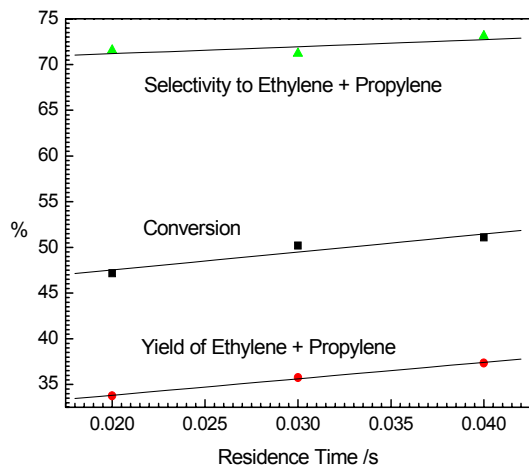


Figure 2. Conversion, yield of products and selectivity to products with residence time (Mass of catalyst: 7g, Temperature: 600°C, Reaction time: 1h, Input rate of feed: 150g/h, H_2O/Oil ratio: 0.34).

As shown in Fig. 2, the conversion of the reaction and the yield of ethylene + propylene increase from 47.17% to 51.09% and from 33.75% to 37.35% with the residence time of oil gas in the reactor varying from 0.02s to 0.04s, respectively. It seems that the longer time is more favorable. However, it is well known that olefins may be saturated due to hydrogen transfer, therefore, the residence time should not be too long.

Steam can reduce the partial pressure of hydrocarbons and restrain coking of the catalyst^[7]. On no steam participation, the conversion, the yield of ethylene + propylene and the selectivity to ethylene + propylene are 20.61%, 37.44%, 55.05%, respectively. However, when the H_2O/Oil ratio is 0.28 (Fig. 3), the yield of ethylene + propylene and the selectivity to it increase by 15.0 and 32.0 percent points, respectively. The reason that the conversion decreases with H_2O/Oil ratio may be due to the reduction of the partial pressure of oil gas. In addition, producing high temperature steam will consume very large amount of energy. So the appropriate H_2O/Oil is crucial for producing light olefins economically. In order to study the effect of the reaction time, some experiments were

carried out. In Fig. 4, the conversion and the yield of ethylene + propylene fall quickly by 14.4 and 9.8 percent points respectively when the reaction time were prolonged from 20min to 120min, which is caused by the coking deactivation. However, the selectivity of the catalyst to ethylene + propylene keeps about 72%, and even after reacting for 120min the yield of ethylene + propylene is still higher than 30%.

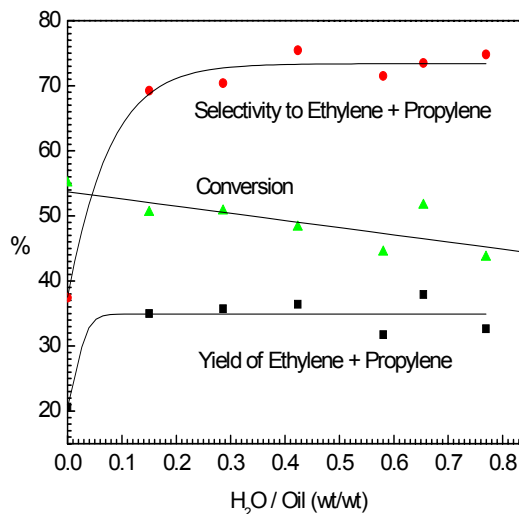


Figure 3. Curves for conversion, yield of products and selectivity to products with H_2O/Oil ratio (Mass of catalyst: 7g, Temperature: 600°C, Reaction time: 1h, Input rate of feed: 150g/h).

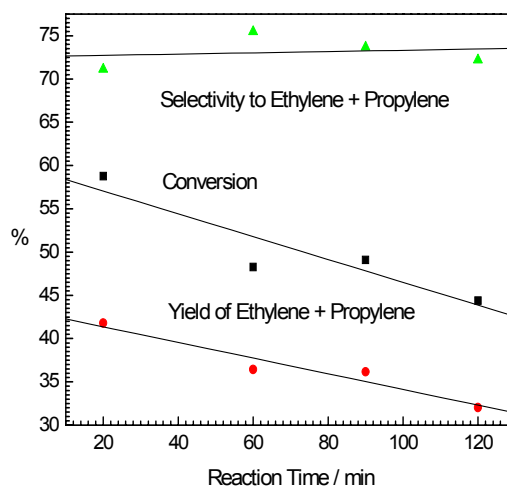


Figure 4. Effect of reaction time on the catalytic pyrolysis of FCC gasoline (Mass of catalyst: 7g, Temperature: 600°C, H_2O/Oil ratio: 0.50, Input rate of feed: 150g/h).

The catalytic pyrolysis of FCC gasoline is a new and effective method to produce light olefins. One of its prominent advantages is that high octane number gasoline with low olefins content can be obtained simultaneously. Certainly, the appropriate reaction conditions and the special catalyst should be studied further.

Acknowledgement

This work was supported by PetroChina, Corp., under contract 020802-05-2.

References

1. Yi, H. L.; Shi, Zh. C.; Li, C. Y.; Wang, X. Q.. *Petroleum Processing and Petrochemicals*, **2002**, 33(3), 38.
2. Zhou, Q.; Hu, J. L.. *Shihua Jishu*, **2001**, 8(4), 244.
3. Zhang, Zh. G.; Xie, Ch. G.; Shi, Zh. Ch.; Wang, Y. M.. *Petroleum Processing and Petrochemicals*, **2001**, 32(5), 21.
4. Xie, Ch. G.; Pan, R. N.. *Petroleum Processing and Petrochemicals*, **1994**, 25(6), 30.
5. Powers, D. H.; Webber, K. M.. W.O. Pat., No. 0,181,280, **2001**.
6. Chester, A. W.; Degnan, T. F.; Kiu, K.; Timken. H. K. C.; Mathias. M. F.; Woolery, G.L.. W.O. Pat., No. 0,031,215, **2000**.
7. Cheng, Y. G.; Mao, W. X.; He, Y. K.. *Petrochemical Technology*, **2001**, 30(4), 311.

CS₂-SOLUBLE FRACTIONS FROM MACERALS AND EXTRACTION KINETICS

Yugui Zhang¹ Yajun Tian² Wang Baojun¹ Xie Kechang¹
Xianyong Wei³

1. State Key Lab of C1 Chemistry and Technology, Taiyuan University of Technology, Taiyuan, 030024, P. R. China
2. College of Chemistry and Chemical Engineering, Nanjing University, Nanjing 210093, P.R. China
3. Department of Applied Chemistry, School of Chemical Engineering, CUMT, Xuzhou, Jiangsu 221008, China

Introduction

The solvent extraction techniques have long become of valid methods to study properties, constituents and structures of coal. Coal extracts have been used to obtain coal material in solution form that can readily be characterized^{1, 2}. In general terms, the mechanism of coal extraction seems to consist in substitution: electron-donating solvent molecules replace the coal electron donor participants in the forces³. Numerous organic solvents used for coal extraction had been characterized by quantitative measures^{3, 4, 5} of their electron-donor (DN) and electron-acceptor (AN) properties (Gutmann's⁶ donor and acceptor numbers) as well as by Hildebrand's solubility parameter and Snyder's polarity index. Correlations were found between the extract yields on one hand and donor numbers of the solvents as well as the differences (DN-AN), on the other. Though extract yield with solvent CS₂ is generally lower, solvent CS₂ is available for use to extraction of many low weight molecular compounds in coal. However, for long time, not much attention had been paid to Studying the law of extract process of coal and investigating the kinetic of the extraction.

In this work, fractions and kinetics of extraction for several macerals with solvent CS₂ were studied, origin and occurrence of the low molecular compound were discussed.

Experimental

Coal Samples. Three groups of coal samples used in this study respectively were taken from Fushun west strip mine (FS) in Liaoning province, Datong Sitai mine (DT) and Pingshou strip mine (PS) in Shanxi province, included a resinite, two inertinite and three vitrinite concentrates. Individual maceral concentrates were drawn from the same coal seam for each couple samples in each mine, and maceral purities were all higher than 95%. Proximate and ultimate analyses data of coal samples used in this study are presented in Table 1.

Table 1 Proximate and ultimate analyses data of coal samples

Coal samples	%A _{ad}	%V _{daf}	%C _{daf}	%H _{daf}	%N _{daf}	%O _{daf} [*]	%S
FS vitrinite	2.46	41.50	79.90	5.82	1.00	13.28	0.51
FS resinite	0.89	99.01	81.40	10.10	0.14	7.71	0.13
DT vitrinite	10.02	31.98	—	—	—	—	0.97
DT fusinite	15.27	27.50	—	—	—	—	—
PS vitrinite	5.54	40.38	79.89	5.32	1.78	13.23	0.58
PS fusinite	8.36	28.24	84.73	3.96	9.89	0.66	0.76

O^{*}: by difference

Solvent extraction. Approximately 10 g of coal with 200 ml carbon disulfide was extracted in the Soxhlet extractor. In order to determinate the weight of extract as a function of time, the solvent contained extract fraction was frequently replaced by fresh solvent, and a series of solvable fractions of the certain time range were obtained. The liquid of each fraction was distilled to 3-5ml concentrated liquids in the vacuum rotatory evaporator and then dried in air at 35°C until partially dry and then dried to constant weight in a vacuum drying oven.

The extraction yield is the weight of extract divided by the weight of organic substance in coal sample.

Results and Discussion

Extract yield. Table 2 is extract yields of PS and DT coal samples in different ranges of time. Table 3 is extract yields and family constitutes of FS coal in different ranges of time.

Table 2 Extract yields of PS and DT coal samples in different ranges of time (on the basis of dry ash free)

Time range	PS fusinite	PS vitrinite	DT fusinite	DT vitrinite
0-1	0.42	0.80	0.62	0.74
1-3	0.11	0.11	0.17	0.36
3-7	0.14	0.16	0.13	0.17
7-15	0.17	0.17	0.18	0.28
15-31	0.27	0.18	0.21	0.35
31-64	0.17	0.14	0.14	0.19
64-103	0.10	0.10	0.10	0.11
0-103	1.39	1.65	1.54	2.20

Table 3 Extract yields of FS coal sample in different ranges of time (on the basis of dry ash free)

Time range	Vitrinite	Time range	Resinite
0-2	0.71	0-2	15.38
2-9	0.33	2-7	2.67
9-22	0.16	7-25	0.97
22-46	0.15	25-49	0.47
46-70	0.10	49-73	0.29
70-94	0.11	0-73	19.78
0-94	1.56		

Table 2 and table 3 show that the variety of extract yields is very small after long time, therefore the sum of yield during all ranges is regarded as the theoretic extraction yield.

Normalization of extract yield. Normalized ratio is defined as the fraction of an extract yield to the theoretic extraction yield. Figure 1 is a plot of normalized ratio vs. time for FS vitrinite and FS resinite, and figure 2 for PS and DT coals.

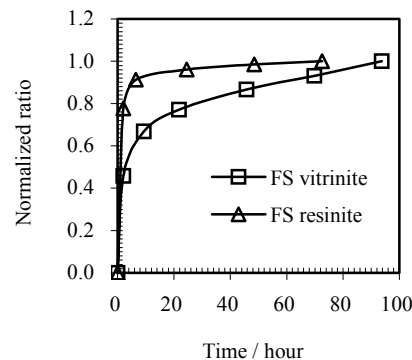


Figure 1. The curve of the normalized ratio of extraction yield vs. time for FS vitrinite and resinite coal

In generally, the extract rate of all macerals is high at beginning few hours, and then decelerates gradually. The extract rate of FS resinite is faster than that of FS vitrinite. Although their biggest yield shows little difference, their rates do notable difference. However, for DT vitrinite and DT inertinite, their extract yields have notable difference, but little difference for their rates.

Extract kinetic. Studying the process of extraction and investigating the kinetic of the extraction is very important for the probable

industrialization. Also, it may be beneficial to understand the mechanism of the extraction.

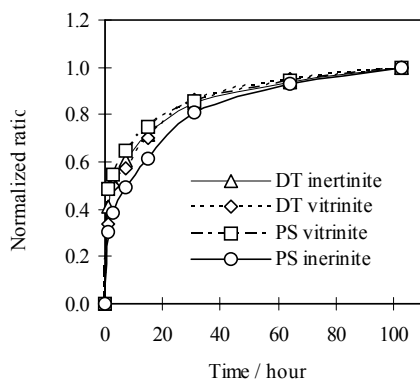


Figure 2. The curve of the normalized ratio of extraction yield vs time for DT and PS coals

Assume the extract rate is first order of the extractable content in coal, that is:

$$\frac{d\alpha}{d\tau} = k(1 - \alpha) \quad (1)$$

where, α , the normalized ratio of extract yield

k , the constant of extract rate

τ , time of extraction

its integral formula is

$$-\ln(1 - \alpha) = k\tau \quad (2)$$

In theory, its plot should be a beeline to pass the origin drop, and the slope of beeline is k , the constant of extract rate.

For instance, with DT vitrinite, the result of $-\ln(1 - \alpha)$ vs. τ displays in **Figure 3**, and the plot is not a beeline to pass the origin, which illuminates that process of extraction is not the process of first order process. However, the whole process can be divided into two first order stages to describe, the critical time of the two stages is about 3.08 hour, the slopes of two stages are 0.25 and 0.038 respectively.

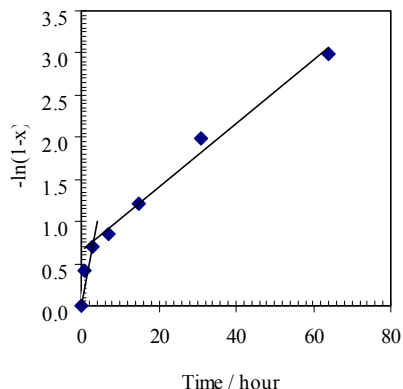


Figure 3. Kinetic curves of extraction of FS vitrinite.

Above all, we can describe the extraction process with two first order sub-processes. A group of general formulae are shown as **Formula (3) and (4)**.

For the first stage,

$$\alpha = 1 - e^{-k_1\tau} \quad (0 \leq \tau < a) \quad (3)$$

For the second stage,

$$\alpha = 1 - e^{-[k_2(\tau-a)+b]} \quad (\tau \leq a) \quad (4)$$

where, k_1 is extract rate constant of the first stage,

k_2 is extract rate constant of the second stage,

a is the critical time between the first stage and second stage,

b is value of formula $-\ln(1 - \alpha)$, when $\tau = a$,

that is $b = k_1 \times a$.

After regression, corresponding parameters is obtained, so the extraction process of FS vitrinite could be simulated by **Formula (5) and (6)**.

For the first stage,

$$\alpha = 1 - e^{-0.25\tau} \quad (0 \leq \tau < 3.08) \quad (5)$$

For the second stage,

$$\alpha = 1 - e^{-[0.038(\tau-3.02)+0.755]} \quad (3.08 \leq \tau) \quad (6)$$

It is found in **Figure 4** that the prediction values match the experimental results very well. The confidence of simulation is 0.9904.

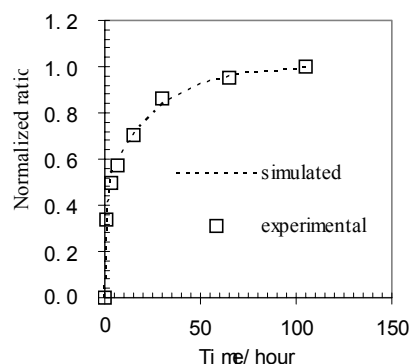


Figure 4. Comparison of simulation with experimental results for DT vitrinite

In a similar way, the parameters of other samples are obtained and presented in **Table 4**. For most cases, their extraction process could be described by two first order producers, except FS resinite.

Table 4 Kinetic parameters of extraction of CS_2 solvent

samples	k_1	k_2	a	b	Confidence
DT vitrinite	0.25	0.038	3.02	0.755	0.9904
DT fusinite	0.27	0.033	3.02	0.817	0.9774
PS vitrinite	0.31	0.033	3.00	0.930	0.9640
PS fusinite	0.18	0.036	2.90	0.522	0.9872
FS vitrinite	0.13	0.025	8.68	1.128	0.9614
FS resinite	0.41	0.043	5.98	2.451	0.7734

Acknowledgment. BASIG NATURES AND PURPOSES in The Key Technologies Research and Development program, under contract G1999022101, supported this work.

References

1. Y.G. Zhang, B.J. Wang, Y.J. Tian et al. Journal of China University of Mining and Technology, 2003(3)
2. Z M Zong, X H Wang, X H Gu, et al. Proceedings of the 7th China-Japan Symposium on Coal and C1 Chemistry, 2001, 347-350.
3. A. Marzec, M. Jozwa, K. Bettlej. Fuel Processing Technology. 1979,2(1), 35-44.
4. M. Nishioka. Fuel, 1993, 72 (12): 1719-1723
5. V. Gutmann, The Donor- Acceptor Approach to Molecular Interactions, Plenum, New York, 1978.
6. A. Marzec. Fuel Processing Technology , 2002,77-78, 25-32.